ROLE OF WAVES ON THE CIRCULATION OF THE ARCTIC MIDDLE ATMOSPHERE: RAYLEIGH LIDAR MEASUREMENTS AND ANALYSIS

By

Brentha Thurairajah

RECOMMENDED: _____

_____

_____

_____

_____
Advisory Committee Chair

_____
Chair, Department of Atmospheric Sciences

APPROVED: _____
Dean, College of Natural Science and Mathematics

_____
Dean of the Graduate School

_____
Date

ROLE OF WAVES ON THE CIRCULATION OF THE ARCTIC MIDDLE ATMOSPHERE: RAYLEIGH LIDAR MEASUREMENTS AND ANALYSIS

A

DISSERTATION

Presented to the Faculty

of the University of Alaska Fairbanks

in Partial Fulfillment of the Requirements

for the Degree of

DOCTOR OF PHILOSOPHY

By

Brentha Thurairajah, B.E., M.S.

Fairbanks, Alaska

December 2009

Abstract

Rayleigh lidar measurements of the upper stratosphere and mesosphere are made on a routine basis over Poker Flat Research Range (PFRR), Chatanika, Alaska, (65°N, 147°W). Rayleigh lidar measurements have yielded high resolution temperature and density profiles in the 40-80 km altitude. These measurements are used to calculate gravity wave activity in the 40-50 km altitude. The thermal structure of the stratosphere and mesosphere is documented using an eight year data set, and the role of small scale gravity waves on the large scale meridional circulation is analyzed in terms of the synoptic structure of the Arctic stratospheric vortex, Aleutian anticyclone, and planetary wave activity. The monthly mean temperature indicates colder January temperatures that appear to be due to the increase in frequency of occurrence of stratospheric warming events from 1997-2004. The gravity wave potential energy density is analyzed during stratospheric warming events in two experimental time periods. From the first study consisting of three winters, 2002-2003, 2003-2004, and 2004-2005, the first direct measurement of suppression of gravity wave activity during the formation of an elevated stratopause following the 2003-2004 stratospheric warming event is presented. The gravity wave potential energy density at Chatanika is positively correlated with horizontal wind speeds in the stratosphere, and indicates that the wave activity in the 40-50 km altitude is partially modulated by the background flow. In the second study with more recent winters of 2007-2008 and 2008-2009, no systematic difference in the magnitude of potential energy density between the vortex displacement warming event during the 2007-2008 winter and vortex split warming event during the 2008-2009 winter is found. However, the low correlation between gravity wave potential energy and horizontal wind speed after the first warming in January 2008, and a higher correlation after the January 2009 warming suggests that while the gravity wave activity after the 2009 warming is modulated by the background flow, other wave sources modulate the gravity wave activity after the 2008 warming.

Table of Contents

Page

Signature page ..... **i**

Title Page ..... **ii**

Abstract ..... **iii**

Table of Contents ..... **iv**

List of Figures ..... **vii**

List of Tables ..... **x**

List of Appendices ..... **xi**

Acknowledgements ..... **xii**

Chapter 1. Introduction **1**

1.1. Middle Atmospheric Study 1

1.2. The Circulation of the Arctic Middle Atmosphere 3

1.3. Rayleigh Lidar 8

1.4. Scope of this study 11

References 14

Chapter 2. Multi-Year Temperature Measurements of the Middle Atmosphere at Chatanika, Alaska (65°N, 147°W)[1] **25**

Abstract. 25

2.1. Introduction 26

2.2. Rayleigh Lidar Technique 28

2.3. Rayleigh Lidar Measurements 31

2.4. Comparison of Measurements from Chatanika with Other Arctic Measurements and Models 34

2.5. Discussion 36

2.6. Conclusions 39

Acknowledgments 40

Page
References 42

Chapter 3. Rayleigh Lidar Observations of Reduced Gravity Wave Activity during the Formation of an Elevated Stratopause in 2004 at Chatanika, Alaska (65°N, 147°W)[2] 59

Abstract. 59
3.1. Introduction 60
3.2. Rayleigh Lidar Technique 62
3.3. Rayleigh Lidar Measurements 65
3.3.1. Temperature Profile 65
3.3.2. Gravity Wave Activity 66
3.4. Arctic Planetary Wave Activity and Synoptic Structure 68
3.4.1. Pan Arctic Perspective 69
3.4.2. Chatanika Perspective 72
3.5. Variability of Gravity Wave Activity and Synoptic Structure 75
3.6. Summary and Conclusion 77
Acknowledgments 79
References 80

Chapter 4. Gravity Wave Activity in the Arctic Stratosphere and Mesosphere during the 2007-2008 and 2008-2009 Stratospheric Sudden Warmings[3] 99

Abstract. 99
4.1. Introduction 100
4.2. Rayleigh Lidar Data and Analysis 103
4.3. Rayleigh Lidar Measurements 104
4.3.1. Temperature Measurements 104
4.3.2. Gravity Wave Activity 105

Page

4.4. Synoptic View and Planetary Wave Activity during the 2007-2008 and 2008-2009 Winters 107
4.4.1. The 2007-2008 Arctic Winter 108
4.4.2. The 2008-2009 Arctic Winter 109
4.5. The 2007-2008 and 2008-2009 Winters at Chatanika 110
4.6. Comparison of Gravity Wave Activity at Chatanika with Kühlungsborn and Kangerlussuaq 112
4.7. Variability in Gravity Wave Activity 113
4.7.1. Variability in Gravity Wave during the 2007-2008 and 2008-2009 Winters 113
4.7.2. Comparison of Gravity Wave Activity during the 2008-2009 Winter with the 2003-2004 Winter 115
4.7.3. Geographic Variability in Gravity Wave Activity 116
4.8. Conclusion 117
Acknowledgments 118
References 119

Chapter 5. Conclusions and Further Work 137
5.1. Middle Atmosphere Temperature Measurements at Chatanika, Alaska 137
5.2. Suppression of Gravity Wave Activity during the Formation of an Elevated Stratopause at Chatanika, Alaska 138
5.3. Gravity Wave Activity during Different Types of Stratospheric Warmings 138
5.4. Further Work 139

List of Figures

Page

Figure 1.1. The atmospheric temperature profile for Fairbanks, Alaska 21
Figure 1.2. The wave driven middle atmospheric circulation 22
Figure 1.3. Schematic of a Rayleigh lidar system 23
Figure 2.1. Vertical temperature profile plotted as a function of altitude.....48
Figure 2.2. Monthly distribution of 116 Rayleigh lidar measurements 49
Figure 2.3. Nightly temperature profiles as a function of altitude.....50
Figure 2.4. Monthly variation of the stratopause altitude and temperature 51
Figure 2.5. Monthly variation of stratospheric and mesospheric temperatures.....52
Figure 2.6. Variation in rms temperature as a function of month.....53
Figure 2.7. False color plot of monthly mean temperature.....54
Figure 2.8. Vertical temperature profile measured by Rayleigh lidar at PFRR.....55
Figure 2.9. Monthly temperature differences 56
Figure 2.10. Monthly variation of the stratopause in the Arctic.....57
Figure 2.11. Monthly variation of thermal structure of stratosphere and mesosphere 58
Figure 3.1. Relative density perturbations measured by Rayleigh lidar 87
Figure 3.2. Nightly mean temperature profiles measured by Rayleigh lidar.....88
Figure 3.3. Atmospheric stability measured by Rayleigh lidar 89
Figure 3.4. Gravity wave activity - rms density fluctuation, rms displacement fluctuation, and potential energy density 90
Figure 3.5. Variation of rms density fluctuation as a function of buoyancy period 91
Figure 3.6. 3-D representation of the Arctic stratospheric vortex and anticyclones.....92
Figure 3.7. Northern hemisphere polar stereographic plots.....93
Figure 3.8. Planetary wave-one geopotential amplitude at 65^{o}N.....94
Figure 3.9. Temporal evolution of the stratospheric vortex and Aleutian anticyclone.....95
Figure 3.10. Daily wind speed from the MetO analyses data..... 96
Figure 3.11. Monthly mean wind profiles calculated from the MetO analyses data 97
Figure 3.12. Scatter plot of potential energy density per unit mass.....98

Page

Figure 4.1. Nightly mean temperature profiles measured by Rayleigh lidar.....124
Figure 4.2. Atmospheric stability measured by Rayleigh lidar at Chatanika 125
Figure 4.3. Potential energy density measured by Rayleigh lidar at Chatanika 126
Figure 4.4. Monthly variation of potential energy density at Chatanika 127
Figure 4.5. Variation of rms density fluctuation as a function of buoyancy period 128
Figure 4.6. 3-D representation of the Arctic stratospheric vortex 129
Figure 4.7. 3-D representation of the Arctic stratospheric vortex 130
Figure 4.8. SABER planetary wave number one and two geopotential amplitude, gradient winds, and divergence of EP flux at 65^{o}N from mid-January to mid-March of 2008.....131
Figure 4.9. SABER planetary wave number one and two geopotential amplitude, gradient winds, and divergence of EP flux at 65^{o}N from mid-January to mid-March of 2009.....132
Figure 4.10.Temporal evolution of the stratospheric vortex and Aleutian high anticyclone over Chatanika 133
Figure 4.11. Northern hemisphere polar stereographic plots of vortex and anticyclone.134
Figure 4.12. Daily horizontal wind speed from MetO analyses data.....135
Figure 4.13. Scatter plot of potential energy density averaged over the 40-50 km altitude range and MetO wind speed 136
Figure B.1. Range bins and center of range bin in meters.....155
Figure B.2. Normalized density profile from 0.0 to 300.0 km 156
Figure B.3. Generated photon count profile from 0.0 to 300.0 km 157
Figure B.4. Isothermal temperature profile from 40.0 to 80.0 km.....158
Figure B.5. Isothermal temperature profiles from 40.0 to 80.0 km.....159
Figure C.1. Scatter plot of signal to noise ratio (SNR) and ratio of gravity wave variance 163
Figure D.1. False color plot of volume backscatter coefficient and backscatter ratio of aerosol layer as a function of time and altitude on the night of 21-22 January 1999 170
Figure D.2. Integrated backscatter coefficient, variation of altitude and backscatter coefficient of aerosol layer as a function of time on the night of 21-22 January 1999 ...171

Page

Figure D.3. False color plot of volume backscatter coefficient and backscatter ratio of aerosol layer as a function of time and altitude on the night of 11-12 February 1999 172
Figure D.4. Integrated backscatter coefficient, variation of altitude and backscatter coefficient of aerosol layer as a function of time on the night of 11-12 February 1999 .173
Figure D.5. False color plot of volume backscatter coefficient and backscatter ratio of aerosol layer as a function of time and altitude on the night of 24-25 February 2000 174
Figure D.6. Integrated backscatter coefficient, variation of altitude and backscatter coefficient of aerosol layer as a function of time on the night of 24-25 February 2000 .175
Figure D.7. Rayleigh lidar nightly mean temperature profiles 176
Figure E.1. Latitude height plot of zonal mean gradient wind 181
Figure E.2. Latitude height plot of divergence of Eliassen-Palm flux.....182

List of Tables

Page

Table 1.1. Specifications of NICT Rayleigh lidar system at Chatanika, Alaska 19
Table 3.1. Buoyancy period and gravity wave activity at 40-50 km at Chatanika 85
Table 3.2. Buoyancy period and gravity wave activity at 40-50 km at Chatanika 86
Table 4.1. Buoyancy period and potential energy density at Chatanika.....123
Table A.1. Variation of Earth's radius (*RE*) in km and root mean square error 148
Table A.2. Acceleration due to gravity, variation of Earth's radius (*RE*) in km and root mean square error.....149
Table D.1. Rayleigh lidar observation times and rocket launch times 168
Table D.2. Characteristics of aerosol layer from rocket exhaust.....169

List of Appendices

Page

Appendix A. Calculation of Constant of Acceleration due to Gravity and Radius of the Earth at 65^{o}N 141

A.1. Method 1 143

A.1.1. Linear Approximation 143

A.1.2. Quadratic Approximation 143

A.2. Method 2 144

A.3. Result 146

References 147

Appendix B. Effect of Binning Photon Counts on Rayleigh Lidar Temperature Retrieval 150

B.1. Density Calculation 151

B.2. Photon Count Calculation 151

B.3. Temperature Calculation 152

References 154

Appendix C. Effect of Exponential Smoothing on Gravity Wave Variances 160

References 162

Appendix D. Effect of Aerosols on Rayleigh Lidar Temperature Retrieval 164

References 167

Appendix E. Gradient Wind and Eliassen-Palm Flux Analysis using SABER\TIMED data 177

E.1. Gradient Wind Calculation 178

E.2. Eliassen-Palm Flux Calculation 178

References 180

Acknowledgments

I would like to thank my advisor Dr. Richard Collins for the opportunity to work with lidars, for the patient discussions, and constant encouragement. I thank my committee members Drs. Kenneth Sassen, Ruth Lieberman, Uma Bhatt, and David Atkinson for their constructive criticism and encouragement during my doctoral study. The lidar data presented in this dissertation is the result of the dedicated work by the former students of the Lidar Research Laboratory, and current students Agatha Light and Brita Irving with never ending support from Dr. Collins – Thank You. I would also like to thank Agatha Light for contributing to the data presented in Appendix A. I thank the staff of Poker Flat Research Range for their assistance. I will always be grateful to the faculty, staff, and students of the Department of Atmospheric Sciences and Geophysical Institute. I thank my family and friends for their unconditional support.

I thank the following colleagues without whom the journal papers that form Chapter 2, 3, and 4 of this dissertation would not have been possible. I thank my advisor Dr. Collins for informative discussions, suggestions and comments. The Rayleigh lidar was installed at Poker Flat Research Range, Chatanika, Alaska by Dr. Mizutani and the National Institute of Information and Communications Technology, Japan as part of the Alaska Project. I thank Dr. Harvey for contributions to the analyses of the MetO data, Dr. Lieberman for providing the opportunity to visit Colorado Research Associates in Boulder, Colorado and learn satellite data processing methods and for contributions to the satellite data analysis, Drs. Gerding and Livingston for providing the Rayleigh lidar data for Kangerlussuaq and Kühlungsborn, respectively.

Chapter 1. Introduction

1.1. Middle Atmospheric Study

The middle atmosphere refers to the region from the tropopause (~10-16 km) to the homopause (~110 km) where the constituents are well mixed by atmospheric eddy processes. Interest in the middle atmosphere increased with the discovery of the ozone hole in the 1980's. Trends in stratospheric temperatures have been recognized as an important component in assessing changes in the stratospheric ozone layer [*Ramaswamy et al.,* 2001]. More recently observational and modeling studies indicate that due to the coupling that exists between the various atmospheric regions the study of the upper atmosphere can have important implications on our understanding of the lower atmosphere. For example, results from model simulations from the 1960s to 1990s have shown that a strengthening of the stratospheric winter jet caused a strengthening of the tropospheric westerlies in the mid to high latitudes, a weakening of the westerlies at low latitudes, and an increase in the North Atlantic Oscillation (NAO) index [*Scaife et al*., 2005]. Model simulations also indicate a strengthening of the Brewer Dobson circulation, a large scale stratospheric mean meridional circulation in which air rises in the tropics and moves poleward and downward in the winter hemisphere [*Brewer*, 1949; *Dobson*, 1956] under a changing climate [*Butchart et al.*, 2006; *Deckert and Dameris*, 2008]. For example *Garcia and Randel* [2008] used Whole Atmosphere Community Climate Model (WACCM) simulations to show an acceleration of the Brewer-Dobson circulation with increase in greenhouse gases in the troposphere. They attribute this strengthening circulation to the increased wave driving in the subtropical lower stratosphere caused by changes in zonal mean zonal winds brought about by change in greenhouse gases in the troposphere (an increase in greenhouse gases would increase the meridional temperature gradient in the subtropical upper troposphere and lower stratosphere - the region of largest temperature contrast) that allow enhanced propagation and dissipation of planetary waves in the stratosphere.

Since the wave-driven general circulation in the middle atmosphere is expected to be altered by climate change in the troposphere, it is important to first understand the changes occurring in the asymmetric Arctic middle atmospheric circulation. Model studies [e.g., *Hauchecorne et al.*, 2007; *Siskind et al.*, 2007] have emphasized the coupled role of planetary and gravity waves in the variability of the Arctic wintertime stratosphere and mesosphere. But small scale gravity waves are not measured but parameterized in middle atmospheric models. Rayleigh lidar (Light Detection and Ranging) is one of the few instruments that can provide direct high resolution measurements of gravity waves in the stratosphere and mesosphere. A review of key Rayleigh lidar observations that highlight the capability of this lidar in measuring temperature, gravity waves, and tides in the middle atmosphere can be found at *Grant et al*. [1997]. A comprehensive analysis of gravity wave activity in the mid-latitude middle atmosphere by Rayleigh lidar measurements can also be found at *Wilson et al*. [1991a; 1991b].

The middle atmosphere in addition to being of interest in general can thus play a major role in understanding the atmosphere as a whole [*Houghton*, 1986]. The knowledge of the role of small scale and large scale processes on the middle atmosphere can be used in fully coupled models like Whole Atmosphere Community Climate Model (WACCM) [e.g., *Garcia and Randel*, 2008]. A basic understanding of the non-linear fluid dynamics of the middle atmosphere can provide information for forecasting changes in ozone concentration and temperature trends. In addition, including the stratosphere in models is expected to improve the skill in weather forecasting. This dissertation is focused on using Rayleigh lidar measurements of temperature and density of the upper stratosphere and mesosphere over Chatanika, Alaska (65^{o}N, 147^{o}W) to analyze the thermal structure and gravity wave fluctuations in the middle atmosphere. We use the Rayleigh lidar measurements in combination with Sounding of the Atmosphere using Broadband Emission Radiometry (SABER) instrument aboard the Thermosphere Ionosphere Mesosphere Energetics Dynamics (TIMED) [*Mertens et al*., 2004; *Russell et al*., 1999] satellite data and United Kingdom Meteorological Office (MetO) global analyses data to quantify the effect of the stratospheric vortex and anticyclone, and mean flow on

atmospheric gravity waves and the implications on the middle atmospheric circulation. Gravity waves are analyzed during two experimental time periods, each period with marked different meteorological conditions.

1.2. The Circulation of the Arctic Middle Atmosphere

The atmosphere is divided into the troposphere, stratosphere, mesosphere, and thermosphere (Figure 1.1) based on the vertical temperature structure. The middle atmosphere includes the stratosphere, mesosphere, and lower thermosphere (~10-110 km). The temperature increase with height in the stratosphere, from the tropopause to the stratopause is due to the absorption of ultraviolet solar radiation (~240-290 nm) by the ozone layer. The temperature decreases with height in the mesosphere. In the thermosphere the temperature increases with height due to the absorption of extreme solar ultra violet radiation (<100 nm). In the absence of dynamical processes, the middle atmosphere would be at radiative equilibrium with uniform temperature increase from the winter pole to the summer pole. The observed temperatures, however, show a temperature increase from the cold tropical tropopause to the mid and high latitude tropopause in the winter hemisphere. The summertime upper mesosphere (~65-90 km) is also significantly colder then the wintertime upper mesosphere (Figure 1.1). This deviation from radiative equilibrium reflects that dynamical processes play a major role in maintaining circulation of the middle atmosphere.

The mean zonal wind in the lower stratosphere follows the tropospheric zonal circulation with westerly winds in both hemispheres and the jets centered at 30^o – 40^o latitude. Above 20 km and in the mesosphere the mean zonal winds are westerly in the winter hemisphere and easterly in the summer hemisphere. In the extratropics above ~85-95 km the zonal flow reverses direction. The seasonal variation in solar heating influences the zonal mean flow. Owing to the meridional thermal gradient the strong westerly winds in the polar winter stratosphere form the polar vortex, a synoptic scale cyclone that isolates cold air from mid-latitudes and supports the formation of Polar Stratospheric Clouds (PSCs) that enhance ozone depletion [e.g., *Solomon,* 1999; *Shibata*

et al., 2003]. Another feature of the stratospheric circulation are the large quasi-stationary anticyclones, the most common being the Aleutian anticyclone in the northern hemisphere and the Australian anticyclone in the southern hemisphere [*Harvey et al*., 2002]. The Aleutian anticyclones are so called because at ~10 hPa maximum geopotential amplitudes are found over the Aleutian Islands [*Harvey and Hitchman*, 1996]. The Arctic stratospheric vortex is usually found in the eastern Arctic.

Local variations in wind speed and direction are linked to the presence of atmospheric waves. Atmospheric waves can be defined as 'propagating disturbances of material contours whose acceleration is balanced by a restoring force' [*Brasseur and Solomon*, 2005]. Atmospheric waves exert a zonal force on the background flow through transfer of momentum by wave transience (change in amplitude with time), wave breaking, or dissipation. This zonal force exerted on the mean flow influences the global circulation of the middle atmosphere. Waves that are important for the middle atmospheric circulation include planetary scale Rossby waves and small scale gravity waves.

Gravity waves are small scale waves with horizontal wavelengths from tens to hundreds of kilometers. Their restoring force is buoyancy. One of the main sources of vertically propagating gravity waves in the middle atmosphere is topography, and such waves are also known as mountain waves. It has been shown that in high latitudes gravity waves with vertical wavelengths between 2 and 15 km can be measured reliably with a Rayleigh lidar [e.g., *Duck et al*., 2001]. For such vertically propagating waves the intrinsic frequency ($\hat{\omega}$) lies between the buoyancy frequency (N) and the Coriolis parameter (f),

$$N > \hat{\omega} > f \tag{1.1}$$

The intrinsic frequency, $\hat{\omega} = N.K_h/m$ is the frequency that would be observed in a frame of reference moving with the background wind ($\bar{u}, \bar{v}$) [*Fritts and Alexander*, 2003]. For an upward propagating gravity wave with observed frequency ω (ω = $k.c_h$), the dispersion relation reduces to,

$$\hat{\omega} = \omega - k.\bar{u}_h \tag{1.2}$$

where k is the horizontal wave number, $\bar{u}_h$ is the horizontal wind in the direction of propagation, and c_h is the gravity wave's horizontal phase speed. The dispersion relation relates the frequency of the wave to its wavenumber and atmospheric properties, N and $(\bar{u}, \bar{v})$. Substituting for the intrinsic and observed frequency,

$$\frac{N.k_h}{m} = k_h(c_h - \bar{u}_h) \tag{1.3}$$

where m, the vertical wavenumber is given by $m=2.\pi/\lambda_z$. The vertical wavelength of the upward propagating gravity wave is given by,

$$\lambda_z = \frac{2.\pi}{N}(c_h - \bar{u}_h). \tag{1.4}$$

Thus when the gravity wave phase speed (c_h) is equal to the background horizontal wind speed ($\bar{u}_h$) the wave is absorbed or 'critically' filtered. For orographic or 'stationary' waves the phase speed relative to the ground is zero, and the vertical wavelength reduces to,

$$\lambda_z \approx \frac{2.\pi}{N}\bar{u}_h. \tag{1.5}$$

Thus these waves are 'critically' filtered when the background horizontal wind reduces to zero. Due to strong filtering of gravity waves in the stratosphere, when these waves reach the mesosphere they are westward propagating in summer and eastward propagating in winter. When the horizontal wavelength of the gravity wave becomes greater than ~300 km, the Coriolis force in addition to buoyancy acts as a restoring force. These waves are called inertia-gravity waves.

Planetary (Rossby) waves as their name implies are large scale (~10^4 km) [*Holton*, 2004] waves and their restoring force is the meridional gradient of potential vorticity (or the variation of Coriolis parameter with latitude). Planetary wave sources include large-scale orography and land-sea contrasts. These waves are westward propagating relative to the mean flow [*Brausseur and Solomon*, 2005]. Planetary waves propagate vertically only when the mean winds are westerly, with velocity less than a critical value. Since this condition exists only during winter, planetary waves are absent

in the stratosphere during summer. Wave breaking occurs when the phase velocity of the wave is equal to the background horizontal wind ($c_h = \bar{u}_h$).

The zonal force exerted by planetary waves on the stratosphere can induce an equator to pole Brewer Dobson circulation (Figure 1.2 right panel), while the zonal-force exerted by gravity waves in the mesosphere can induce a pole to pole circulation [*Houghton*, 1978] (Figure 1.2 left panel). While the planetary wave induced circulation is responsible for the transport of critical species (e.g. ozone, water vapor) in the middle atmosphere, the gravity wave circulation is responsible for the cooling of the polar summer mesopause region, and the warming of the polar winter stratopause region (see reviews by *Holton et al.*, 1995; *Holton and Alexander*, 2000; *Fritts and Alexander*, 2003 and references therein].

The zonal asymmetry of the Arctic wintertime circulation due to non-linear wave-wave, wave-mean flow interaction makes it difficult to characterize the Arctic middle atmosphere. An example of wave-mean flow interaction is the occurrence of stratospheric sudden warmings (SSWs). SSWs occur owing to the interaction between upward propagating planetary waves and the zonal polar stratospheric flow. SSWs are characterized by a displaced stratospheric polar vortex, the weakening of the zonal-mean zonal flow, and an asymmetric stratospheric circulation. The commonly accepted mechanism that induces SSWs was first proposed by *Matsuno* [1971] and is as follows; planetary waves form in the troposphere and interact with the tropospheric and stratospheric circulation as they grow and propagate upwards. The westerly jet of the winter middle atmosphere acts as a waveguide for the vertical propagation of planetary waves. The planetary waves grow in amplitude as density decreases, become unstable, and can break to peel off vortex edge materials to produce the surf zone or a vorticity gradient [*Andrews et al*., 1987; *Holton*, 2004]. The wave mean flow interaction is accompanied by wave transience and wave dissipation. While the tropospheric disturbance sometimes becomes a blocking event, this stratospheric disturbance can become a SSW. The stratospheric polar vortex should be pre-conditioned (usually

elongated and pole centered) for an SSW to occur. The planetary wave disturbances that initiate a major SSW are usually the wave-one or wave-two components.

A stratospheric warming is defined as a major warming if at 10 mb or below the zonal-mean temperature increases poleward of 60^{o}N and the zonal mean zonal wind reverses (westerlies to easterlies) [*Labitzke*, 1972]. A SSW is a minor warming if an increase in temperature occurs but there is no wind reversal. SSWs are observed to occur more frequently in the northern hemisphere than the southern hemisphere. It is thought that the less frequent occurrence of a major SSW in the southern hemisphere is because the southern hemispheric vortex is stronger than the northern hemispheric vortex. Therefore, the planetary wave forcing required for wind reversal should be much greater than that required in the northern hemisphere. Up to the mid-1980's, major stratospheric warming events had been reported on average, every other year in the Arctic, while none had been reported in the Antarctic [*Andrews et al*., 1987]. No major warmings were reported from 1990 to 1998 while seven major warmings have been reported from 1999 to 2004 [*Manney et al*., 2005]. The Antarctic major stratospheric sudden warming observed in 2002 was the first reported [*Allen et al*., 2003].

In a recent study, *Liu et al*. [2009] used zonal mean zonal momentum equations and wind measurements from lidar and satellite data to estimate the gravity wave forcing in the mesopause region (~85-100 km). The contribution of winds due to planetary waves was assumed to be negligible. But the authors report that their equation is expected to have large errors during stratospheric warming events since the temporal winds would be significantly different from zonal winds. Thus, in an asymmetric Arctic middle atmospheric circulation, direct measurements of gravity waves under various types and characteristics of stratospheric warming events from single site locations would provide the temporal measurements required to understand the asymmetric circulation. The recent increase in the occurrences of stratospheric warming events with different characteristics and strengths provide such an opportunity to directly measure gravity wave activity in the 40-50 km altitude using a Rayleigh lidar system.

1.3. Rayleigh Lidar

Studies of the Arctic middle atmosphere are challenging not only due to the zonal asymmetry of the wintertime circulation but also due to the limited number of ground-based observations and seasonal limitations of satellite measurements. Radars can measure only up to 30 km, or above 60 km (owing to the lack of scattering media in the middle atmosphere), and meteorological balloons can reach up to ~30 km. Middle atmospheric observations have been made by short-term rocket campaigns and falling sphere experiments. Rayleigh lidars have emerged as a robust technique for sounding the stratosphere and mesosphere and provides high resolution (15 min, 100 m) vertical temperature profiles of the 30-90 km altitude range [*Hauchecorne and Chanin*, 1980]. Rayleigh lidar studies have supported a variety of investigations of the thermal structure of the middle atmosphere providing data for studies of long term and seasonal variations as well as tides and gravity waves. For example analysis of 20 year observations from Observatoire de Haute Provence (OHP) in France (44^{o}N, 6^{o}E) has yielded a cooling of 0.4 K/year in the mesosphere and 0.1 K/year in the stratosphere [*Keckhut et al*., 1995]

Rayleigh lidar systems are so named as they detect Rayleigh scattered light [*Strutt*, 1899] from air molecules. Rayleigh scattering can be defined as the scattering of electromagnetic radiation by particles smaller than the wavelength of the radiation. In an atmosphere free of clouds and aerosols the backscattered lidar signal is proportional to the density of the atmosphere. The expected photon count signal from an altitude range (z - $\Delta z/2$, z + $\Delta z/2$) in a time interval Δt is given by the lidar equation:

$$N(z) = N_s(z) + N_B + N_D \tag{1.6}$$

Where $N_s(z)$ is the lidar photon count proportional to the atmospheric density, N_B is the background skylight count, and N_D is the detector dark current given by,

$$N_s(z) = \eta T^2 \frac{E_L R_L \Delta t}{hc/\lambda_L} \rho(z) \Delta z \sigma_\pi^R \frac{A_T}{z^2} \tag{1.7}$$

$$N_B = \eta \left[H_N R_L \Delta t \pi (\Delta\Theta_R / 2)^2 A_T \Delta\lambda \right] \left(\frac{2\Delta z/c}{hc/\lambda} \right) \tag{1.8}$$

$$N_D = (C_N R_L \Delta t)\left(2\Delta z / c\right) \tag{1.9}$$

where, η is the receiver efficiency, T is the one-way atmospheric transmission at the laser wavelength λ_L (m), E_L is the laser energy per pulse (J), R_L is the repetition rate of the laser (s^{-1}), $\rho(z)$ is the molecular number density at altitude z (m^{-3}), σ_π^R (m^2) is the effective backscatter cross section at λ_L (m), h is the Planck's constant (6.63×10^{-34} J.s), c is the speed of light (3.00×10^8 m/s), A_T is the area of the telescope (m^2), H_N is the background sky radiance ($W/(m^3.\mu m.sr.)$), $\Delta\Theta_R$ is the FOV of receiver (rad), $\Delta\lambda$ is the bandwidth of the detector (μm) and C_N is the dark count rate for the detector (s^{-1}). More information on lasers can be found for example in *Hecht* [1992] and *Silfvast* [1996], and about laser remote sensing and applications of lidar to atmospheric science for example in *Measures* [1984], *Fujii and Fukuchi* [2005], and *Weitkamp* [2005].

The first Rayleigh lidar type measurement of stratospheric density was carried out with the help of a searchlight beam [*Elterman*, 1951]. After searchlights, high altitude atmospheric properties were obtained using light scattered from zenith pointing laser beams [*Kent*, 1967]. 'Laser' is an abbreviation for Light Amplification by Stimulated Emission of Radiation, an expression that covers the important processes in a laser [*Hecht,* 1992]. The advantage of using lasers is that the laser produces monochromatic, coherent light (light waves are in phase with each other). The backscattered light from a laser beam is measured in a manner similar to that of a radar signal. The narrow laser beam with small angular divergence makes it possible to filter out the background light from the night sky. Hauchecorne and coworkers [*Hauchecorne and Chanin*, 1980] systematically improved the accuracy of lidars. Currently Rayleigh lidars are widely used to study the middle atmosphere in the height range of ~30 to 90 km.

The National Institute of Information and Communications Technology (NICT) Rayleigh lidar was installed at Poker Flat Research Range (PFRR), Chatanika, Alaska in November 1997 as part of the Alaska Project [*Murayama et al*., 2007; *Mizutani et al*., 2000], and is jointly operated by NICT and the Geophysical Institute (GI) of the University of Alaska Fairbanks (UAF). The Rayleigh lidar is a nighttime only lidar, and no daytime measurements are taken as this requires a precise design of a very narrow

band pass filter around 532 nm to avoid measuring sunlight. While measurements are taken from August to May under clear sky conditions, no measurements are taken during June and July as Chatanika does not experience astronomical darkness during this period. In Table 1.1 we present the specifications of this lidar, and in Figure 1.3 we present a schematic of a typical lidar system. A detailed description of the density and temperature retrieval, error calculations, and a schematic of the NICT Rayleigh lidar can be found at *Wang* [2003] and *Nadakuditi* [2005]. The algorithm used to calculate temperature from backscattered photon counts can also be found in this dissertation in Appendix B.

Previous Rayleigh lidar studies have focused on single-site measurements of mesospheric inversion layers [*Cutler et al.*, 2001], noctilucent clouds [*Collins et al.*, 2003; *Collins et al*., 2009, *Taylor et al*., 2009], and instrumental performance of the Rayleigh lidar [*Cutler*, 2000; *Wang*, 2003; *Nadakuditi*, 2005]. Rayleigh lidar measurements have also been used to validate the Atmospheric Chemistry Experiment Fourier Transform Spectrometer (ACE-FTS) instrument on the SCISAT satellite [*Sica et al*., 2008]. This dissertation focuses on the dynamics of the stratosphere and mesosphere, primarily the modulation of gravity waves (measured by the lidar) by planetary waves, the synoptic structure of the Arctic stratospheric vortex and anticyclone and the background mean flow. While other lidar studies [*Duck et al*., 2000; *Gerrard et al*., 2002] have examined the variability in temperature structure and gravity wave activity under the influence of the vortex in the eastern Arctic, the location of the NICT lidar at Chatanika provides an excellent opportunity to study this variability under the effect of both the stratospheric vortex and Aleutian anticyclone. The lidar measurements in the eastern Arctic were made during 1992-1998 [*Duck et al*., 2000] and during 1995-1998 [*Gerrard et al*., 2002] at a time when no stratospheric sudden warmings were reported. In contrast, the lidar measurements at Chatanika included in this dissertation were made during two time periods 1997-2005 and 2007-2009, both of which were characterized by the occurrences of SSWs of varying strengths. The lidar measurements during the 2007-2008 and 2008-2009 winters were made as part of the International Polar Year (IPY) project [*Collins*, 2004; *ICSU*, 2004; *NRC*, 2004] and are supplemented by measurements

from Kangerlussuaq, Greenland (67°N, 51°W), a high latitude site, and Kühlungsborn, Germany (54°N, 12°E), a mid-latitude site.

1.4. Scope of this study

The objective of this study is to document the thermal structure of the Arctic stratosphere and mesosphere and to quantify the impact of the stratospheric vortex and anticyclone, and background flow on the vertical propagation of gravity waves using Rayleigh lidar measurements at Chatanika, Alaska. The main elements of this study are to first analyze multi-year Rayleigh lidar measurements of the stratospheric and mesospheric temperature profile from a single site at Chatanika. These temperature measurements also provide information about the background stability of the atmosphere. We then investigate the role of gravity waves in inducing the observed temperature structure using two experimental data sets, one from 2002-2005 winters and the other from more recent 2007-2008 and 2008-2009 winters. The gravity waves are analyzed in terms of the synoptic structure of the stratospheric vortex and anticyclone, and planetary wave activity.

This dissertation consists of five chapters. Chapter 2 is in print as a journal article for *Earth Planets Space* with coauthors R. Collins and K. Mizutani [*Thurairajah et al*., 2009a]. Chapter 3 has been submitted to the *Journal of Geophysical Research* with coauthors R. Collins, L. Harvey, R. Lieberman, and K. Mizutani [*Thurairajah et al*., 2009b]. Chapter 4 is in preparation as an article for submission to the *Journal of Geophysical Research* with coauthors R. Collins, L. Harvey, R. Lieberman, M. Gerding, and J. Livingston [*Thurairajah et al*., 2009c].

In Chapter 2, we present a detailed study of the thermal structure of the upper stratosphere and lower mesosphere above Chatanika, Alaska based on an eight year Rayleigh lidar data set. We compare this temperature structure with climatologies and seasonal data sets from ground-based measurements at other Arctic sites. We document the annual and inter-annual variability of the observed temperature structure and discuss

it in terms of zonal asymmetry, movement of the polar vortex, inter-annual variability of the Arctic middle atmosphere, and stratospheric warming events.

In Chapter 3, we analyze gravity wave activity over three winter periods (2002-2003, 2003-2004, and 2004-2005) with different meteorological conditions that resulted in variable temperature structures. We present the first direct measurement of a suppressed gravity wave activity during the 2003-2004 winter when an extreme major stratospheric warming event lead to the formation of an elevated stratopause and a two month long disruption of the lower and middle stratosphere. We discuss the gravity wave activity in terms of the planetary wave activity and synoptic scale structure of the polar vortex and Aleutian anticyclone.

In Chapter 4, we study the gravity wave activity during different types of stratospheric sudden warmings that occurred in the recent 2007-2008 and 2008-2009 winters. We analyze the variability in gravity wave activity in terms of the synoptic structure of the stratospheric vortex and Aleutian anticyclone, and planetary wave activity. We extend the analysis to understand the geographical variability in gravity wave activity using data from three different sites. We also compare the gravity wave activity during meteorologically similar winters of 2003-2004 (from Chapter 3) and 2008-2009.

In Chapter 5, we review the main results of this dissertation and discuss possible future work.

This dissertation also includes five appendices that are technical notes of the various data processing methods. In Appendix A, I present the calculation of the constants, acceleration due to gravity and radius of Earth at 65^{o}N, used in the Rayleigh lidar processing algorithm. In Appendix B, I present changes to the Rayleigh lidar processing algorithm that were made to obtain more accurate temperature retrieval. In Appendix C, I discuss the effect of the data processing method on the estimation of gravity wave variance. In Appendix D, we investigate the effect of aerosol contamination in the raw photon count data and the consequent effect on the lidar temperature retrieval.

In Appendix E, I discuss the formula and algorithm used to calculate gradient winds and Elaissen-Palm flux from the SABER\TIMED satellite data.

References

Allen, D. R., R. M. Bevilacqua, G. E. Nedoluha, C. E. Randall, and G. L. Manney (2003), Unusual stratospheric transport and mixing during the 2002 Antarctic winter, *Geophys. Res. Lett.*, *30*(12), 1599, doi:10.1029/2003GL017117.

Andrews, D. G., J. R. Holton, and C. B. Leovy (1987), *Middle atmosphere dynamics*, 489 pp., Academic Press Inc., New York.

Brasseur, G. P., and S. Solomon (2005), *Aeronomy of the middle atmosphere*, 644 pp., Springer, Netherlands.

Brewer, A. W. (1949), Evidence for a world circulation provided by the measurements of helium and water vapour distribution in the stratosphere, *Quart. J. Roy. Meteor. Soc*., *75*, 351-363.

Butchart, N., A. A. Sciafe, M. Bourqui, J. de Grandpré, S. H. E. Hare, J. Kettleborough, U. Langematz, E. Manzini, F. Sassi, K. Shibata, D. Shindell, M. Sigmond (2006), Simulations of anthropogenic change in the strength of the Brewer-Dobson circulation, *Clim. Dyn.*, *27*, 727-741, doi:10.1007/s00382-006-0612-4.

Collins, R. L. (2004), *Pan-Arctic Study of the Stratospheric and Mesospheric circulation (PASSMeC),* Expressions of Intent for International Polar Year 2007-2008 activities, ID no.11.

Collins R. L., M. C. Kelley, M. J. Nicolls, C. Ramos, T. Hou, T. E. Stern, K. Mizutani and T. Itabe (2003), Simultaneous lidar observations of a noctilucent cloud and an internal wave in the polar mesosphere, *J. Geophys. Res., 108*(D8), 8435, doi:10.1029/2002JD002427.

Collins, R. L., M. J. Taylor, K. Nielsen, K. Mizutani, Y. Murayama, K. Sakanoi, M. T. DeLand (2009), Noctilucent cloud in the western Arctic in 2005: Simultaneous lidar and camera observations and analysis, *J. Atmos. Sol. Terr. Phys*., *71*, 446-452, doi:10.1016/j.jastp.2008.09.044.

Cutler, L. J. (2000), *Rayleigh lidar studies of the Arctic middle atmosphere*, M.S. Thesis, University of Alaska, Fairbanks.

Cutler L. J., R. L. Collins, K. Mizutani, and T. Itabe (2001), Rayleigh lidar observations of mesospheric inversion layers at Poker Flat, Alaska (65 °N, 147° W), *Geophys. Res. Lett.*, *28*(8), 1467-1470.

Deckert, R., and M. Dameris (2008), From ocean to stratosphere, *Science*, *322*, 53-55.

Dobson, G. M. B. (1956), Origin and distribution of the polyatomic molecules in the atmosphere, *Proc. Roy. Soc. London*, *A236*, 187-193.

Duck, T. J., J. A. Whiteway, A. I. Carswell (2000), A detailed record of High Arctic middle atmospheric temperature, *J. Geophys. Res.*, *105* (D18), 22909-22918.

Duck, T. J., J. A. Whiteway, and A. I. Carswell (2001), The gravity wave-Arctic stratospheric vortex interaction, *J. Atm. Sci.*, *58*, 3581-3596.

Elterman, L. (1951), The measurement of stratospheric density distribution with the searchlight technique, *J. Geophys. Res.*, *56* (4), 509-520, 1951.

Fritts, D. C., and M. J. Alexander (2003), Gravity wave dynamics and effects in the middle atmosphere, *Rev. Geophys*., *41* (1), 1003, doi:10.1029/2001RG000106.

Fujii, T., and T. Fukuchi (2005), *Laser remote sensing*, 888 pp., CRC Press, Florida.

Garcia, R. R., and W. J. Randel (2008), Acceleration of the Brewer-Dobson circulation due to increases in greenhouse gases, *J. Atm. Sci*., *65*, 2731-2739.

Gerrard, A. J., T. J. Kane, J. P. Thayer, T. J. Duck, J. A. Whiteway, J. Fiedler (2002), Synoptic scale study of the Arctic polar vortex's influence on the middle atmosphere, 1, observations, *J. Geosphys. Res.*, *107* (D16), doi:10.1029/2001JD000681.

Grant, W. B., E. V. Browell, R. T. Menzies, K. Sassen, and C. Y. She, eds. (1997), *Laser applications in remote sensing*, 527-560 pp., SPIE Milestones Series (MS 141), SPIE.

Harvey, V. L., and M. H. Hitchman (1996), A climatology of the Aleutian high, *J. Atmos. Sci*., *53* (14), 2088-2101.

Harvey V. L., R. B. Pierce, T. D. Fairlie, and M. H. Hitchman (2002), A climatology of stratospheric polar vortices and anticyclones, *J. Geophys. Res., 107*(D20), 4442, doi:10.1029/2001JD001471.

Hauchecorne, A., J.-L. Bertaux, F. Dalaudier, J. M. Russel III, M. G. Mlynczak, E. Kyrölä, and D. Fussen (2007), Large increase of NO_2 in the north polar mesosphere in Janaury-February 2004: Evidence of a dynamical origin from GOMOS/ENVISAT and SABER/TIMED data, *Geophys. Res. Lett.*, *34*, L03810, doi:10.1029/2006GL027628.

Hauchecorne, A., and M. L. Chanin (1980), Density and temperature profiles obtained by lidar between 35 and 70 km, *Geophys. Res. Lett.*, *7*, 565-568.

Hecht, J. (1992), *The Laser Guidebook*, McGraw-Hill Inc, 498 pp., New York.

Hedin, A. E. (1991), Extension of the MSIS thermospheric model into the middle and lower atmosphere, *J. Geophys. Res*., *96*, 1159-1172.

Holton, J. R. (2004), *An introduction to dynamic meteorology*, 535 pp. Elsevier Academic Press, Massachusetts.

Holton, J. R., and M. J. Alexander (2000), The role of waves in the transport circulation of the middle atmosphere, in *Atmospheric Science Across the Stratopause*, *Geophys*. *Monogr*. *Ser*., vol. 123, edited by D. E. Siskind, S. D. Eckermann, and M. E. Summers, pp. 21-35, AGU, Washington, D. C.

Holton, J. R., P. H. Haynes, M. E. McIntyre, A. R. Douglass, R. B. Rood, L. Pfister (1995), Stratosphere-troposphere exchange, *Rev. Geophys*., *33* (4), doi:10.1029/95RG02097.

Houghton, J. T. (1986), *The physics of atmospheres*, Cambridge University Press, 271 pp., Great Britain.

Houghton, J. T. (1978), The stratosphere and mesosphere, *Quart. J. Royal Met. Soc*., *104*, 1-29.

ICSU (International Council for Science) (2004), *A framework for the International Polar Year 2007-2008*, 73 pp, www.ipy.org.

Keckhut, P., A. Hauchecorne, M. L. Chanin, Midlatitude long-term variability of the middle atmosphere: Trends and cyclic and episodic changes, *J. Geophys. Res*., *100*, 18,887-18,897, 1995.

Kent, G. S., B. R. Clemesha, R. W. Wright (1967), High altitude atmospheric scattering of light from a laser beam, *J. Atmosph. Terr. Phys.*, *29*, 169-181.

Labitzke, K. (1972), Temperature changes in the mesosphere and stratosphere connected with circulation changes in winter, *J. Atmos. Sci.*, *29*(4), 756-766.

Liu, H.-L., D. R. Marsh, C.-Y. She, Q. Wu, and J. Xu (2009), Momentum balance and gravity wave forcing in the mesosphere and lower thermosphere, *Geophys. Res. Lett.*, 36, L07805, doi:10.1029/2009GL037252.

Manney, G. L., K. Kruger, J. L. Sabutis, S. A. Sena, and S. Pawson (2005), The remarkable 2003-2004 winter and other recent winters in the Arctic stratosphere since the late 1990s, *J. Geophys. Res.*, *110*, D04107, doi:10.1029/2004JD005367.

Matzuno, T. (1971), A dynamical model of the stratospheric sudden warming, *J. Atm. Sci*., *28*(8), 1479-1494.

Measures, R. M. (1984), *Laser remote sensing fundamentals and applications*, 510 pp. Wiley-Interscience, Florida

Mertens, C. J., F. J. Schmidlin, R. A. Goldberg, E. E. Remsberg, W. D. Pesnell, J. M. Russell III, M. G. Mlynczak, M. Lopez-Puertas, P. P. Wintersteiner, R. H. Picard, J. R. Winick, and L. L. Gordley (2004), SABER observations of mesospheric temperatures and comparisons with falling sphere measurements taken during the 2002 summer MaCWAVE campaign, *Geophys. Res. Lett*., *31*(3), L03105, doi:10.1029/2003GL018605.

Mizutani, K., T. Itabe, M. Yasui, T. Aoki, Y. Murayama, and R. L. Collins (2000), Rayleigh and Rayleigh Doppler lidars for the observations of the Arctic middle atmosphere, *IEICE Trans. Fundam. Electron. Commun. Comput. Sci.,* E83-B, 2003.

Murayama, Y., M. Ishii, M. Kubota, M. Hirotaka, K. Mizutani, S. Ochiai, Y. Kasai, S. Kawamaura, Y. Tanaka, H. Masuko, T. Iguchi, H. Kumagai, T. Kikuchi, K. Sata, R. L. Collins, B. J. Watkins, M. Conde, W. B. Bristow, and R. W. Smith (2007), Comprehensive Arctic atmosphere observing system and observed results for system performance demonstration, *J. Nat. Instit. Info. Comms. Tech*, *54*(1/2), 5-16.

Nadakuditi, S. (2005), *Spectral estimation of wave-driven fluctuations in Rayleigh lidar temperature measurements*, MS Thesis, University of Alaska Fairbanks.

NRC (National Research Council) (2004), *A vision for the International Polar Year 2007-2008*, pp 96, National Academy Press, Washington D. C.

Ramaswamy, V., M.-L. Chanin, J. Angell, J. Barnett, D. Gaffen, M. Gelman, P. Keckhut, Y. Koshelkov, K. Labitzke, J.-J. R. Lin, A. O'Neill, J. Nash, W. Randel, R. Rood, K. Shine, M. Shiotani, and R. Swinbank (2001), Stratospheric temperature trends: Observations and model simulations, *Rev. Geophys*., *39*(1), doi:10.1029/1999RG000065.

Russell, J. M. III, M. G. Mlynczak, L. L. Gordley, J. Tansock, and R. Esplin (1999), An overview of the SABER experiment and preliminary calibration results, *Proceedings of the SPIE*, 44th Annual Meeting, Denver, Colorado, July 18-23, *3756*, 277-288.

Scaife, A. A.., J. R. Knight, G. K. Vallis, and C. K. Folland (2005), A stratospheric influence on the winter NAO and North Atlantic surface climate, *Geophys. Res. Lett., 32*(18)*,* L18715, doi:10.1029/2005GL023226.

Shibata, T., K. Sato, H. Kobayashi, M. Yabuki and M. Shiobara (2003), Antarctic polar stratospheric clouds under temperature perturbation by nonorographic inertia gravity waves observed by micropulse lidar at Syowa Station*, J. Geophys. Res.*, 108, D3, 4105, doi:10.1029/2002JD002713.

Sica R. J., M. R. M. Izawa, K. A. Walker, C. Boone, S. V. Petelina, P. S. Argall, P. Bernath, G. B. Burns, V. Catoire, R. L. Collins, W. H. Daffer, C. De Clercq, Z. Y. Fan, B. J. Firanski, W. J. R. French, P. Gerard, M. Gerding, J. Granville, J. L. Innis, P. Keckhut, T. Kerzenmacher, A. R. Klekociuk, E. Kyrö, J. C. Lambert, E. J. Llewellyn, G. L. Manney, I. S. McDermid, K. Mizutani, Y. Murayama, C. Piccolo, P. Raspollini, M. Ridolfi, C. Robert, W. Steinbrecht, K. B. Strawbridge, K. Strong, R. Stübi, and B. Thurairajah (2008), Validation of the Atmospheric Chemistry Experiment (ACE) version 2.2 temperature using ground-based and space-borne measurements, *Atmos. Chem. Phys*., *8*, 35-62.

Silfvast, W. T. (1996), *Laser Fundamentals*, Cambridge University Press, 521 pp., New Delhi.

Siskind, D. E., S. D. Eckermann, L. Coy, J. P. McCormack, and C. E. Randall (2007), On recent interannual variability of the Arctic winter mesosphere: Implications for tracer decent, *Geophys. Res. Lett., 34,* L09806, doi:10.1029/2007GL029293.

Solomon, S. (1999), Stratospheric ozone depletion: A review of concepts and history, *Rev. Geophys.*, *37* (3), doi:10.1029/1999RG900008.

Strutt, J. W. (Lord Rayleigh) (1899), On the transmission of light through an atmosphere containing small particles in suspension, and on the origin of the blue of the sky, *Phil. Mag. XLVII*, pp. 375-384.

Taylor, M. J., Y. Zhao, P. -D. Pautet, M. J. Nicolls, R. L. Collins, J. Barker-Tvedtness, C. D. Burton, B. Thurairajah, J. Reimuller, R. H. Varney, C. J. Heinselman, K. Mizutani (2009), Coordinated optical and radar image measurements of noctilucent clouds and polar mesospheric summer echoes, *J. Atmos. Sol.-Terr. Phys*., *71*, 675-687.

Thurairajah, B., R. L. Collins, and K. Mizutani (2009a), Multi-Year temperature measurements of the middle atmosphere at Chatanika, Alaska (65°N, 147°W), *Earth Planets Space*, *61(6)*, 755-764.

Thurairajah, B., R. L. Collins, V. L. Harvey, R. S. Lieberman, K. Mizutani (2009b), Rayleigh lidar observations of reduced gravity wave activity during the formation of an elevated stratopause in 2004 at Chatanika, Alaska (65°N, 147°W), *submitted to J. Geophys. Res.,* 2009JD013036.

Thurairajah, B., R. L. Collins, V. L. Harvey, R. S. Liebermann, M. Gerding , J. M. Livingston (2009c), Gravity wave activity in the Arctic stratosphere and mesosphere during the 2007-2008 and 2008-2009 stratospheric sudden warmings, *paper in preparation for submission to J. Geophys. Res.*

Wang, W. (2003), *Spectral estimation of signal and noise power in Rayleigh lidar measurements of the middle atmosphere*, MS Thesis, University of Alaska Fairbanks.

Weitkamp, C. (2005), *Lidar: Range resolved optical remote sensing*, 460 pp., Springer, Singapore.

Wilson, R., M. L. Chanin, and A. Hauchecorne (1991a), Gravity waves in the middle atmosphere observed by Rayleigh lidar 1. Case studies, *J. Geophy. Res., 96*(D3), 5153-5167.

Wilson, R., M. L. Chanin, and A. Hauchecorne (1991b), Gravity waves in the middle atmosphere observed by Rayleigh lidar 2. Climatology, *J. Geophy. Res., 96*(D3), 5169-5183.

Table 1.1. Specifications of NICT Rayleigh lidar system at Chatanika, Alaska (65°N, 147°W).

Transmitter	
1. Laser	Nd:YAG
a. Model	Continuum Powerlite 8020
b. Wavelength (λ_L)	532 nm
c. Repetition Rate (R_L)	20 Hz
d. Pulse Energy (E_L)	460 mJ
e. Pulse Width	5-7 ns
f. Line Width	1.0 cm^{-1}
2. Beam Expander	x 10
3.Divergence	0.45 mrad
Receiver	
4. Telescope	Newtonian
a. Diameter	60 cm
b. Range Resolution	75 m
5. Optical Bandwidth	0.3 nm
6.Detector	Photomultiplier Tube
a. Model	Hamamatsu R3234-01
7. Preamplifier Gain	x 5
a. Model	Stanford Research Systems SR445
b. Bandwidth	300 MHz
8. Digital Recorder	Multichannel Scalar
a. Model	Ortec Turbo MCS T914
b. Maximum Count Rate	150 MHz

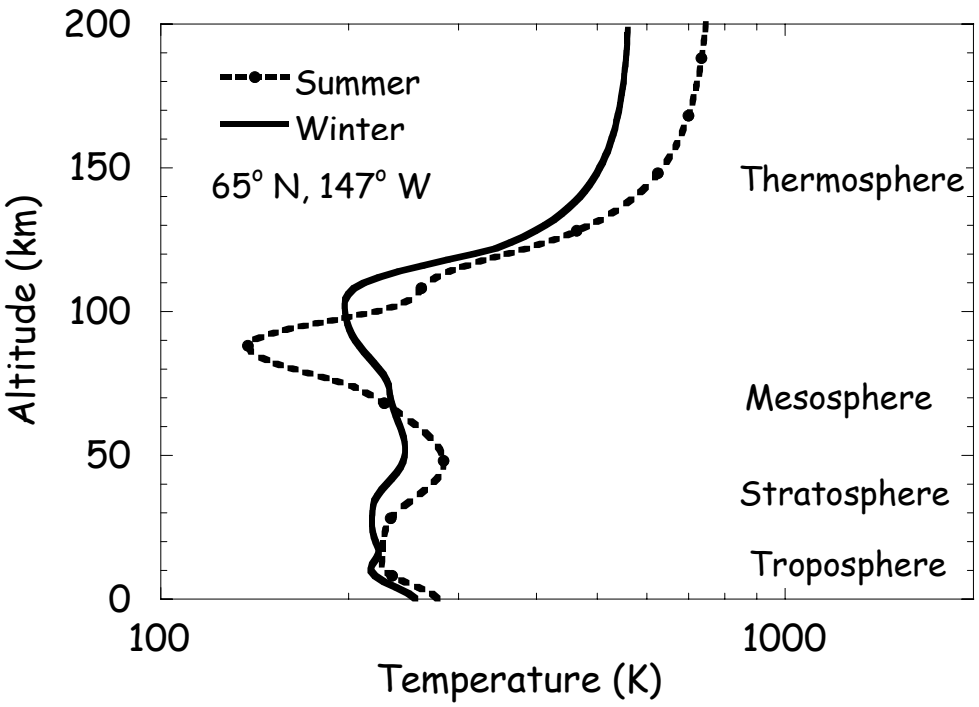

Figure 1.1. The atmospheric temperature profile for Fairbanks, Alaska (65^{o}N, 147^{o}W) in summer and winter. The data is obtained from the Extended Mass Spectrometer Incoherent Scatter (MSISE-90) model [*Hedin*, 1991] and is for 21st June 2008 (summer) and 21st December 2008 (winter)

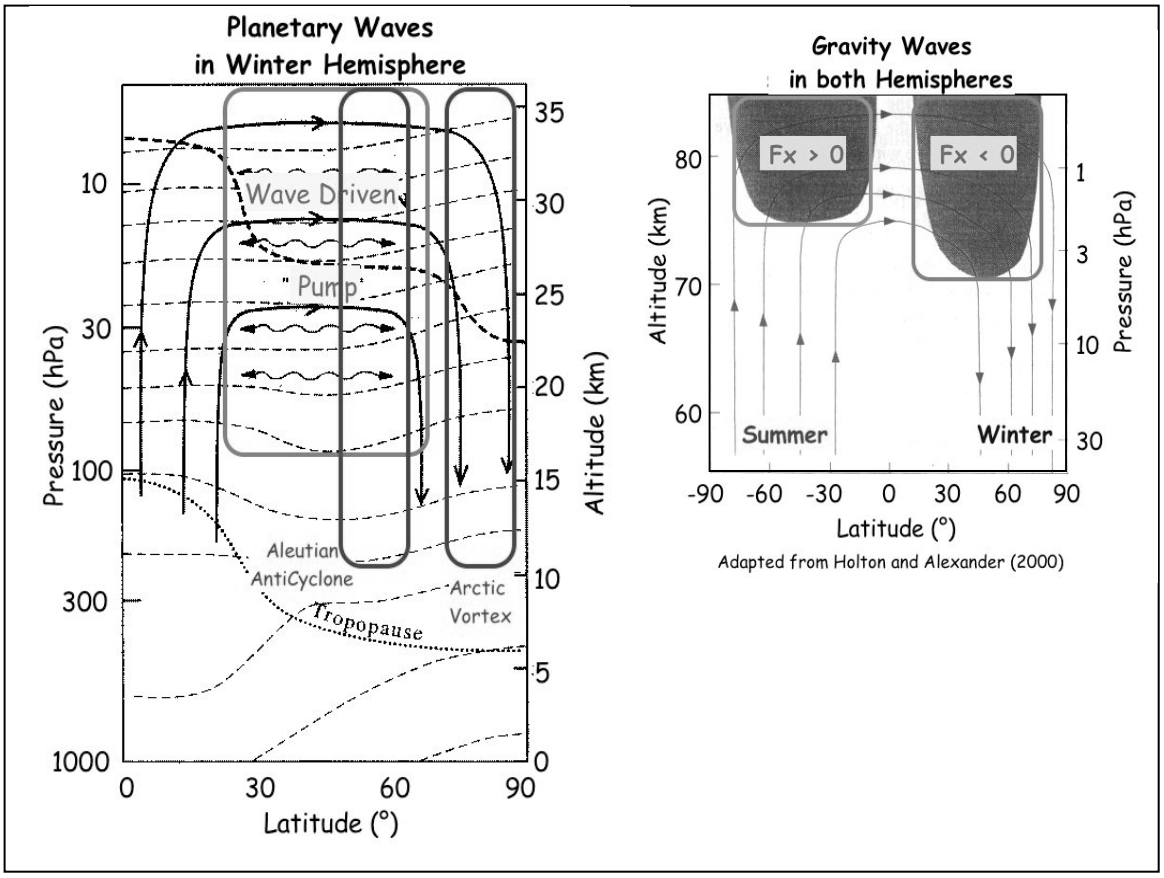

Figure 1.2. The wave driven middle atmospheric circulation (adapted from *Holton and Alexander*, [2000]). (Left) equator to pole planetary wave driven circulation and (right) pole to pole gravity wave driven circulation. Shading indicates region of gravity wave breaking and *Fx* denotes zonal forcing direction i.e. eastward forcing in summer hemisphere and westward forcing in winter hemisphere.

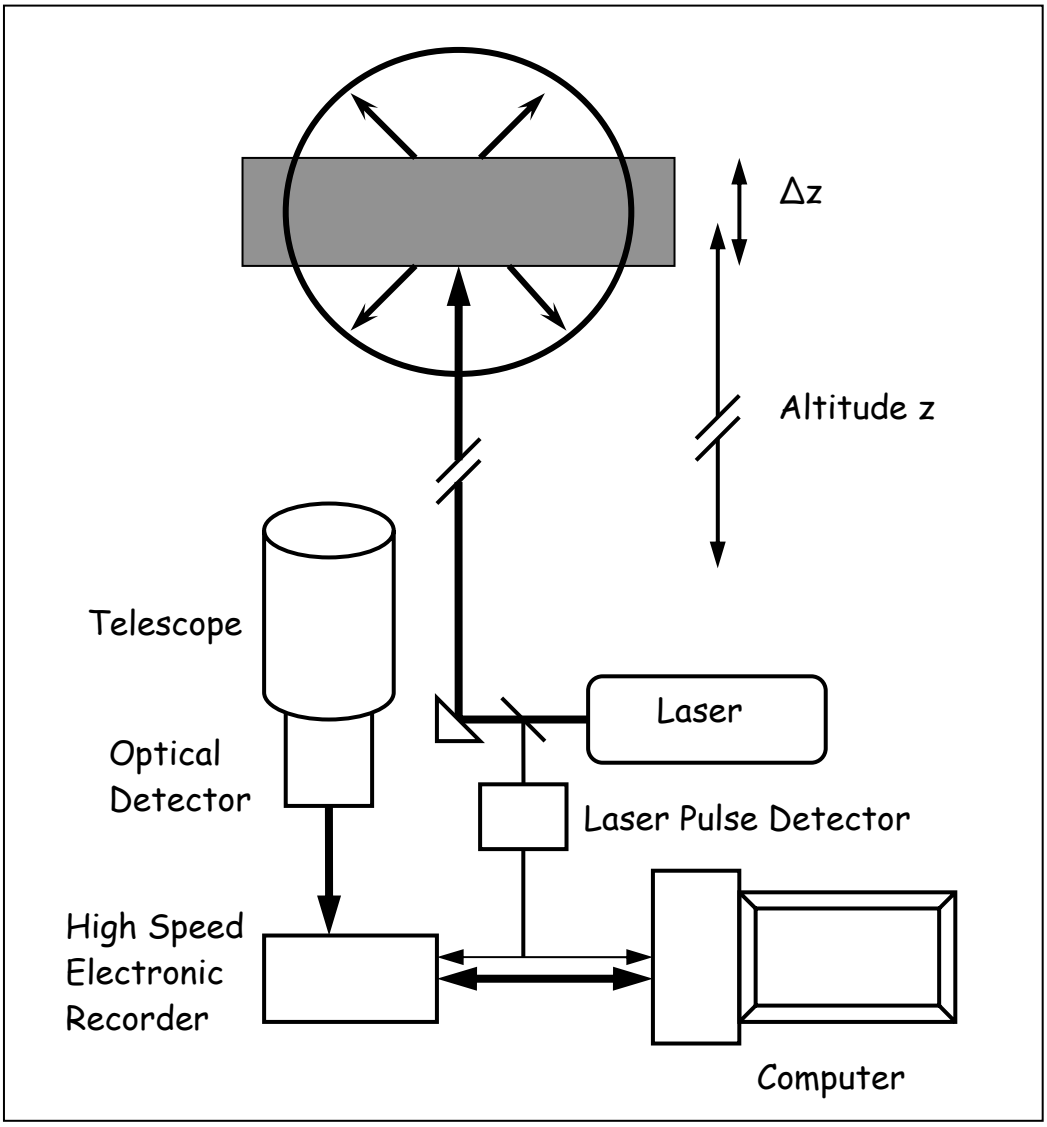

Figure 1.3. Schematic of a Rayleigh lidar system

Chapter 2. Multi-Year Temperature Measurements of the Middle Atmosphere at Chatanika, Alaska (65°N, 147°W)[1]

Abstract. Over an eight-year period (1997-2005) Rayleigh lidar temperature measurements of the stratosphere and mesosphere (40-80 km) have been made at Poker Flat Research Range, Chatanika, Alaska (65°N, 147°W). The Rayleigh lidar measurements have been made between mid-August and mid-May. These measurements have yielded a total of approximately 904 hours of temperature measurements of the middle atmosphere over 116 nights. The seasonal evolution of the middle atmosphere shows an annual cycle with maximum in summer below 60 km and a reversal of the cycle with minimum in summer above 60 km. The monthly mean stratopause has a highest temperature of 273 K at an altitude of 47.5 km in May and a lowest temperature of 243 K at an altitude of 54.7 km in January. However, nightly stratopause temperatures in January and December are sometimes warmer than those in May and August. An elevated stratopause (> 65 km) is observed on 5 occasions in 41 observations in January and February. The Chatanika measurements are compared with five other Arctic data sets and models. The upper stratosphere at this site is slightly colder than the zonal mean as well as sites in Greenland and Scandinavia with the largest differences found in January. We discuss the wintertime temperatures in the upper stratosphere and lower mesosphere in terms of the position of the polar vortex and the increased occurrence of stratospheric warming events during the 1997-2005 observation period.

---

[1]Thurairajah, B., R. L. Collins, K. Mizutani (2009), Multi-Year temperature measurements of the middle atmosphere at Chatanika, Alaska (65^{o}N, 147^{o}W), *Earth Planets Space*, *61*(6), 755-764.

2.1. Introduction

Measurements of middle atmosphere temperature support empirical studies of the climate and climate variability. Observations also constrain the behavior of numerical models. Since the mid-1980s, studies of trends in stratospheric temperatures have been recognized as a critical component in assessing changes in the stratospheric ozone layer (see reviews by Solomon, 1999; Ramaswamy *et al*., 2001; and references therein; WMO, 2007). Studies of coupling between the stratosphere and troposphere suggest that zonal-mean circulation anomalies propagate downward from the upper stratosphere into the troposphere over the course of the winter, and that inclusion of the stratosphere in numerical prediction models can improve the accuracy of tropospheric forecasts (Boville, 1984; Baldwin and Dunkerton, 1999; Baldwin *et al*., 2007; and references therein). For example, Scaife *et al*. (2005) have used model simulations to study the link between stratospheric circulation and trends in the North Atlantic Oscillation (NAO) from the 1960s to the 1990s. The results from this simulation showed that a strengthening of the stratospheric winter jet caused a strengthening of the tropospheric westerlies in the mid to high latitudes, a weakening of the westerlies at low latitudes, and an increase in the NAO index. These topics have motivated the World Climate Research Program to investigate the effects of the middle atmosphere on climate, and support the project Stratospheric Processes And their Role in Climate (SPARC) (Pawson *et al*., 2000). The SPARC program has conducted an intercomparison study of contemporary and historical datasets to determine relative biases in middle atmosphere climatologies and has published a reference atlas of temperature and zonal-wind based on several of these datasets (SPARC, 2002; Randel *et al*., 2004).

Climatologies of the polar middle atmosphere have been challenging due to paucity of ground-based observations and seasonal limitations on space-based occultation methods. Furthermore, while the structure of the wintertime Antarctic middle atmosphere circulation is zonally symmetric, the structure of the wintertime Arctic middle atmosphere is zonally asymmetric (see comparative presentation of the structure of polar vortices in the northern and southern hemispheres by Schoeberl *et al.*, 1992).

The Arctic stratospheric vortex is primarily found in the eastern Arctic, while the Aleutian anti-cyclone is the dominant feature in the western Arctic. There is significant interaction between these systems during the winter that maintains a zonally asymmetric circulation (Harvey *et al*., 2002). During the winter, the structure of the Arctic stratosphere and mesosphere is also disturbed by stratospheric warming events (Labitzke, 1972). During major stratospheric warmings the zonal mean configuration of the circulation is disrupted (the stratospheric temperatures increase, the height of the stratopause changes, and zonal-mean zonal wind reverses). Up to the mid-1980s, major stratospheric warming events had been reported on an average every other year in the Arctic, while none had been reported in the Antarctic (see review by Andrews *et al*., 1987). No major warmings were reported in the Arctic from 1990-1998 while seven major warmings have been reported from 1999 to 2004 (Manney *et al*., 2005). The first reported Antarctic major stratospheric sudden warming occurred in 2002 (Allen *et al*., 2003) with an associated cooling in the mesosphere (Hernandez, 2003; Siskind *et al*., 2005). Thus, the definition of a zonally symmetric middle-atmosphere climatology for the Arctic is particularly challenging.

In this study we present multi-year measurements of the stratospheric and mesospheric temperature profile from a site in the western Arctic at Chatanika, Alaska (65°N, 147°W). These temperature measurements have been made with a Rayleigh lidar system that has been operated on an ongoing basis from November 1997 through April 2005. We present monthly mean temperature profiles for all months except June and July. We discuss the variability in these measurements. We compare these measurements with climatologies and seasonal data sets from ground-based measurements at other sites in the Arctic (Lübken and von Zahn, 1991; Lübken, 1999; Gerrard *et al*., 2000), the SPARC reference atlas (SPARC, 2002), the Extended Mass Spectrometer and ground-based Incoherent Scatter (MSISE-90) model (Hedin, 1991), and from satellite measurements (Clancy *et al*., 1994). We discuss the monthly temperatures in terms of zonal asymmetry, movement of the polar vortex, inter-annual variability of the Arctic middle atmosphere, and stratospheric warming events.

2.2. Rayleigh Lidar Technique

The National Institute of Information and Communications Technology (NICT) Rayleigh lidar was installed at Poker Flat Research Range (PFRR), Chatanika, Alaska in November 1997. NICT and the Geophysical Institute (GI) of the University of Alaska Fairbanks (UAF) jointly operate this Rayleigh lidar. The lidar observations were initiated during the Alaska Project, a ten-year international program of observations of the Arctic middle and upper atmosphere (Murayama *et al*., 2007).

The NICT Rayleigh lidar system consists of a Nd:YAG laser, a 0.6 m receiving telescope with a field-of-view of 1 mrad, a narrowband optical filter (bandwidth of either 1 nm or 0.3 nm FWHM), a photomultiplier tube, a photon counting detection system, and a computer-based data acquisition system (Mizutani *et al.*, 2000; Collins *et al.*, 2003). The lidar is a fixed zenith-pointing system. The laser operates at 532 nm with a pulse repetition rate of 20 pps, the laser pulse width is 7 ns FWHM, and the average laser power is 10 W. The photon counts are integrated over 0.5 μs yielding a 75 m range sampling resolution. The raw photon count profiles are acquired every 50 s or 100 s representing the integrated echo from 1000 or 2000 laser pulses respectively. In the Rayleigh lidar technique like the searchlight technique (Elterman, 1951), we assume that the intensity profile of the scattered light is proportional to the density of the atmosphere, and the atmosphere is in hydrostatic equilibrium. The raw photon count signal can be described as a Poisson random variable (Pratt, 1969). We logarithmically smooth the raw photon count profile with a 2 km running average to reduce the uncertainty in the signal due to photon counting noise (see Papoulis and Pillai, 2002 for review of random variables and associated signal processing). We then correct the photon count profile for extinction due to Rayleigh scatter (Wang, 2003; Nadakuditi, 2005). We finally determine the Rayleigh lidar temperature profiles from the photon count profiles under standard inversion techniques by downward integration of the density profile with the assumption of an initial temperature at the upper altitude of 80 km (Leblanc *et al.*, 1998). In this study we use the temperatures from the SPARC reference atlas to initialize the lidar temperature profiles. Thus the total uncertainty in the temperature estimate has two

sources; the uncertainty in the initial temperature estimate (assumed to be 25 K), and the statistical uncertainty in the raw photon count signal. The total uncertainty gives the accuracy in the absolute value of the temperature values while the statistical uncertainty in the raw lidar data gives the relative accuracy of the temperature in a given profile. The lidar signal increases with decreasing altitude and the lowest altitude is determined by the maximum photon counting rate (150 million counts per second) of the receiver. In these studies the lidar signal at 40 km is equivalent to 1-2 million counts per second and the photon counting receiver records the lidar signal accurately (Donovan *et al.*, 1993).

We plot an example of a Rayleigh lidar temperature measurement in Fig. 2.1. This is the temperature measured over a 2 h period on the night of 22-23 January 2003. We derived this lidar temperature profile from the lidar profile integrated over 63 individual raw photon count profiles (each representing the integrated signal of 2000 laser pulses) that were acquired between 2329 and 0130 LST (0829 – 1030 UT (LST = UT – 9 h)). The initial temperature, from the SPARC reference atlas at 80 km, contributes 100% of the temperature estimate at 80 km, 21% of the temperature estimate at 70 km, 4% at 60 km, and 1% at 50 km. The uncertainty in the temperature due to the initial temperature estimate decreases with decreasing altitude. An uncertainty of 10 K in the initial temperature at 80 km yields an error of 2.1 K at 70 km, 0.6 K at 60 km, and 0.2 K at 50 km. We plot the temperature profile bounded by the standard deviation of the total uncertainty due to the combination of the uncertainty in the photon count signal and the uncertainty in the initial temperature at 80 km. The stratopause is at an altitude of 50.2 km and has a temperature of 251.6 K (±0.7 K). A mesospheric inversion layer (MIL) is at an altitude near 60 km with characteristics typical of MILs reported from PFRR (Cutler *et al*., 2001). This MIL has a maximum at 60.5 km with a temperature of 235.0 K (±1.9 K) and a minimum at 58.3 km with a temperature of 222.4 K (±1.5 K). The lapse rate on the topside (61.0-62.0 km) of the MIL is –6.2 K/km. In summary the mesospheric inversion layer has a depth of 2.2 km and amplitude of 12.6 K (±1.7 K). There is a deep temperature minimum of 194.5 K (± 5.4 K) in the mesosphere at 69.1 km. There is also a shallow temperature minimum of 232.4 K (±0.3 K) in the stratosphere at 41.7 km.

We also plot the temperature profile measured by the Sounding of the Atmosphere using Broadband Emission Radiometry (SABER) instrument aboard the Thermosphere Ionosphere Mesosphere Energetics Dynamics (TIMED) satellite (Mertens *et al*., 2004; Mertens *et al*., 2001; Russell *et al*., 1999) in Fig. 2.1. The SABER temperature retrieval is Level 2A version 1.06. The SABER temperature measurement was made at 0030 LST approximately 270 km northeast (67°N, 146°W) of the Rayleigh lidar. The SABER temperature profile is reported at a vertical resolution of 0.4 km and represents a measurement profile over 1.7° of latitude and 6.9° of longitude (Beaumont, 2007). We compare the lidar and SABER measurements at 1 km resolution. The temperature profiles measured by lidar and satellite show the same general structure; the stratopause is near 50 km, there is a MIL near 60 km, the deep temperature minimum near 70 km, and the shallow temperature minimum in the stratosphere near 42 km. The deep temperature minimum at 70 km is not the mesopause. The SABER profile shows a mesopause temperature minimum of 171 K at 102 km with temperatures steadily increasing above this altitude up to the highest measurement of 605 K at 155 km. The mesopause altitude has a value typical of midwinter conditions when the mesopause is usually found at approximately 100 km as opposed to at 80 km in summer (e.g., Senft *et al*., 1994). The lidar temperature at the stratopause is 0.02 K warmer than the SABER stratopause temperature. The lidar measurement is on average warmer than the SABER measurement with an average difference of 2.6 K (4.3 K rms) between 40 and 70 km. The largest difference of 12.5 K is found at 60 km. The differences in the structure of the MIL measured by the lidar and SABER are within the spatial variations expected for MILs where the amplitudes of the inversions can vary by 10 K over hundreds of km (Leblanc *et al*., 1995).

We also plot the SPARC temperature profile for the month of January and the MSISE-90 temperature profile for local midnight on 22 January 2003 in Fig. 2.1. Clearly the lidar measurements indicate that the mesosphere is colder than both the SPARC and MSISE-90 profiles suggest. The fact that mesospheric temperatures in the Arctic are colder than those suggested by MSISE-90 has been noted in studies of noctilucent clouds

at PFRR (Collins *et al.,* 2003). We again compare the temperature profiles at 1 km resolution. The lidar temperature profile is on average 11.1 K less than the SPARC profile in the 40-70 km altitude region with a maximum difference of 21.4 K at 69 km. The lidar temperature at the stratopause is 0.4 K warmer than the SPARC stratopause temperature. The lidar temperature profile is on average 10.1 K less than the MSISE-90 profile in the 40-70 km altitude region with a maximum difference of 34.8 K at 69 km. The lidar temperature at the stratopause is 6.9 K warmer than the MSISE-90 stratopause temperature.

We have also compared the Rayleigh lidar temperature measurements at Chatanika with temperature retrievals from the Atmospheric Chemistry Experiment Fourier Transform Spectrometer (ACE-FTS) onboard the SCISAT-1 satellite. Coincident measurements by both instruments report the same temperature structure with agreement in the measurement of the stratopause and MILs (Sica *et al*., 2008). The temperature differences between the lidar and ACE-FTS measurements are less than 5 K in the 40-70 km altitude region.

2.3. Rayleigh Lidar Measurements

Rayleigh lidar measurements of the upper stratosphere and mesosphere have been made in autumn, winter, and spring from November 1997 to April 2005. These observations made each year from August to May have yielded 116 individual nighttime measurements lasting between three and fifteen hours for a total of 904 hours of observations (Fig. 2.2). The average observation period lasted 7.8 h. While Chatanika is below the Arctic Circle, the background light levels in summer twilight prevent measurements by this lidar in June and July.

We average the nightly mean profiles for each month to form the monthly mean profile. To study the temperature variability in the mean monthly middle atmosphere temperature profiles we determine the sample standard deviation of the temperature measurements for each month at each altitude. We plot the individual and mean monthly profiles for January, March, December, and April in Fig. 2.3. The variability in winter

(January and December) is much greater than in springtime (March and April). January and March have similar numbers of observations (22 and 29 respectively) and December and April have the same number of observations (nine each). We also plot the sample standard deviation of the nightly temperature measurements at each altitude in Fig. 2.3. The rms variability of the temperatures averaged over the 40-70 km altitude region is greater in December (14 K) and January (14 K) than in April (6 K) and March (9 K). The uncertainty in the sample mean temperatures is typically less than 5K.

We plot the monthly variation of the altitude and temperature of the stratopause in Fig. 2.4. We also plot the individual measurements for comparison. The monthly mean stratopause varies between altitudes of 47.5 km and 54.7 km and temperatures of 243 and 273 K. The stratopause is highest in December and January and warmest in May. The individual nightly measurements show much greater variability than the monthly means. On a nightly basis the stratopause varies in altitude from 40.8 km to 71.1 km and in temperature from 230 K to 286 K. The wintertime variability is clearly evident in Fig. 2.4. The highest stratopause temperature was measured in early December while the lowest was measured in late January. The highest stratopause altitude was detected in early January while the lowest was detected in late February. We plot the monthly variation of the temperature at 45 km, 55 km, and 65 km in Fig. 2.5, and the individual measurements for comparison. The monthly mean temperature at 45 km has a pronounced annual cycle with an average value of 249 K, a maximum of 270 K in May, and a minimum of 231 K in January. The seasonal variation of 39.5 K is larger than the rms variation of 12.6 K. The monthly mean temperature at 55 km has a less pronounced annual cycle with an average value of 251 K, a maximum of 264 K in May, and a minimum of 240 K in February. The seasonal variation of 24.4 K is larger than the rms variation of 8.3 K. The monthly mean temperature at 65 km has no clear annual cycle with an average value of 230 K, a maximum of 235 K, and a minimum of 222 K. The annual variation of 12.9 K is larger than the rms variation of 4.2 K. The wintertime nightly variability is again clearly evident at all altitudes. We see that nightly wintertime temperatures can be as warm as late spring and early fall temperatures at all altitudes.

We plot the monthly variation in the rms variability over the 40-70 km altitude range in Fig. 2.6. These rms values represent the rms of the standard deviations over the given altitude ranges. We subtract the variance due to measurement error from the total sample variance to give the geophysical variance. The yearly average value of the variability is 9 K with a maximum value of 14 K in December and a minimum of 4 K in September. The rms variability appears to have an annual variation with largest values in winter. There does not appear to be any systematic or significant variation of the variability with altitude. The annual variation does not appear to be function of the number of observations in each month. The decrease through January, February and March and the increase through November and December occur when there are similar numbers of samples in each month (Fig. 2.2). The months with lowest number of samples (May through October) have smaller rms variability than would be expected from their sample statistics.

We present the monthly average temperature climatology of the upper stratosphere and mesosphere at PFRR, Chatanika, Alaska as a false color plot in altitude and time in Fig. 2.7. The pronounced annual cycle in temperatures, with a maximum in May and minimum in January, is clearly seen up to ~60 km. The highest temperature of 273 K is found at 47.5 km in May. The 47.5 km temperature has an annual range of 38 K with a minimum value of 235 K in January. The annual cycle is reversed at higher altitudes. The low temperatures in the upper stratosphere (40-50 km) in January are also evident. The location of the stratopause is plotted as a dashed line. The stratopause has a temperature of 273 K at an altitude of 47.5 km in May and a temperature of 243 K at an altitude of 54.7 km in January.

In Fig. 2.8 we plot the average vertical temperature profile measured at Chatanika for the month of January in 2004 and 2005. The January 2004 profile represents the average of three nights of observation on 5-6, 15-16, and 29-30 January. The three nightly profiles from 2004 correspond to three of the four highest stratopause altitudes recorded in January at Chatanika (Fig. 2.4 upper panel). The January 2005 profile represents the average of three nights of observation on 10-11, 18-19, and 27-28 January.

We also plot the average temperature profiles plus and minus the uncertainty in the sample mean value. The monthly average temperature profiles are significantly different. In 2005 the profile is more similar to the zonal mean profile at 64°N in the SPARC reference atlas (SPARC, 2002). In 2004 the profile shows an elevated stratopause and a colder stratosphere. In January 2004 the stratopause is located at 70.3 km with a temperature of 245.0 K while in 2005 the temperature is 221.8 K at 70.3 km. In January 2005 the stratopause is located at 47.5 km with a temperature of 261.4 K while in 2004 the temperature is 220.4 K at 47.5 km. The difference of 41.0 K at 47.5 km is significant as it is greater than the sum of the sample uncertainties in the average profiles and is 3.0 times greater than the rms variability at this altitude in the January data (Fig. 2.3). The difference of 23.2 K at 70.3 km is significant as it is greater than the sum of the sample uncertainties in the average profiles and is 1.6 times greater than the rms variability at this altitude in the January data (Fig. 2.3). The two high values (67.2 km and 68.5 km) of the stratopause altitude measured in February (Fig. 2.4, upper panel) and the single high value (63.0 km) in December are associated with temperature profiles that have an elevated stratopause with a colder stratosphere. The high value of the stratopause altitude in October (64.2 km) is associated with the presence of a large amplitude MIL in the mesosphere and there is no apparent cooling of the stratosphere.

2.4. Comparison of Measurements from Chatanika with Other Arctic Measurements and Models

We compare the Rayleigh lidar monthly average temperatures with temperatures reported by the SPARC (2002) reference atlas and single site Rayleigh lidar measurement from Kangerlussuaq, Greenland (67^{o}N, 51^{o}W). We form the difference temperature by subtracting the SPARC temperature and Kangerlussuaq temperature from the temperature measured at Chatanika. We plot these differences in Fig. 2.9. Overall, Chatanika has a colder stratosphere and a slightly warmer mesosphere than the 64°N zonal mean temperatures reported by the SPARC reference atlas (upper panel). The largest difference is found in the stratosphere in January where the 42.3 km temperature is 20 K

colder at Chatanika than in the zonal mean. In November the pattern is reversed where the 51.1 km temperature is 5 K warmer at Chatanika than in the zonal mean. Given a sample uncertainty in the mean monthly temperature profiles at Chatanika of less than 5 K, significant temperature differences between Chatanika and the SPARC zonal mean are found in each month from August through April. The temperature measured at Chatanika is also generally lower than the temperature measured at Kangerlussuaq (lower panel). The largest difference is again found in the stratosphere in January where the 46.6 km temperature is 28 K lower at Chatanika than at Kangerlussuaq. The upper stratosphere and lower mesosphere in December are significantly cooler at Chatanika than at Kangerlussuaq, where the 64.0 km temperature is 24 K lower at Chatanika than at Kangerlussuaq. Given the sample uncertainty in the mean monthly temperature profiles at Chatanika, significant temperature differences between Chatanika and Kangerlussuaq are found in each month from September through March.

In Fig. 2.10 we plot the monthly variation of the altitude (upper panel) and temperature (lower panel) of the stratopause measured by the Rayleigh lidar at Chatanika with the stratopause altitude and temperature reported by other data sets and models (i.e., SPARC Reference atlas (SPARC, 2002), lidar measurements at Kangerlussuaq (67^{o}N, 51^{o}W) (Gerrard *et al*., 2000), falling spheres at Andoya (69°N, 16°E) (Lübken, 1999), lidar and in-situ density measurements at Andoya (Lübken and von Zahn, 1991), and MSISE-90 (Hedin, 1991)). The data sets show a variety of seasonal variations in the stratopause altitude from semiannual in the SPARC data to annual in the MSISE-90 data. The maximum values of the stratopause altitude are found in winter. The range of values in each month varies between 3.8 km in April and 6.7 km in March. The lidar measurements of the stratopause altitude at Chatanika generally fall inside the range of values reported by the different data sets. The one exception is in January when the Chatanika lidar measurements report a value of 54.7 km and all other data sets lie between 49.6 km and 51.4 km. The data show an annual variation in the stratopause temperature, except for the measurements of Gerrard *et al*. (2000) and Lübken and von Zahn (1991) that show a secondary maximum in winter. All datasets show that the

warmest stratopause temperatures occur in summer. The range of values in each month varies between 3.6 K in April and 21.1 K in January. The stratopause temperatures at Chatanika are generally cooler than the other measurements with the most significant differences in January, February, and March.

In Fig. 2.11 we plot the monthly variation of the temperature at 45 km (upper panel), 55 km (middle), and 65 km (lower panel) measured by the Rayleigh lidar at Chatanika with the temperatures reported by the other data sets and models in Fig. 2.10 and the 65°N zonal mean satellite measurements (Clancy *et al*., 1994). The various data sets show an annual variation in the temperatures with a summer maximum. This annual variation is most pronounced at 45 km and decreases with increasing altitude. At 45 km, the largest range in temperatures is found in January when the temperature at Chatanika of 230.3 K is significantly lower (10.1 – 27.8 K) than all other measurements. At 55 km, the largest range is still found in January (even allowing for the unusually high temperatures reported by Lübken and von Zahn (1991)) when the temperature at Chatanika of 243.2 K is again the lowest but not significantly lower than MSISE-90. At 65 km, the largest range of values is found in November with the temperature at Chatanika within the range of the other measurements. In general, we find that the lidar measurements at Chatanika report colder temperatures in the upper stratosphere in January, February, March, September, October, and December than those reported from other sites and the global mean.

2.5. Discussion

The current study is based on 116 nights of lidar measurements from a single site distributed between mid-August and mid-May from 1997 through 2005. The Rayleigh lidar measurements at Chatanika show a high degree of variability in the nightly temperature profile (Figs. 2.4 and 2.5). In considering the significance of the monthly averages we consider how the extent of the Chatanika data set compares with the other single-site studies; Lübken and von Zahn (1991) based their study on 180 days of temperature measurements made in all months except April, May and September over

eleven years (1980-1990), Lübken (1999) based his study on 89 measurements made between the end of April and end of September over eleven years (1987-1997), Gerrard *et al*. (2000) based their study on ~179 measurements made in all months except June over four years (1995-1998). For example, the monthly average profiles for January are based on 22 profiles at Chatanika, 30 profiles at Kangerlussuaq (Gerrard *et al*., 2000), and 29 profiles at Andoya (Lübken and von Zahn, 1991). The difference in January, February and March between the upper stratosphere temperatures at Chatanika and the other measurements are statistically significant (Figs. 2.9, 2.10, and 2.11). We consider these differences in terms of the structure of the Arctic polar vortex and stratospheric warming events.

Duck *et al*. (2000) used Rayleigh lidar measurements at Eureka obtained during six wintertime campaigns from 1992-1993 to 1997-1998 to study the relationship between the thermal structure of the middle atmosphere and the location of the polar vortex. They compared measurements of middle atmosphere temperature profile at Eureka both when the vortex is overhead and when it is not. Duck *et al*. (2000) drew on 99 nights of temperature measurements to show that the upper stratosphere and lower mesosphere (39-70 km) is warmer and the lower stratosphere (10-39 km) is colder when the vortex is overhead. Conversely, when the vortex was not over Eureka they found that the upper stratosphere and lower mesosphere (39-70 km) is colder and the lower stratosphere (10-39 km) is warmer. The altitude of the stratopause remains relatively unchanged (49-53 km) during these changes in vortex position. The change in temperature is approximately 20 K at 50 km, 30 K at 25 km and 0 K at 39 km (their Fig. 2.5). Gerrard *et al*. (2002) have studied the temperature structure of the Arctic by combining tropospheric and stratospheric analyses from the National Center for Environmental Prediction with Rayleigh lidar measurements at Andoya, Eureka, and Kangerlussuaq. Gerrard *et al*. (2002) report night-to-night changes in temperature of 20-40 K in the upper stratosphere and lower mesosphere associated with motion of the stratospheric vortex. The observations of colder temperatures in the upper stratosphere and lower mesosphere in December, January and February at Chatanika (Figs. 2.9 and 2.11) are consistent with the

fact that Arctic polar vortex is predominantly found in the eastern Arctic closer to Andoya, Kangerlussuaq, and Eureka (e.g., Gerrard *et al*., 2000, Harvey *et al*., 2002). The fact that the differences between the single-site measurements at Chatanika and Kangerlussuaq are greater than between Chatanika and the zonal mean confirm this zonal asymmetry in the location of the polar vortex and the thermal structure of the Arctic middle atmosphere.

However, the observations in January 2004 and 2005 (Fig. 2.8) show that the colder middle atmosphere is associated with a large change in the stratopause altitude of 23 km. These observations in 2004 contribute to our observation that the average stratopause in January at Chatanika is found at a higher altitude and has a colder temperature than in the other data sets (Fig. 2.10). Thus, the colder temperatures found in the upper stratosphere in Chatanika in January relative to the zonal mean and Kangerlussuaq (Fig. 2.9) is due to factors other than the position of the polar vortex position. Manney *et al*. (2005) noted the fact that recent winters have been warmer in the Arctic lower stratosphere. During these winters, major stratospheric warmings were common (7 in 6 years) resulting in unusually high temperatures in the lower stratosphere and lower temperatures in the upper stratosphere and mesosphere. Manney *et al*. (2005) restricted their study to meteorological analyses that were capped at 1 hPa (~50 km). Manney *et al*. (2008a) report satellite and lidar measurements of stratospheric and mesospheric temperatures over Eureka in early 2004, 2005 and 2006. Their observations show that following major stratospheric warmings in 2004 and 2006 the vortex breaks down throughout the stratosphere, there is a complete disappearance of the warm stratopause, and subsequent reformation of a cool stratopause near 75 km. The elevated stratopause then descends and warms over a several week period. Siskind *et al*. (2007) use a global circulation model to show that the observations in 2006 are consistent with a circulation where the gravity-wave driven meridional circulation has been disrupted (recalling the earlier work on the separated polar winter stratopause of Hitchman *et al*. (1989)). As a result the lower stratosphere radiatively cooled and the stratopause appears near 0.01 hPa (~78 km) with a temperature of approximately 235 K in the daily zonal mean at 65°N. Manney *et*

al. (2008b) have subsequently documented the life-cycle of this 2006 major stratospheric warming event with data from the Microwave Limb Sounder and SABER over the whole northern hemisphere. They show that over a three-week period following the major warming there is a complete disappearance of the warm stratopause followed by reformation of a cooler stratopause near 75 km that warms and descends to the original pre-warming altitude. Furthermore Manney *et al.* (2008b) show that the elevated stratopause in 2006 varies with longitude and extends over about half the polar region. The fact that the mean monthly temperature profile for January 2004 shows an elevated stratopause is consistent with the fact that the disruption of the stratosphere following a major stratospheric sudden warming can last nearly a month.

The other Arctic observations come from earlier time periods; the SPARC atlas represents measurements from 1992-1997 (SPARC, 2002), Gerrard *et al.* (2000) present data from 1995-1998, Lübken (1999) presents data from 1987-1997, Lübken and von Zahn (1991) present data from 1980-1990, the MSISE-90 model is largely based on data from the 1960s through the 1980s (Hedin, 1991), and Clancy *et al*. (1994) present data from 1982-1986. Thus, the thermal structure associated with the colder temperatures in the upper stratosphere in January at Chatanika may reflect the contribution of years when the upper stratosphere and lower mesosphere were colder than expected due to the increased frequency of stratospheric warmings in the 1997-2005 period.

2.6. Conclusions

We have used an eight-year Rayleigh lidar temperature data over Chatanika, Alaska to document the temperature structure of the stratosphere and mesosphere in the western Arctic. Individual lidar measurements have been compared with satellite measurements and found in good agreement. The monthly mean lidar measurements at Chatanika show that the seasonal variations in the monthly mean temperatures follow the expected variations with an annual cycle with summer maximum and winter minimum (273 K at 47.5 km in May and 243 K at 54.7 km in January) below 60 km and an annual cycle with winter maximum and summer minimum above 60 km. However, the Chatanika

measurements reveal an upper stratosphere that is slightly colder than that reported from observations at sites in Scandinavia and Greenland and in satellite measurements of the zonal mean. The study highlights the high degree of variability in the wintertime middle atmosphere when the stratopause is sometimes warmer than in May and August.

The colder January and February temperatures are associated with an elevated stratopause (> 65 km) that is observed on 5 occasions in 41 observations in January and February. The measurements in January are significantly colder than reported from eastern Arctic sites and in the zonal mean. While this difference is consistent with the influence of the polar vortex in the eastern Arctic, we conclude that the significantly lower temperatures in the upper stratosphere in January at Chatanika may reflect the contribution of years when the upper stratosphere and lower mesosphere were colder than expected due to the increased frequency of stratospheric sudden warmings in the 1997-2005 period. A more comprehensive analysis of the contribution of the position of the polar vortex and stratospheric warming events to the observed thermal structure of the Arctic middle atmosphere would require a higher frequency of observations uniformly distributed across the Arctic. Such a detailed pan-Arctic multiyear analysis could be conducted using SABER data for the period starting in 2002.

Acknowledgments The authors thank the following University of Alaska students for their assistance in making the ongoing lidar observations; J. Breese, L. Cutler, T. Hao, S. Nadakuditi, K. Nowicki, M. Peshave, T. Stern, L. Su, W. Wang, and J. Yue. The authors thank K. Sakanoi for her assistance with the spring 2003 measurements. The authors acknowledge the SABER science and data processing teams for providing the SABER data presented in the paper. The authors thank R. S. Lieberman for helpful discussion and comments. The authors thank the staff at PFRR for their ongoing support of the lidar program. The authors acknowledge support from the United States National Science Foundation, under grants ARC 06-32387 and ATM 06-40340, and from the United States Airforce and Navy under the DMSP SSMIS Cal/Val Program,

under contract N00173-01-1-G901. PFRR is a rocket range operated by GI-UAF with support from NASA.

References

Allen, D. R., R. M. Bevilacqua, G. E. Nedoluha, C. E. Randall, and G. L. Manney, Unusual stratospheric transport and mixing during the 2002 Antarctic winter, *Geophys. Res. Lett.*, **30**(12), 1599, doi:10.1029/2003GL017117, 2003.

Andrews, D. G., J. R. Holton, and C. B. Leovy, *Middle atmosphere dynamics*, 489 pp., Academic Press Inc., New York, 1987.

Baldwin, M. P., M. Dameris, and T. G. Shepherd, How will the stratosphere affect climate change, *Science*, **316**, 1576-1577, 2007.

Baldwin, M. P., and T. J. Dunkerton, Propagation of Arctic oscillation from the stratosphere to the troposphere, *J. Geophys. Res.*, **104**(D24), 30937-30946, 1999.

Beaumont, K., SABER: Sounding of the atmosphere using broadband emission radiometry, http://saber.gats-inc.com/, data accessed June 2007.

Boville, B. A., The influence of the polar night jet on the tropospheric circulation in a GCM, *J. Atmos. Sci*., **41**(7), 1132-1142, 1984.

Clancy, R. T., D. W. Rusch, and M. T. Callan, Temperature minima in the average thermal structure of the middle mesosphere (70-80 km) from analysis of 40- to 92-km SME global temperature profiles, *J. Geophys. Res.*, **99**(D9), 190001-19020, 1994.

Collins R. L., M. C. Kelley, M. J. Nicolls, C. Ramos, T. Hou, T. E. Stern, K. Mizutani and T. Itabe, Simultaneous lidar observations of a noctilucent cloud and an internal wave in the polar mesosphere, *J. Geophys. Res.,* **108**(D8), 8435, doi:10.1029/2002JD002427, 2003.

Cutler L. J., R. L. Collins, K. Mizutani, and T. Itabe, Rayleigh lidar observations of mesospheric inversion layers at Poker Flat, Alaska (65 °N, 147° W), *Geophys. Res. Lett.*, **28**(8), 1467-1470, 2001.

Donovan, D. P., J. A. Whiteway, and A. I. Carswell, Correction for nonlinear photon-counting effects in lidar systems, *App. Opt.*, **32**(33), 6742-6753, 1993.

Duck, T. J., J. A. Whiteway, and A. I. Carswell, A detailed record of high Arctic middle atmospheric temperatures, *J. Geophys. Res*., **105**(D18), 22,909-22,918, 2000.

Elterman, L., The measurement of stratospheric density distribution with the searchlight technique, *J. Geophys. Res.*, **56**(4), 509-520, 1951.

Gerrard, A. J., T. J. Kane, and J. Thayer, Year-round temperature and wave measurements of the Arctic middle atmosphere for 1995-1998, *Atmospheric science across the stratopause*, D. E. Siskind, S. D. Eckermann, and M. E. Summers, AGU Monograph, 123, 2000.

Gerrard A. J., T. J. Kane, J. P. Thayer, T. J. Duck, J. A. Whiteway, and J. Fiedler, Synoptic scale study of the Arctic polar vortex's influence on the middle atmosphere, 1, Observations, *J. Geophys. Res.*, **107** (D16), 4276, doi:10.1029/2001JD000681, 2002.

Harvey V. L., R. B. Pierce, T. D. Fairlie, and M. H. Hitchman, A climatology of stratospheric polar vortices and anticyclones, *J. Geophys. Res.,* **107**(D20), 4442, doi:10.1029/2001JD001471, 2002.

Hedin, A. E., Extension of the MSIS thermospheric model into the middle and lower atmosphere, *J. Geophys. Res.*, **96**(A2), 1159, 1991.

Hernandez, G., Climatology of the upper mesosphere temperature above South Pole (90°S): Mesospheric cooling in 2002, *Geophys. Res. Lett.*, **30**(10), 1535, doi:10.1029/2003GL016887, 2003.

Hitchman, M. H., J. C. Gille, C. D. Rogers, and G. Brasseur, The separated polar winter stratopause: A gravity wave driven climatological feature, *J. Atmos. Sci.*, **46**(3), 1989.

Labitzke, K., Temperature changes in the mesosphere and stratosphere connected with circulation changes in winter, *J. Atmos. Sci.*, **29**(4), 756-766, 1972.

Leblanc, T., A. Hauchecorne, M. –L. Chanin, C. Rogers, F. Taylor, and N. Livesey, Mesospheric temperature inversions as seen by ISAMS in December 2001, *Geophys. Res. Lett.*, **22**(12), 1485-1488, 1995.

Leblanc, T., I. S. McDermid, A. Hauchecorne, and P. Keckhut, Evaluation of optimization of lidar temperature analysis algorithms using simulated data, *J. Geophys. Res.*, **103**(D6), 6177-6187, 1998.

Lübken, F.-J., Thermal structure of the Arctic summer mesosphere, *J. Geophys. Res.,* **104**(D8), 9135-9149, 1999.

Lübken,, F.-J., and U. von Zahn, Thermal structure of the mesopause region at polar latitudes, *J. Geophys. Res*., **96**(D11), 20841-20857, 1991.

Manney, G. L., K. Kruger, J. L. Sabutis, S. A. Sena, and S. Pawson, The remarkable 2003-2004 winter and other recent winters in the Arctic stratosphere since the late 1990s, *J. Geophys. Res.*, **110**, D04107, doi:10.1029/2004JD005367, 2005.

Manney, G. L., W. H. Daffer, K. B. Strawbridge, K. A. Walker, C. D. Boone, P. F. Bernath, T. Kerzenmacher, M. J. Schwartz, K. Strong, R. J. Sica, K. Kruger, H. C. Pumphrey, L. Froidevaux, A. Lambert, M. L. Santee, N.J. Livesey, E. E. Remsberg, M. G. Mlynczak, and J. R. Russell III, The high Arctic in extreme winters: vortex, temperature, and MLS and ACE-FTS trace gas evolution, *Atmos. Chem. Phys.*, **8**, 505-522, 2008a.

Manney, G. L., K. Krueger, S. Pawson, K. Minschwaner, M. J. Schwartz, W. Daffer, N. J. Livesey, M. G. Mlynczak, E. Remsberg, J. M. Russell, and J. W. Waters, The evolution of the stratopause during the 2006 major warming: Satellite data and assimilated meteorological analyses, *J. Geophys. Res*., doi:10.1029/2007JD009097, in press, 2008b.

Mertens, C. J., M. G. Mlynczak, M. Lopez-Puertas, P. P. Wintersteiner, R. H. Picard, J. R. Winick, L. L. Gordley, and J. M. Russell III, Retrieval of mesospheric and lower thermospheric kinetic temperature from measurements of CO2 15 mm Earth limb emission under non-LTE conditions, *Geophys. Res. Lett*., **28**(7), 1391-1394, 2001.

Mertens, C. J., F. J. Schmidlin, R. A. Goldberg, E. E. Remsberg, W. D. Pesnell, J. M. Russell III, M. G. Mlynczak, M. Lopez-Puertas, P. P. Wintersteiner, R. H. Picard, J. R. Winick, and L. L. Gordley, SABER observations of mesospheric temperatures and comparisons with falling sphere measurements taken during the 2002 summer MaCWAVE campaign, *Geophys. Res. Lett*., **31**(3), L03105, doi:10.1029/2003GL018605, 2004.

Mizutani, K., T. Itabe, M. Yasui, T. Aoki, Y. Murayama, and R. L. Collins, Rayleigh and Rayleigh Doppler lidars for the observations of the Arctic middle atmosphere, *IEICE Trans. Fundam. Electron. Commun. Comput. Sci.,* E83-B, 2003, 2000.

Murayama, Y., M. Ishii, M. Kubota, M. Hirotaka, K. Mizutani, S. Ochiai, Y. Kasai, S. Kawamaura, Y. Tanaka, H. Masuko, T. Iguchi, H. Kumagai, T. Kikuchi, K. Sata, R. L. Collins, B. J. Watkins, M. Conde, W. B. Bristow, and R. W. Smith, Comprehensive Arctic atmosphere observing system and observed results for system performance demonstration, *J. Nat. Instit. Info. Comms. Tech*, **54**(1/2), 5-16, 2007.

Nadakuditi, S., *Spectral estimation of wave-driven fluctuations in Rayleigh lidar temperature measurements*, MS Thesis, University of Alaska Fairbanks, 2005.

Papoulis, A., and S. U. Pillai, *Probability, Random Variables, and Stochastic Processes*, 852 pp., Fourth Edition, McGraw-Hill, New York, 2002.

Pawson, S., K. Kodera, K. Hamilton, T. G. Shepherd, S. R. Beagley, B. A. Boville, J. D. Farrara, T. D. A. Fairlie, A. Kitoh, W. A. Lahoz, U. Langematz, E. Manzini, D. H. Rind, A. A. Scaife, K. Shibata, P. Simon, R. Swinbank, L. Takacs, R. J. Wilson, J. A. Al-Saadi, M. Amodei, M. Chiba, L. Coy, J. de Grandpré, R. S. Eckman, N. Fiorino, W. L. Grose, H, Koide, J. N. Koshyk, D. Li, J. Lerner, J. D. Mahlman, N. A. McFarlane, C. R. Mechoso, A. Molod, A. O'Neill, R. B. Pierce, W. J. Randel, R. B. Rood, and F. Wu., The GCM-reality intercomparison project for SPARC (GRIPS): Scientific issues and initial results, *Bull Am. Met. Soc*., **81**(4), 781-796, 2000.

Pratt, W. K., *Laser communications systems*, 271 pp., Wiley, New York, 1969.

Ramaswamy, V., M.-L. Chanin, J. Angell, J. Barnett, D. Gaffen, M. Gelman, P. Keckhut, Y. Koshelkov, K. Labitzke, J.-J. R. Lin, A. O'Neill, J. Nash, W. Randel, R. Rood, K. Shine, M. Shiotani, and R. Swinbank, Stratospheric temperature trends: Observations and model simulations, *Rev. Geophys*., **39**(1), doi:10.1029/1999RG000065, 2001.

Randel, W., P. Udelhofen, E. Fleming, M. Geller, M. Gelman, K. Hamilton, D. Karoly, D. Ortland, S. Pawson, R. Swinbank, F. Wu, M. Baldwin, M.-L. Chanin, P. Keckhut, K. Labitzke, E. Remsberg, A. Simmons, and D. Wu, The SPARC intercomparison of middle- atmosphere climatologies, *J. Climate*, **17**(5), 986-1003, 2004.

Russell, J. M. III, M. G. Mlynczak, L. L. Gordley, J. Tansock, and R. Esplin, An overview of the SABER experiment and preliminary calibration results, *Proceedings of the SPIE*, 44th Annual Meeting, Denver, Colorado, July 18-23, **3756**, 277-288, 1999.

Scaife, A. A.., J. R. Knight, G. K. Vallis, and C. K. Folland, A stratospheric influence on the winter NAO and North Atlantic surface climate, *Geophys. Res. Lett.,* **32**(18)*,* L18715, doi:10.1029/2005GL023226, 2005.

Schoeberl, M. R., L. R. Lait, P. A. Newman, and J. E. Rosenfeld, The structure of the polar vortex, *J. Geophys. Res*., **97**(D8), 7859-7882, 1992.

Senft, D. C., G. C. Papen, C. S. Gardner, J. R. Yu, D. A. Kreuger, and C. Y. She, Seasonal variations of the thermal structure of the mesopause region at Urbana, IL (40°N, 88°W) and Ft. Collins, CO (41°N, 105°W), *Geophys. Res. Lett.,* **21**(9)*,* 821-824, 1994.

Sica R. J., M. R. M. Izawa, K. A. Walker, C. Boone, S. V. Petelina, P. S. Argall, P. Bernath, G. B. Burns, V. Catoire, R. L. Collins, W. H. Daffer, C. De Clercq, Z. Y. Fan, B. J. Firanski, W. J. R. French, P. Gerard, M. Gerding, J. Granville, J. L. Innis, P. Keckhut, T. Kerzenmacher, A. R. Klekociuk, E. Kyrö, J. C. Lambert, E. J. Llewellyn, G. L. Manney, I. S. McDermid, K. Mizutani, Y. Murayama, C. Piccolo, P. Raspollini, M. Ridolfi, C. Robert, W. Steinbrecht, K. B. Strawbridge, K. Strong, R. Stübi, and B. Thurairajah, Validation of the Atmospheric Chemistry Experiment (ACE) version 2.2 temperature using ground-based and space-borne measurements, *Atmos. Chem. Phys*., **8**, 35-62, 2008.

Siskind, D. E., L. Coy, and P. Espy, Observations of stratospheric warmings and mesospheric coolings by the TIMED SABER instrument, *Geophys. Res. Lett*., 32, L09804, doi:110.1029/2005GL022399, 2005.

Siskind, D. E., S. D. Eckermann, L. Coy, J. P. McCormack, and C. E. Randall, On recent interannual variability of the Arctic winter mesosphere: Implications for tracer decent, *Geophys. Res. Lett.,* **34***,* L09806, doi:10.1029/2007GL029293, 2007.

Solomon, S., Stratospheric ozone depletion: A review of concepts and history, *Rev. Geophys*., **37**(3), doi:10.1029/1999RG900008, 1999.

SPARC, 2002: *SPARC intercomparison of middle atmosphere climatologies*, SPARC Rep. 3, 96 pp., 2002.

Wang, W., *Spectral estimation of signal and noise power in Rayleigh lidar measurements of the middle atmosphere*, MS Thesis, University of Alaska Fairbanks, 2003.

WMO: *Scientific assessment of ozone depletion: 2006*, WMO report No. 50, U. N. Environ. Program, Geneva, Switzerland, 2007.

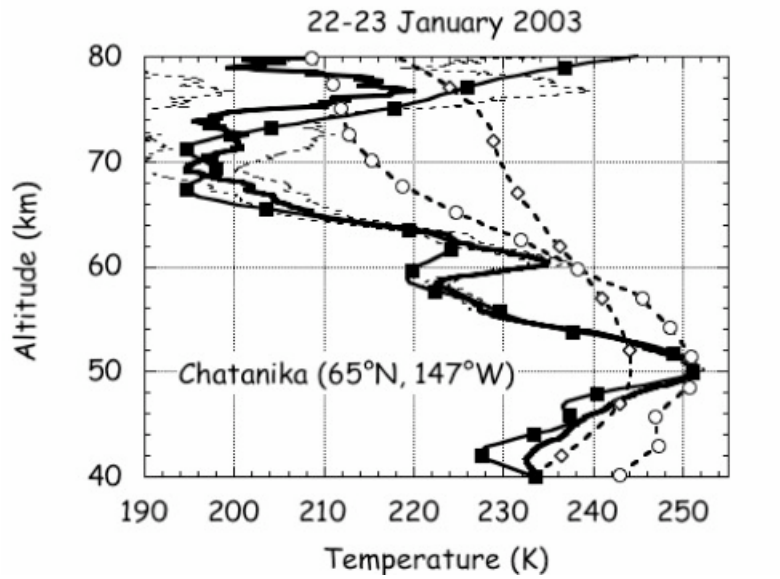

Figure 2.1. Vertical temperature profile plotted as a function of altitude measured by Rayleigh lidar at PFRR, Chatanika, Alaska (65°N, 147°W) for the period 2329-0130 LST on the night of 22-23 January 2003 LST (thick solid line). The uncertainty in the temperature profile is also plotted (thin dashed line). Temperature profile measured by SABER at 0030 LST (solid line with solid square), reported by SPARC (dashed line with open circle) and MSISE-90 (dashed line with open diamond) are also plotted.

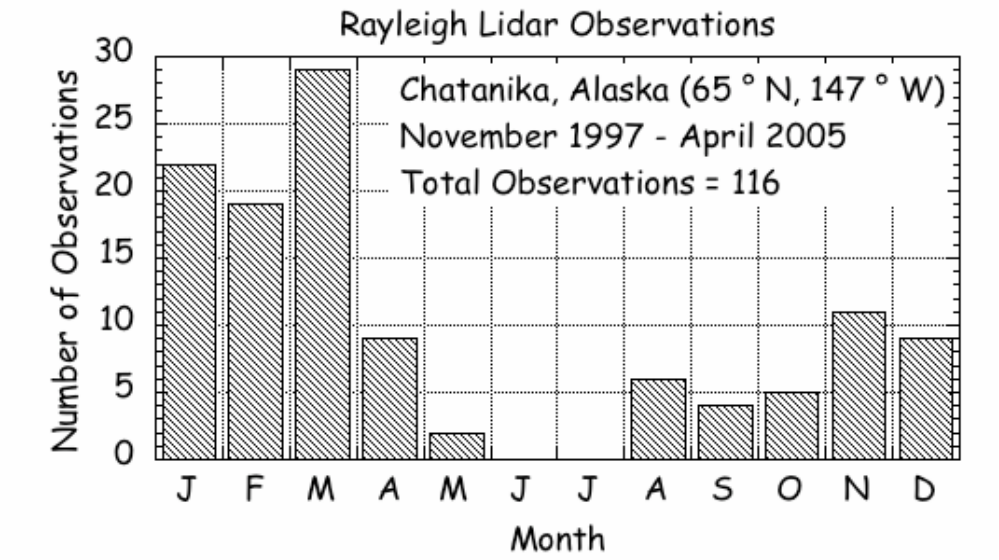

Figure 2.2. Monthly distribution of 116 Rayleigh lidar measurements of nightly middle atmosphere temperature profiles at PFRR, Chatanika, Alaska (65°N, 147°W).

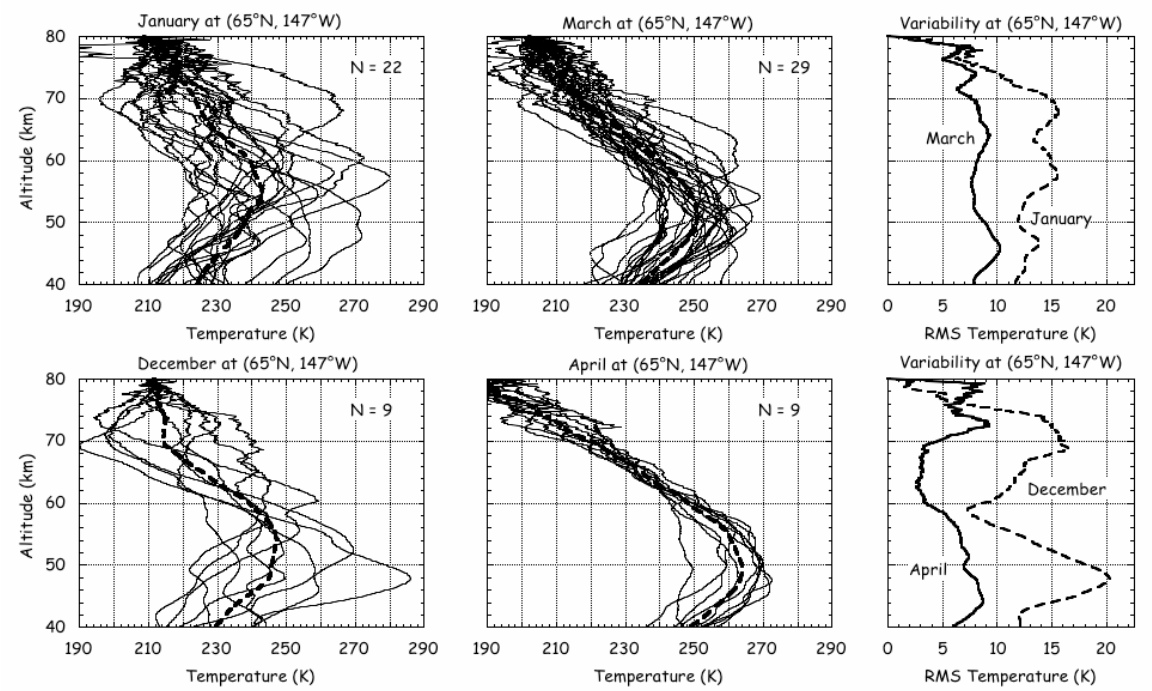

Figure 2.3. Nightly temperature profiles as a function of altitude measured in January (upper left), March (upper center), December (lower left), and April (lower center) at PFRR, Chatanika, Alaska (65°N, 147°W). The monthly average profile is also plotted (thick dashed line). The number of nightly profiles, N, is indicated on each panel. Sample standard deviation in nightly temperature profiles as a function of altitude measured in January and March (upper right), and December and April (lower right).

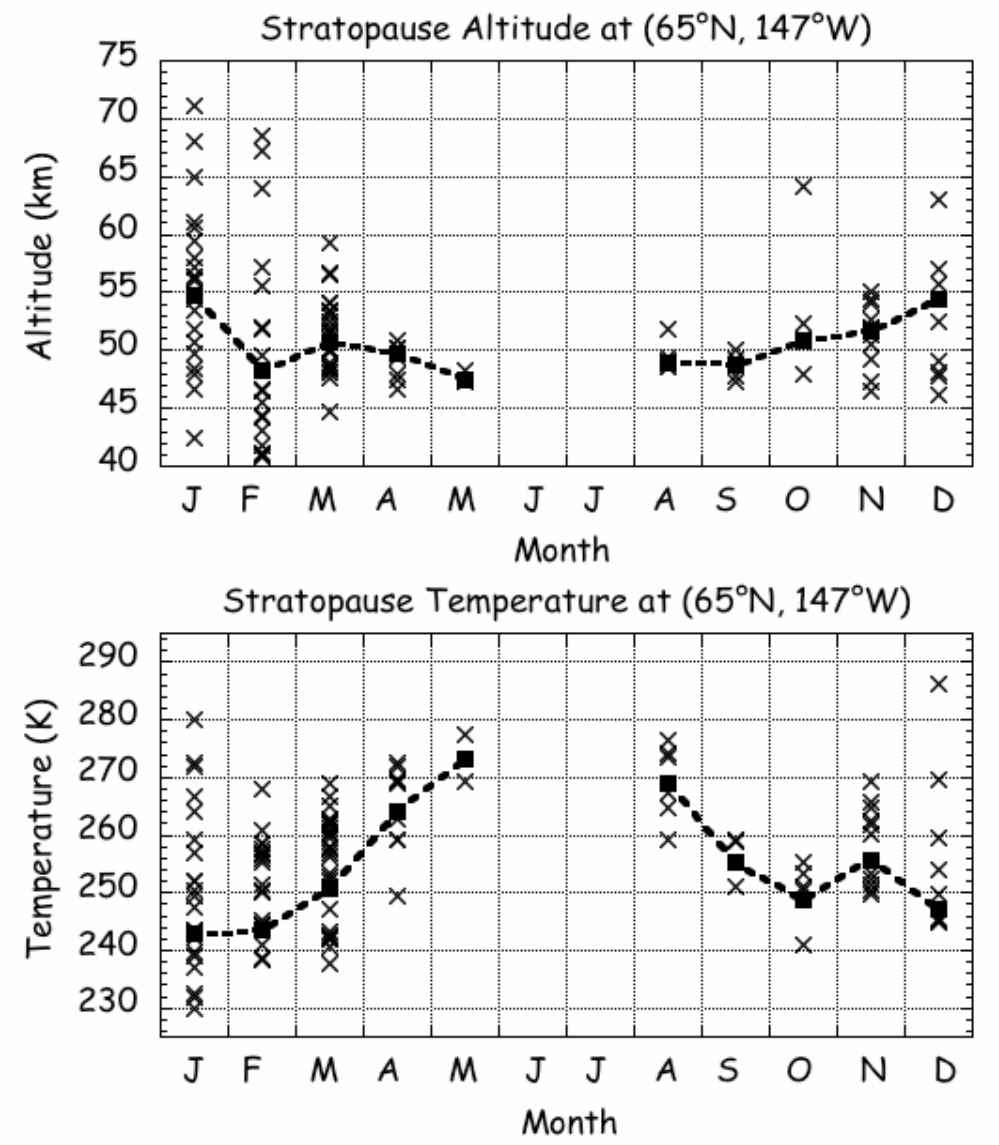

Figure 2.4. Monthly variation of the stratopause altitude and temperature at PFRR, Chatanika, Alaska (65°N, 147°W) measured by Rayleigh lidar. (Upper) Altitude of stratopause plotted as a function of month. (Lower) Temperature of stratopause plotted as a function of month. Individual nightly values (×), monthly average profile (dashed line with closed square).

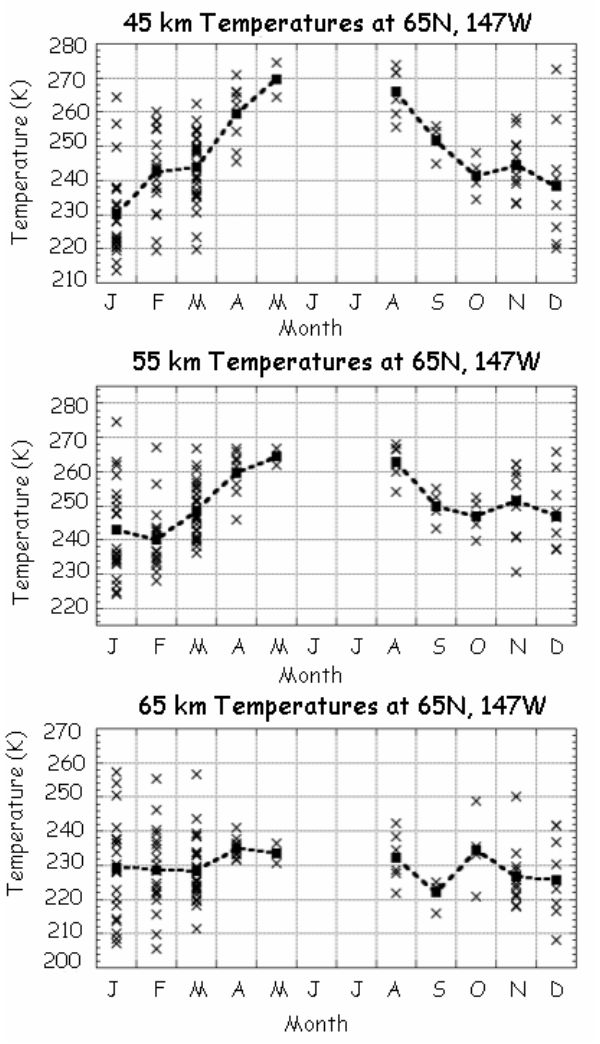

Figure 2.5. Monthly variation of stratospheric and mesospheric temperatures measured by Rayleigh lidar at PFRR, Chatanika, Alaska (65°N, 147°W). The values from individual nightly measurements (×) and monthly average profiles (dashed line with closed square) are plotted. (Upper) Temperature at 45 km plotted as a function of month. (Middle) Temperature at 55 km plotted as a function of month. (Lower) Temperature at 65 km plotted as a function of month.

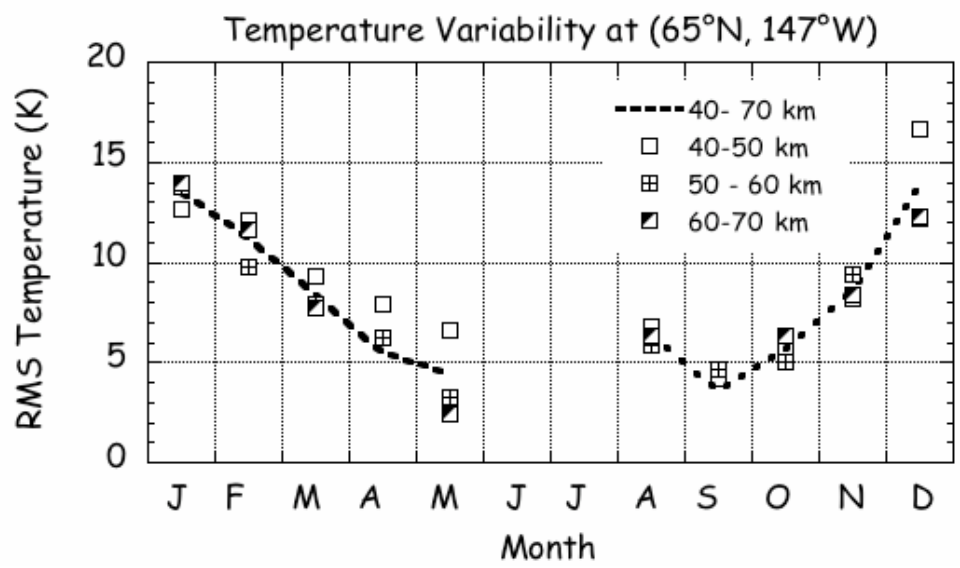

Figure 2.6. Variation in rms temperature as a function of month at PFRR, Chatanika, Alaska (65°N, 147°W). These rms temperatures are root mean-square averages of sample standard deviations over the 40-70 km, 40-50 km, 50-60 km, 60-70 km altitude regions. The rms measurement error has been subtracted.

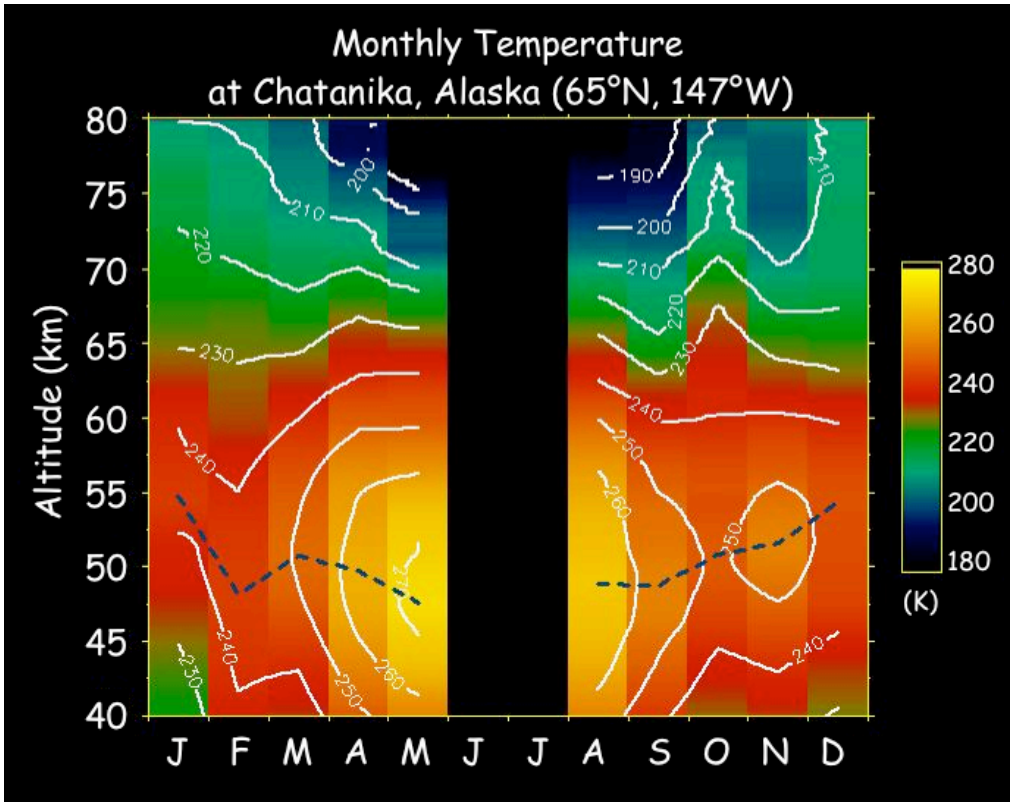

Figure 2.7. False color plot of monthly mean temperature measured by Rayleigh lidar as a function of month and altitude at PFRR, Chatanika, Alaska (65^{o}N, 147^{o}W). The stratopause altitude is plotted as a broken line. No measurements are reported for June and July

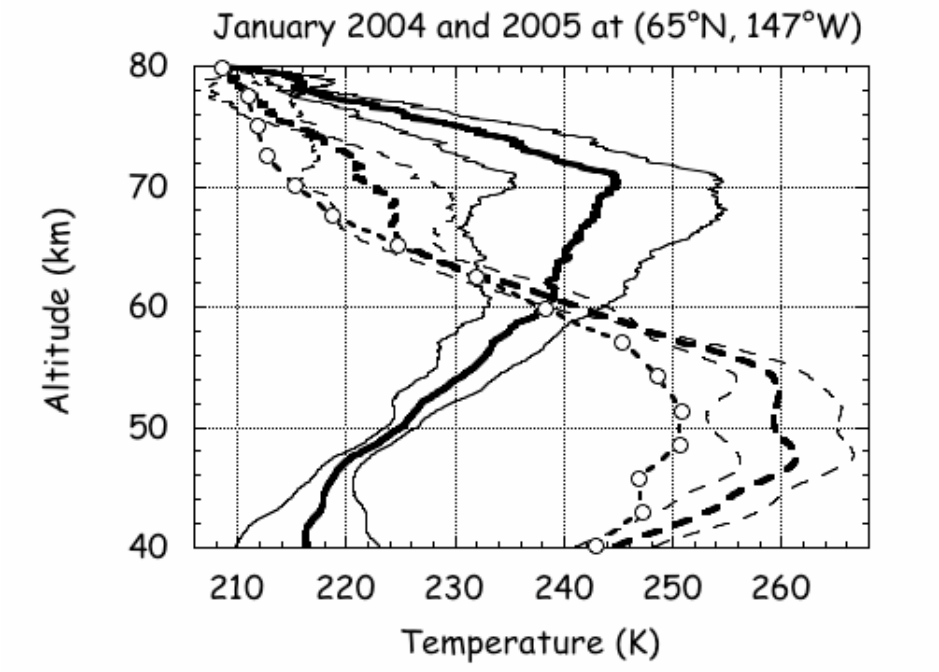

Figure 2.8. Vertical temperature profile measured by Rayleigh lidar at PFRR, Chatanika Alaska (65°N, 147°W) for January 2004 (thick solid line) and January 2005 (thick dashed line). The January 2004 profile represents the average of the three observations on the nights of 5-6, 15-16, and 29-30 January. The January 2005 profile represents the average of the three observations on the nights of 10-11, 18-19, and 27-28 January. The mean temperature plus and minus the sample uncertainty is also plotted (thin solid and thin dashed lines). The SPARC reference atlas profile for January is plotted for comparison (dashed line with open circle).

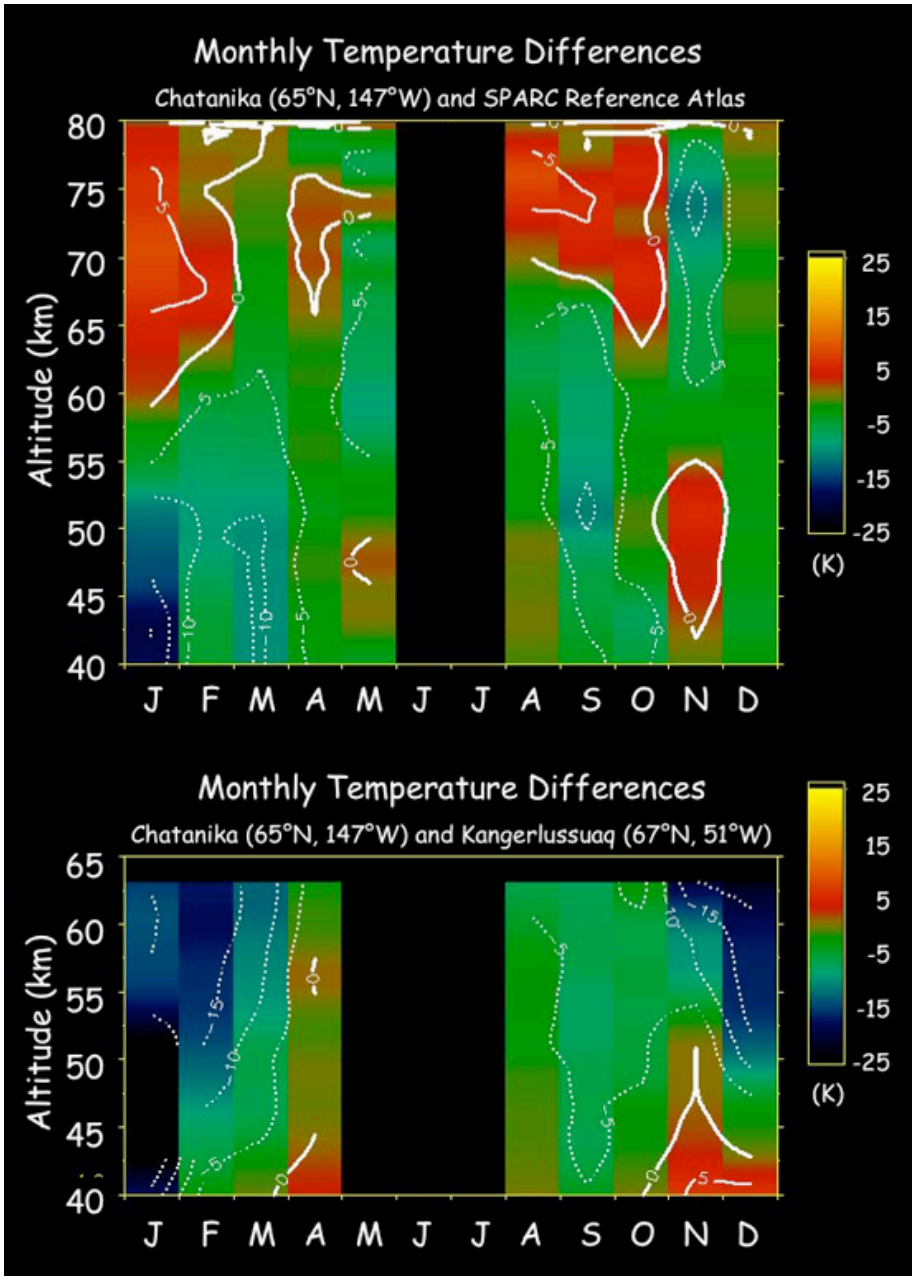

Figure 2.9. Monthly temperature differences between the Rayleigh lidar measurements at PFRR, Chatanika, Alaska (65^{o}N, 147^{o}W) and (upper) the SPARC reference atlas, and (lower) Rayleigh lidar measurements at Kangerlussuaq, Greenland (67^{o}N, 51^{o}W). These difference temperatures are calculated by subtracting the temperatures of the SPARC reference atlas and the measurements at Kangerlussuaq from the temperature measurements at Chatanika.

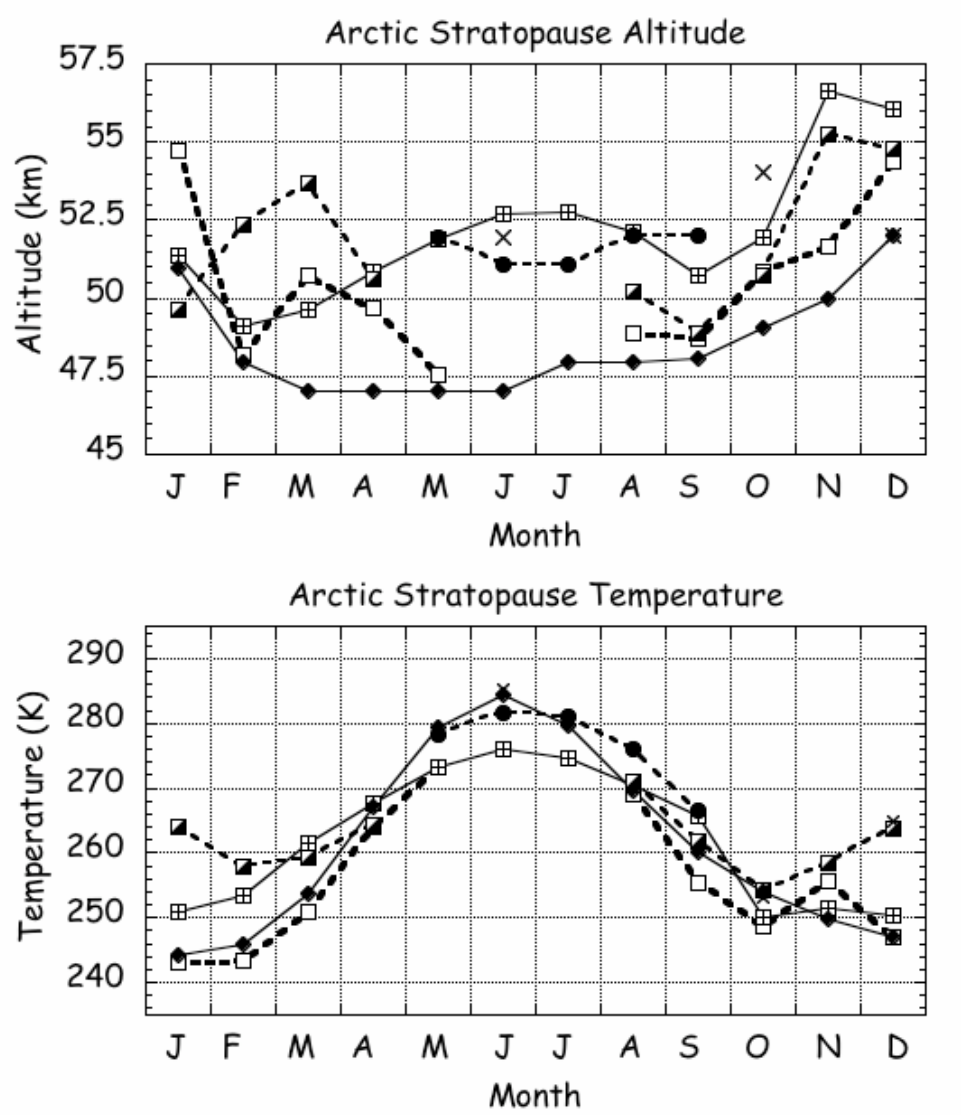

Figure 2.10. Monthly variation of the stratopause in the Arctic. (Upper) Altitude of stratopause plotted as a function of month. (Lower) Temperature of stratopause plotted as a function of month. Rayleigh lidar measurements at Chatanika (dashed line with open square), SPARC Reference atlas (SPARC, 2002) (solid line with cross square), Gerrard *et al*., (2000) (dashed line with half open square), Lübken (1999) (dashed line with solid circle), Lübken and von Zahn (1991) (×), MSISE-90 (Hedin, 1991) (solid line with closed diamond).

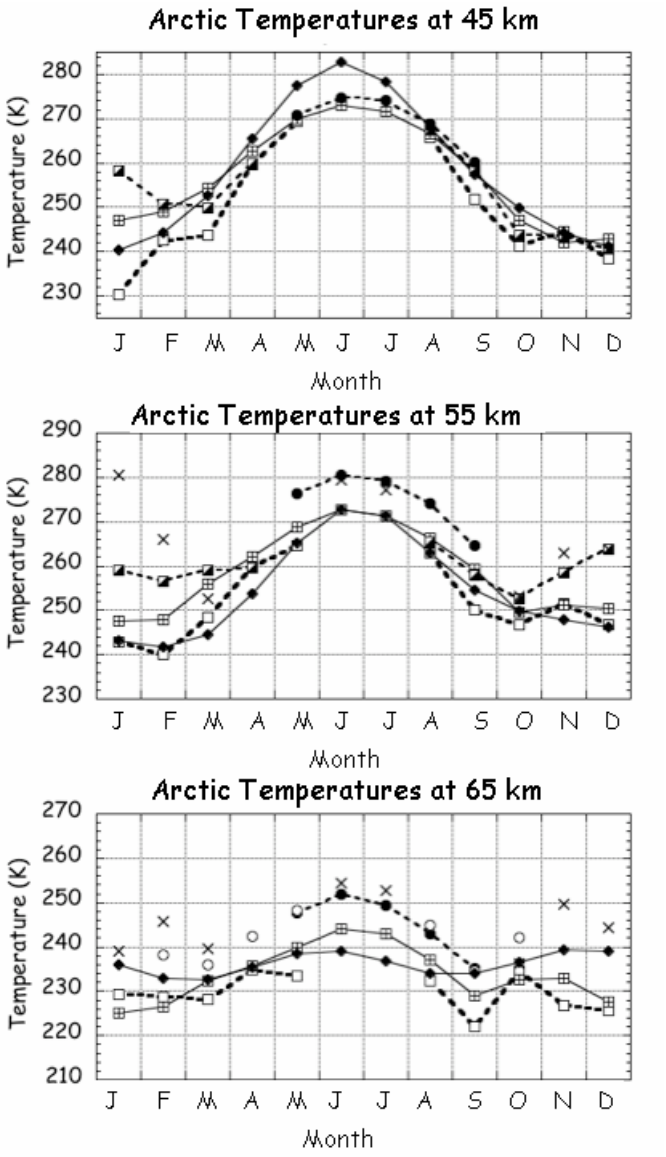

Figure 2.11. Monthly variation of thermal structure of stratosphere and mesosphere in the Arctic. (Upper) Temperature at 45 km plottted as a function of month. (Middle) Temperature at 55 km plotted as a function of month. (Lower) Temperature at 65 km plotted as a function of month. See Fig. 10 for details. The 65 km plot includes data from Clancy et al., (1994) (open circle) in addition to the other data sets.

Chapter 3. Rayleigh Lidar Observations of Reduced Gravity Wave Activity during the Formation of an Elevated Stratopause in 2004 at Chatanika, Alaska (65°N, 147°W)[1]

Abstract. We report Rayleigh lidar measurements of the stratosphere and mesosphere at Poker Flat Research Range, Chatanika, Alaska (65°N, 147°W) in December, January and February over three winters (2002-2003, 2003-2004, 2004-2005). The Rayleigh lidar measurements have yielded nightly temperature profiles in the 40-80 km altitude region and 15 min relative density profiles in the 40-50 km altitude region. We characterize the gravity wave activity in terms of the buoyancy period, relative density fluctuations, vertical displacement fluctuations, and potential energy density. These three winters have marked different meteorological conditions with a major stratospheric warming in 2002-2003, an extreme warming event in 2003-2004 resulting in an elevated stratopause, and no warming in 2004-2005. Over all three winters the average potential energy density of 2.6 J/kg is significantly lower than that reported at mid-latitudes. This reduction of gravity wave activity is most pronounced in 2003-2004 (1.1 J/kg) during the appearance of an elevated stratopause at 70.3 km in January. The largest average wave energies (5.7 J/kg) occur in 2004-2005. The growth length of the gravity wave potential energy density is largest in 2003-2004 (52 km). We use satellite and reanalysis data to analyze the gravity wave activity in terms of the synoptic structure of the vortex and the Aleutian anticyclone and the planetary wave activity. We find a significant positive correlation of 0.74 between the wave activity and the wind speeds in the lower stratosphere. These observations confirm recent modeling studies that suggest that the elevated stratopause is formed by blocking the transmission of gravity waves into the mesosphere.

---

[1]Thurairajah, B., R. L. Collins, V. L. Harvey, R. S. Lieberman, K. Mizutani (2009), Rayleigh lidar observations of reduced gravity wave activity during the formation of an elevated stratopause in 2004 at Chatanika, Alaska (65°N, 147°W), submitted to *J. Geophys. Res*. in August 2009.

3.1. Introduction

The general circulation of the middle atmosphere includes two wave-driven circulation patterns; the planetary wave driven equator-to-pole circulation (often referred to as Brewer-Dobson circulation after *Brewer* [1949] and *Dobson* [1956]) in the lower stratosphere and the gravity wave driven pole-to-pole circulation in the mesosphere [*Houghton*, 1978]. These circulations have a variety of impacts on the atmosphere, including the transport of critical species (e.g. ozone, water vapor) in the middle atmosphere, the lifetime of minor species (e.g., chloroflourocarbons) in the stratosphere, the cooling of the polar summer mesopause region, and the warming of the polar winter stratopause region (see reviews by *Holton et al.*, 1995; *Solomon,* 1999; *Holton and Alexander*, 2000; *Fritts and Alexander*, 2003 and references therein). Changes in the Arctic wintertime circulation with warming of the stratosphere, cooling of the mesosphere, and breakdown of the polar vortex have been documented and understood in terms of planetary wave activity since the 1970s [*Matsuno*, 1971; *Labitzke*, 1972]. The breakdown of the polar vortex during these stratospheric warming events inhibits the formation of polar stratospheric clouds and the subsequent depletion of ozone (see review by *Schoeberl and Hartmann*, 1991). Stratospheric warmings have attracted attention in recent years due to an increase in frequency and strength, with significant disruptions of the circulation in the winters of 2003-2004 and 2005-2006 and little disruption in 2004-2005 [*Manney et al*., 2005; 2006; 2008]. *Rex et al*. [2006] have documented the extensive ozone loss in the Arctic middle atmosphere during the winters of 2004-2005 when the Artic vortex was not disturbed.

Recent studies of transport of NO_x from the upper mesosphere / lower thermosphere to the stratosphere and the subsequent interaction of NO_x with stratospheric ozone have raised questions about the relative role of planetary and gravity waves in the polar circulation [*Randall et al*., 2006]. *Hauchecorne et al*. [2007] and *Siskind et al*. [2007] have studied the downward transport of NO_x in the wintertime Arctic middle atmosphere associated with sudden stratospheric warmings in 2004 and 2006, respectively. During these winters the disruption of the circulation results in a cooling of the upper

stratosphere and warming of the mesosphere and the formation of an elevated stratopause. *Hauchecorne et al*. [2007] used satellite observations in January-February 2004 to study a large increase of NO_2 in the Arctic polar mesosphere with simultaneous depletion of O_3. *Hauchecorne et al*. [2007] attribute this enhancement of NO_x to the blocking of planetary waves, which allowed the propagation and breaking of gravity waves and tidal waves in the middle and upper mesosphere and enhanced the descent of NO_x into the polar vortex. *Siskind et al*. [2007] use satellite observations and a general circulation model to study tracer descent in February 2006 and address the observations of *Randall et al.* [2006]. *Siskind et al*. [2007] conclude that the elevated stratopause is coupled to a disturbed stratosphere owing to the occurrence of stratospheric warming that suppresses vertical propagation of orographic gravity waves. Subsequent vertical propagation and breaking of a planetary wave one in the mesosphere facilitated the downward decent of NO_x. Both *Hauchecorne et al.* [2007] and *Siskind et al.* [2007] emphasize the coupled role of planetary and gravity waves in the variability of the Arctic wintertime stratosphere and mesosphere, but present opposing views of the dynamical interaction. While both studies identify gravity waves as a key physical process in these events, neither study presents direct observations of the gravity wave activity.

Several studies have focused on the influence of the synoptic-scale features on the upward propagation of gravity waves in the Arctic middle atmosphere. Lidar studies of the Arctic middle atmosphere by *Gerrard et al*. [2002] have shown that the synoptic scale movement of the stratospheric vortex influences the stratospheric and lower mesospheric temperatures over three sites in Kangerlussuaq, Greenland (67^oN, 51^oW), Eureka, Canada (80^oN, 86^oW), and Andoya, Norway (69^oN, 16^oE), all located in the eastern Arctic where the vortex is present and the Aleutian anticyclone is absent. Lidar studies of gravity wave activity over Eureka, Canada [*Whiteway and Carswell*, 1994; *Duck et al.*, 1998; *Duck et al*., 2001] have also shown a reduction of gravity wave activity in the upper stratosphere associated with movement of the stratospheric vortex overhead. However, these lidar studies were conducted during winters when there were no major stratospheric warmings (i.e., 1992-1993 through 1997-1998).

In this paper we present Rayleigh lidar measurements of gravity wave activity in the upper stratosphere and lower mesosphere during the winters of 2002-2003, 2003-2004, and 2004-2005 over Poker Flat Research Range (PFRR), Chatanika, Alaska (65^{o} N, 147^{o} W). The location of Chatanika provides an opportunity to study gravity wave variability under the influence of both the Aleutian anticyclone and the stratospheric vortex using direct measurements. *Dunkerton and Butchart* [1984] have shown by ray tracing studies that gravity wave propagation is modulated by the stratospheric vortex and Aleutian anticyclone with the lighter winds in the anticyclone blocking the upward transmission of orographic gravity waves. This paper is arranged as follows. In section 3.2 we describe the Rayleigh lidar technique and the methods used to determine and characterize the gravity wave activity. In section 3.3 we present lidar measurements of the temperature profiles and the gravity waves in December, January and February (DJF) of 2002-2003, 2003-2004, 2004-2005. In section 3.4 we present the planetary wave activity and synoptic structure of the Arctic middle atmosphere during these winters using satellite measurements and meteorological global analyses data. We discuss the evolution of the circulation of the whole Arctic region as well as over Chatanika. In section 3.5 we analyze the observed gravity wave activity in terms of the synoptic structure and horizontal winds. In section 3.6 we present our summary and conclusions.

3.2. Rayleigh Lidar Technique

The National Institute of Information and Communications Technology (NICT) Rayleigh lidar has been operated at PFRR, Chatanika, Alaska since 1997 [*Mizutani et al*., 2000; *Thurairajah et al*., 2009]. The NICT Rayleigh lidar is a zenith pointing system, and consists of a Nd:YAG laser, a 0.6 m receiving telescope, and a photomultiplier based photon-counting receiver system. The laser operates at 532 nm with a pulse repetition rate of 20 pps. The laser pulse width is 7 ns FWHM, and the average laser power is 9 W. The photon counts are integrated over 0.5 μs yielding a 75 m range sampling resolution. The raw photon count profiles are acquired every 50 s representing the integrated echo from 1000 laser pulses. The photon counting process is statistical in nature and thus the

recorded profiles include both fluctuations due to geophysical variations as well as statistical fluctuations. These statistical fluctuations are an inherent noise in the measurement. The raw photon profiles are then integrated in time to yield 15 min profiles for analysis of wave driven density fluctuations and over the whole observation period to yield a nightly temperature profile. In this study we use 29 nights of lidar measurements from DJF of 2002-2003, 2003-2004, and 2004-2005. These measurements last between four and 14 hours for a total of 255 hours of observations.

The lidar observations yield measurements of the stratospheric and mesospheric temperature profile (~40-80 km) under the assumptions of hydrostatic equilibrium using an initial temperature at the upper altitude of 80 km [e.g., *Thurairajah et al*., 2009]. We characterize the gravity wave activity in the upper stratosphere and lower mesosphere in terms of the atmospheric stability, T_B, rms density fluctuation, ρ'/ρ_o, vertical displacement, ξ, and potential energy density, E_p, calculated from the 15 minute resolution Rayleigh lidar data. To estimate the gravity activity we first calculate the logarithm of the nightly average density profile. A 3rd order polynomial is fitted to this profile, which is then subtracted from the logarithmic average density profile. The residual is filtered by a low pass filter of wavelength 6 km to remove photon noise and then added back to the 3rd order fitted density profile. The antilog of the resulting density profile forms the background density, $\rho_o(z)$. The background density is subtracted from the 15 min density profiles (obtained by binning the raw photon count profiles acquired every 50s) to form the perturbation density, $\rho'(z,t)$. The perturbation is then normalized by dividing it by the back ground density profile to obtain the relative density perturbation $\rho'(z,t)/\rho_o(z)$. To reduce the statistical noise in the measurement and characterize short period waves the perturbations are spatially band-limited between vertical wavenumbers 0.5 km^{-1} and the required vertical altitude range and temporally band-limited by the Nyquist frequency of 2 h^{-1} and the low frequency 0.25 h^{-1}. We determine the mean-square noise fluctuation from the average vertical wavenumber spectrum of the perturbations and subtract it from the total mean-square fluctuations to

yield an estimate of the mean-square relative density fluctuations ($\overline{(\rho'(z,t)/\rho_o(z))^2}$) [*Wang,* 2003]. The mean-square vertical displacement ($\overline{\xi^2}$) is derived from the mean-square relative density fluctuation using the gravity wave polarization relations [e.g., *Gill*, 1982],

$$\overline{\xi^2} = \frac{g^2}{N^4}\overline{\left(\frac{\rho'}{\rho_o}\right)^2} \tag{3.1}$$

where g is the acceleration due to gravity, and *N* is the buoyancy frequency defined as,

$$N^2 = \frac{g}{T_o}\left(\frac{\partial T_o}{\partial z} + \frac{g}{C_p}\right) \tag{3.2}$$

where T_0 is the vertical temperature profile, and Cp is the specific heat at constant pressure. The potential energy density (E_p) is given by [e.g. *Gill*, 1982],

$$E_p = \frac{1}{2}N^2\overline{\xi^2} = \frac{1}{2}\left(\frac{g}{N}\right)^2\overline{\left(\frac{\rho'}{\rho_o}\right)^2} \tag{3.3}$$

We plot two examples of the relative density perturbations measured with the lidar as contour plots in altitude and time in Figure 3.1. In the upper panel we show relative density perturbations derived from lidar measurements taken over a ~11 h period (2014-0649 LST (LST = UT – 9 h)) on the night of 15-16 January 2004. In the lower panel we show relative density perturbations derived from lidar measurements taken over a ~14 h period (1820 – 0820 LST) on the night of 10-11 January 2005. The relative density perturbations show periodic variations with downward phase progression typical of upwardly propagating gravity waves reported in other lidar studies [e.g., *Wilson et al.*, 1991]. We present the buoyancy period and wave parameters for these observations in Table 3.1. The values of the potential energy density (1.6 J/kg on 15-16 January 2004 and 13.3 J/kg on 10-11 January 2005) can be compared with the Rayleigh lidar measurements of potential energy density in the 30-45 km and 45-60 km altitude ranges at the mid-latitude sites of Observatoire de Haute Provence (OHP, 44^{o}N, 6^{o}E) and the Centre d'Essais des Landes at Biscarosse (BIS, 44^{o}N, 1^{o}W) in France [*Wilson et al*., 1991]. We first take the geometric mean of the measurements at 30-45 and 45-60 km to yield an

equivalent measurement at 45 km and then scale these values by a factor of 1.7 to compensate for differences in data processing between the data sets. The compensated monthly mean for January at OHP and BIS are 10 J/kg and 7 J/kg respectively. The two measurements at Chatanika span the monthly average values at the mid-latitude sites, though the value of the 2004 measurement is significantly lower than the monthly average values measured at mid-latitudes.

3.3. Rayleigh Lidar Measurements

3.3.1. Temperature Profile

We plot the individual and monthly mean profiles of 14 nighttime measurements for January 2003, 2004, and 2005 in Figure 3.2 (left panel). These measurements have yielded a total of 122 hours of data. We average the nighttime profiles for each month to form the monthly mean profile. We also compare (Figure 3.2, right panel) the monthly mean profile for January 2003, 2004, and 2005 to the monthly mean January profile calculated from 22 nights of lidar measurements over Chatanika from 1998 to 2005 [*Thurairajah et al*., 2009] and the zonal mean temperature climatology from the Stratospheric Processes And their Role in Climate (SPARC) reference atlas [*Randel et al*., 2004; SPARC, 2002]. The Rayleigh lidar measurements at Chatanika show a high degree of interannual variability in the monthly mean temperature profile over these three years. In January 2003 the upper stratosphere and mesosphere were colder than the Chatanika and SPARC averages with the stratopause located at 54.0 km with a temperature of 237.3 K. In January 2004 the upper stratosphere was much colder and the mesosphere much warmer than the Chatanika and SPARC averages with the stratopause vertically displaced to 70.3 km with a temperature of 245.0 K. In January 2005 the upper stratosphere was much warmer than the Chatanika and SPARC averages with the stratopause located at 47.5 km with temperature of 261.4 K.

In Figure 3.3 we plot the buoyancy period averaged over the 40-50 km altitude range as a function of day during DJF of 2002-2003, 2003-2004, and 2004-2005. On average the buoyancy period is lower in the winter of 2003-2004 than in 2002-2003 and

2004-2005 (Table 3.2). In 2003-2004 the background atmosphere is less stable with higher buoyancy period during the first half of 2003-2004 winter (average: 320 s (± 5 s)), and more stable with lower buoyancy period after 15 January 2004 (average: 273 s ((± 4 s)). The increase in stability in 2003-2004 coincides with the formation of the elevated stratopause. In 2002-2003 and 2004-2005 the stability generally decreases through the winter.

3.3.2. Gravity Wave Activity

In Figure 3.4 we plot the gravity wave activity in terms of rms relative density fluctuation, rms vertical displacement fluctuation, and potential energy density averaged over 40-50 km as a function of day during DJF of the three winters. We tabulate the average values for DJF in Table 3.2. The gravity wave fluctuations have significantly lower rms relative density and vertical displacement in 2003-2004 compared to the other two winters. The rms relative density and vertical displacement fluctuations are largest in 2004-2005 having values that are twice the 2003-2004 values. The interannual differences are more pronounced in the rms displacements than the rms relative density fluctuations due to the inter-annual differences in the atmospheric stability (Eqn. 2). The average potential energy density in 2004-2005 of 5.7 J/kg is 5.2 times larger than in 2003-2004 and 2.7 times larger than in 2002-2003. The values measured at Chatanika are consistently lower than the compensated DJF monthly mean values from OHP and BIS (i.e., 7-11 J/kg) [*Wilson et al*., 1991]. It is only during the winter of 2004-2005 that values of the potential energy density measured at Chatanika have values similar to the DJF monthly mean values measured at OHP and BIS.

In Figure 3.5 we plot the rms relative density fluctuation as a function of buoyancy period averaged over 40-50 km for all three winters. We calculate linear fits to the data for the entire data set as well as by year. The correlation coefficient for all 29 nights is 0.21, with a value of 0.24 for the 2002-2003 data (15 nights), 0.17 for the 2003-2004 data (8 nights), and 0.69 for the 2004-2005 data (6 nights). There is no significant variation of rms relative density fluctuation with buoyancy period except in 2004-2005, where the

rms amplitude of the gravity-wave fluctuations decreases as buoyancy period increases (i.e., the stability decreases). Examination of the variation of rms vertical displacement and potential energy per unit mass with buoyancy period shows similar behavior albeit with lower correlation coefficients. This behavior suggests that the amplitude of the gravity-wave fluctuations does not increase as the stability decreases and we conclude that the measured fluctuations represent gravity waves that are propagating through the 40-50 km altitude region rather than being generated by the local atmospheric stability conditions. The decrease of the rms amplitude of the gravity wave fluctuations with increase in buoyancy period in 2004-2005, when the gravity wave amplitudes are largest, is consistent with saturation of the gravity wave amplitudes due to convective and dynamic instabilities [*Fritts and Rastogi,* 1985]. The limiting wave amplitudes are inversely proportional to the buoyancy period and thus decrease as the buoyancy period increases [*Smith et al*., 1987].

To better understand how the waves are propagating with altitude we calculate the vertical growth length, or scale height, of the potential energy. We calculate the growth length from the ratio of the potential energy densities over the 45-50 km to the 40-45 km altitude regions. In 2002-2003 the average ratio of the nightly energy densities at both altitudes is 2.0, corresponding to a growth length of 7.4 km. In 2003-2004 the average ratio is 1.1, corresponding to a growth length of 52 km. In 2004-2005 the ratio is 1.7 indicating a growth length of 9.4 km. We expect freely propagating waves to have a growth length in their energy equal to the density scale height of 7.0 km. Thus the gravity waves in 2002-2003 appear to be propagating freely, while the waves in 2003-2004 and 2004-2005 appear to be loosing energy. The waves in 2003-2004 appear to be loosing significant energy with altitude.

In summary the Rayleigh lidar observations at Chatanika show that the middle atmosphere during winter 2003-2004 is significantly different from the winters of 2002-2003 and 2004-2005. The temperature profile shows an elevated stratopause during January 2004 that is not observed in 2003 and 2005. The upper stratosphere (40-50 km) is more stable in January and February 2004 relative to 2003 and 2005, with shorter

buoyancy periods. The gravity wave activity is reduced in 2004 relative to the other winters with lower rms relative density fluctuations, lower rms vertical displacements, and lower potential energy densities. The gravity wave activity in 2003-2004 shows less growth with altitude suggesting stronger dissipation of the waves than in the two other winters.

3.4. Arctic Planetary Wave Activity and Synoptic Structure

In this section we analyze the synoptic structure and the planetary wave activity in the Arctic stratosphere and mesosphere during the three winters. In a recent study *Charlton and Polvani* [2007] analyze the synoptic structure and planetary wave activity to differentiate between stratospheric warming events that result in displacement of the polar vortex and those that result in splitting of the vortex in two pieces. The two types of events are dynamically different. Vortex splitting events occur after a clear preconditioning of the polar vortex and their influence on middle-stratospheric temperatures lasts for up to 20 days longer than vortex displacement events. Our goal is to understand how variations in the synoptic structure in the different winters impacts the gravity wave activity in each winter.

To characterize the synoptic structure of the middle atmosphere, we analyze the 3-D structure and temporal evolution of the stratospheric vortex and anticyclones calculated using the United Kingdom Meteorological Office (MetO) global analyses data. *Harvey et al*. [2002] presented a methodology to identify vortices in terms of evolving 3-D air masses. The calculations are done on 22 potential temperature surfaces from 240 K to 2000 K. The vortex edges are identified by integrating a scalar measure of the relative contribution of strain and rotation in the wind field around the scale stream function that characterizes the large-scale flow. The analysis of *Harvey et al.* [2002] provides a full view of the 3-D structure of the vortex and anticyclones from which we can follow the evolution of the vortex and anticyclones through the winter. We can identify vortex anticyclone interactions, vortex displacement events, and vortex splitting events. We can also determine the synoptic conditions over Chatanika (i.e., below the vortex, below the

Aleutian anticyclone, or neither). We also calculate the winds speeds from MetO analyses data and define the wind speed as the magnitude of the horizontal wind, by combining the zonal, u and meridional, v wind ($\sqrt{u^2 + v^2}$).

We characterize the planetary wave activity using geopotential heights measured by the Sounding of the Atmosphere using Broadband Emission Radiometry (SABER) instrument data (Level 2A version 1.07) [*Beaumont*, 2008] aboard the Thermosphere Ionosphere Mesosphere Energetics Dynamics (TIMED) satellite [*Mertens et al*., 2004; *Russell et al*., 1999]. Due to the satellite's two-month yaw cycle, wintertime measurements are available for a two month period from mid-January through mid-March. We use standard Fourier techniques to determine the wave-one and wave-two components in the geopotential along latitude circles for a given day of satellite observations. We characterize the amplitude of the planetary wave as the magnitude of the corresponding Fourier component of the geopotential. While the Fourier analysis yields the amplitudes of the planetary wave activity it does not yield a measure of the planetary wave breaking or whether the planetary waves disrupt the vortex and cause mixing of mid-latitude and polar air. *Harvey et al.* [2002] showed that during planetary wave breaking events the vortex and anticyclone become tilted in altitude, intertwine, and mix. If the stratospheric vortex is displaced from the pole there will be a large Fourier wave-one component indicating a large amplitude wave-one planetary wave but the vortex may remain intact. Similarly a wave that breaks and disrupts the vortex in two would contribute to a large wave-two component indicating a large amplitude wave-two planetary wave [*Shepherd*, 2000]. We also determine the gradient winds from the SABER data, and hence calculate the Eliassen-Palm flux divergence using standard techniques [*Andrews et al*., 1987].

3.4.1. Pan Arctic Perspective

The 2002-2003 winter was characterized by a cold early winter and warm mid- to late winter [*Singleton et al*., 2005]. By mid-December a robust vortex had formed (Figure 3.6 upper left panel). The lack of planetary wave activity in mid-December is evidenced

by the barotropic structure of the vortex where the vortex does not tilt with height. A minor warming occurred in late December 2002 in the upper stratosphere while the lower stratospheric temperatures remained undisturbed [*Manney et al*., 2005]. During the first half of January 2003 the Aleutian anticyclone intensified, moved eastward, and by 13 January had developed a westward tilt with height (not shown). At the same time the anticyclone elongated and displaced the vortex off the pole. By January 18 a major stratospheric warming was in progress and the anticyclone had split the vortex in the lower and the middle stratosphere (Figure 3.6 upper center panel, Figure 3.7 upper panel). The anticyclonic winds found in the Aleutian anticyclone are stronger than the cyclonic winds in the vortex during this splitting event. During this period the planetary wave-one geopotential amplitude increased to 1800 m at altitudes of 7.1 scaled heights (~50 km) (Figure 3.8 upper panel) and the wave-two amplitude increased to 1000 m at altitudes of 5.0 scaled heights (~35 km) (not shown). During the minor warming in mid-February, when the upper stratospheric vortex had again strengthened and entwined the Aleutian anticyclone and the mid- and lower stratospheric vortices were distorted (Figure 3.6 upper right panel), there is an increase of planetary wave-one (1700 m at 7.9 scaled heights (~55 km)) and wave-two amplitudes (700 m at 4.3 scaled heights (~30 km)). During both warming events in January and February the Eliassen-Palm flux divergence at 65°N decreased and had negative values.

The 2003-2004 winter was characterized by one of the most prolonged mid-winter warming event on record [*Manney et al*., 2005]. The stratospheric vortex and Aleutian anticyclone remained quasi-stationary in December (Figure 3.6 middle left panel). A major warming with strong disruption of the vortex occurred in early January 2004 when the upper stratospheric vortex had entwined around the Aleutian anticyclone while the mid- and lower stratospheric vortices were distorted and had small areas (Figure 3.6 middle center panel, Figure 3.7 middle panel). The winds in the anticyclone are much weaker and the winds in the vortex stronger than during the 2003 vortex splitting event. By mid-January the upper stratospheric vortex had reformed into a stronger cyclone while the lower and middle atmospheric vortices remained small and disrupted through

late February 2004 (Figure 3.6 middle right panel). This disruption of the polar vortex is accompanied by repeated periods of strong planetary wave-one (Figure 3.8 middle panel) and wave-two (not shown) amplitudes in January, February and early March. There are five periods of large wave-one amplitudes in late January, mid-February, and late February with peak geopotential amplitudes between 1700 m and 2800 m at altitudes between 8.3 scaled heights (~58 km) and 9.4 scaled heights (~66 km). There are repeated periods of large wave-two amplitudes in mid- and late January, mid- and late February with peak geopotential amplitudes between 700 m and 1000 m at altitudes of between 7.7 scaled heights (~54 km) and 10.9 scaled heights (~76 km). The Eliassen-Palm flux divergence at 65°N is negative between scaled heights of 5 and 9 (~35 and ~63 km) throughout the period from mid-January through early March.

The 2004-2005 winter was the coldest winter in the lower stratosphere on record at that time and no warming events satisfied the zonal mean definition during this winter of reversed meridional temperature gradients and/or easterly flow at midlatitudes [*Manney et al*., 2006]. During December 2004 the vortex in the upper stratosphere remained warm and strengthened while in the lower and mid- stratosphere the vortex was cold. The vortex remains robust and well established throughout the winter (Figure 3.6 lower panels). The area of the vortex is larger, the Aleutian anticyclone is displaced further equatorward, and the vortex winds are stronger and more uniform than in the previous two winters (Figure 3.7 lower panel). There are four periods of large wave-one amplitudes in February with peak geopotential amplitudes between 1800 m and 2100 m at altitudes between 5.8 scaled heights (~41 km) and 7.0 scaled heights (~49 km) (Figure 3.8 lower panel). There are several periods of large wave-two amplitudes in mid-January and February with peak geopotential amplitudes between 500 m and 1600 m at altitudes between 5.8 scaled heights (~41 km) and 10.0 scaled heights (~70 km) (not shown). Despite these repeated periods of large amplitude planetary wave-one in February and wave-two in mid-January and February, where the upper stratospheric vortex had entwined with the Aleutian anticyclone, the vortex remained robust and well established in the mid- and lower stratosphere (Figure 3.6 lower panels). The Eliassen-Palm flux

divergence at 65°N is negative in only two periods in late January and from the middle to end of February between scaled heights of 5 and 9 (~35 and ~63 km).

In summary the structure of the vortex and the planetary wave activity is significantly different in the three years. In 2002-2003 large amplitude planetary waves are found repeatedly throughout the winter, and are associated with interaction between the stratospheric vortex and the Aleutian anticyclone and the stratospheric warmings. In 2003-2004 large amplitude planetary waves are found more commonly throughout the winter, with ongoing interaction between the stratospheric vortex and the Aleutian anticyclone, major stratospheric warming with extreme disruption of the stratospheric vortex, and significant lofting of the stratopause. In 2004-2005 there are several large amplitude planetary wave events. However, there is little interaction between the stratospheric vortex and the Aleutian anticyclone, leading to a robust stratospheric vortex, and no stratospheric warming. In all three winters we find that the periods of planetary wave breaking are characterized by tilting and inter twining of the vortex and anticyclone, peaks in the planetary wave amplitudes, and negative Eliassen-Palm flux divergence. Our analyses of the synoptic structure and the planetary wave activity of the wintertime Arctic middle atmosphere shows that during winters when the amplitudes of the planetary waves are similar, the planetary wave action and resultant synoptic structure can be markedly different.

3.4.2. Chatanika Perspective

In Figure 3.9 we plot the temporal evolution of the stratospheric vortex (in green) and Aleutian anticyclone (in red) over Chatanika, Alaska over the altitude range of ~14-48 km (isentropic surfaces from 400 K to 2000 K) for DJF of the three successive winters. The three successive winters show distinctive differences in the temporal evolution of the stratospheric vortex and Aleutian anticyclone over Chatanika. The planetary wave activity is evident as the vortex and Aleutian anticyclone cross over this site.

During the 2002-2003 winter the vortex dominates above 1000 K (~33 km) while the anticyclone is sampled at lower altitudes. During the January 2003 major stratospheric warming the Aleutian anticyclone extends to (at least) 2000 K (~48 km). During the 2003-2004 winter the Aleutian anticyclone is over Chatanika during the second half of December, reflecting that the vortex and anticyclone are quasi-stationary in December. During the major stratospheric warming in January 2004 there is a transition to a regime where the vortex remains overhead above 800 K (~29 km) and the anticyclone appears on a day-to-day basis at lower altitudes. During the 2004-2005 winter the large vortex extends over Chatanika for all of December and January. The appearance of the anticyclone overhead in the second half of February coincides with the planetary wave activity during that period. The synoptic structure in 2002-2003 shows more variability over Chatanika, with the repeated movement of the vortex and anticyclone over the site, while in 2003-2004 and 2004-2005 there is less variability.

We plot the horizontal wind and the associated cumulative distribution functions at the 500 K (~19 km, ~60 hPa), 800 K (~30 km, ~10 hPa) and 1600 K (~44 km, ~1 hPa) isentropic surfaces above Chatanika in Figure 3.10. The interannual variations in the wind speeds are clearly evident with significantly higher winds in 2004-2005. In 2002-2003 the reduction in winds correspond to the presence of the Aleutian anticyclone, except during the period of the major stratospheric warming in the second half of January when there is an increase in the winds during the period when the Aleutian anticyclone extends up to 2000 K. On 18 January 2003 at 800 K the Aleutian anticyclone is over Alaska with stronger winds compared to the weak winds inside the split vortex (Figure 3.7) and the horizontal wind over Chatanika inside the anticyclone was 42.6 m/s. In 2003-2004 the decrease in the winds in the second half of December corresponds to the appearance of the Aleutian anticyclone. The anticyclone appears first at the upper altitudes and the winds weaken here first. On 5 January 2004 at 800 K the Aleutian anticyclone is over the western Arctic with weak winds (Figure 3.7) and the horizontal wind over Chatanika inside this anticyclone was 11.2 m/s, a factor of 3.8 less than the wind over Chatanika on 18 January 2003. In 2004-2005 the winds remain strong from

early December through early February as the vortex remains overhead (Figure 3.7) and the horizontal wind inside the vortex over Chatanika on 18 January 2005 was 58.9 m/s. The decrease in wind speeds in late February coincides with the appearance of the Aleutian anticyclone over Chatanika.

We plot the mean monthly wind profiles at Chatanika in Figure 3.11. In all three years the wind speeds increase in the troposphere with a local maximum near the tropopause (~320 K), decrease in the lower stratosphere and then increase through the stratosphere. The winds in 2004-2005 are clearly fastest while the winds in 2003-2004 are slowest. The interannual variability in the vortex and anticyclone positions shown in Figure 3.9 is reflected in the interannual variability in monthly mean wind profiles in Figure 3.11. During the winter of 2002-2003 there is significant month-to-month variability in the winds above 500 K. During the winter of 2003-2004 the wind profiles for January and February show similar winds up to 800 K. During the winter of 2004-2005 the wind profiles for December and January show similar winds up to 900 K. The disruption of the stratosphere in 2003-2004 is also evident in that the expected upper stratospheric jet (i.e., wind maximum between 1200 K (~38 km, 3 hPa) and 1800 K (~45 km, ~0.8 hPa) observed in 2002-2003 and 2004-2005 is not observed. At 500K the average winter wind speed in 2003-2004 is 10.3 m/s, a factor 1.2 and 3.3 times less than the average winds in 2002-2003 and 2004-2005 respectively. The interannual difference is greatest at 800 K where the average winter wind speed in 2003-2004 is 14.8 m/s, a factor 1.9 and 3.9 times less than the average winds in 2002-2003 and 2004-2005, respectively. This interannual variation decreases at 1600 K where the average winter wind speed in 2003-2004 is 43.3 m/s, similar to the value of the wind speed in 2002-2003 of 42.2 m/s and a factor of 1.4 times less than the average winds in 2004-2005. The weakest winds are found in January 2004 and the interannual differences are most pronounced in January when the monthly average wind speed at 500 K is 6.5 m/s, a factor 1.9 and 5.9 times less than the average winds in 2002-2003 and 2004-2005 respectively. At 800 K the difference is again more pronounced when the average wind speed for January is 8.9 m/s, a factor 3.5 and 7.5 times less than the average winds in

2002-2003 and 2004-2005 respectively. The difference is less pronounced at 1600K when the average wind speed for January is 28.3 m/s, a factor 1.2 and 2.5 times less than the average winds in 2002-2003 and 2004-2005 respectively.

3.5. Variability of Gravity Wave Activity and Synoptic Structure

To understand the relationship between the synoptic structure of the middle atmosphere and the gravity wave activity at Chatanika we calculate the linear correlation between the potential energy density of the gravity waves at 40-50 km and the horizontal wind speeds at each of the altitudes. For 28 gravity wave measurements over the three winters we find that the correlation coefficient is greater than 0.6 between 300 K (~6 km, 420 hPa) and 700 K (~27 km, 16 hPa). The maximum correlation of 0.74 is found at 400 K (~14 km, ~130 hPa) (Figure 3.12). This suggest that about 50% ($r^2 = 0.55$) of the day-to-day variability of the gravity wave activity in the upper stratosphere is related to the variation of the mean wind speed in the lower stratosphere. This correlation of 0.74 at 400 K is the same as the value of 0.73 found by Wilson and colleagues from Rayleigh lidar measurements of gravity waves in the 30-45 km altitude range and winds at 50 hPa (~20 km) at BIS and OHP [*Wilson et al*., 1991].

Our analysis indicates that the gravity wave activity in the upper stratosphere is significantly modulated by the horizontal wind speed in the lower stratosphere with larger potential energies associated with larger wind speeds. The fact that the correlations are highest with the winds in the regions where the wind speeds are lowest indicates that the physical process underlying the modulation is critical layer filtering of low-frequency waves with low horizontal phase speeds in the altitude regions where the winds are weakest. The interannual variation in the energy growth lengths can be understood in terms of the local winds at 1600 K (Figure 3.10 upper panel) and internal wave instabilities. In 2002-2003 the growth of the gravity waves with altitude is not limited by critical layer filtering in weak winds (average of 40.0 m/s on the nights of the lidar measurements) nor internal instabilities in the waves themselves. In 2003-2004 the reduced growth of the waves with altitude arises from continued critical layer filtering of

waves in the weaker winds (average of 31.9 m/s on the nights of the lidar measurements) at these upper altitudes. In 2004-2005 the large amplitude gravity waves propagating in higher winds (average of 53.9 m/s on the nights of the lidar measurements) are limited by internal convective and dynamic instabilities and have growth lengths that are longer than in 2003-2004 but shorter than in 2002-2003. Thus the light winds associated with the disruption of the middle atmosphere circulation in 2003-2004 serves to reduce the amount of wave energy in the upper stratosphere and lower mesosphere in two ways. Weak winds in the lower stratosphere block the propagation of gravity waves from below, while weak winds in the upper stratosphere and lower mesosphere dissipate the waves at those altitudes.

The inter-annual variations in the gravity wave activity (Figure 3.4) are consistent with the observed variations in the monthly mean temperature profiles at Chatanika (Figure 3.2). In 2002-2003 the stratosphere has a typical structure and is colder than the multi-year averages with intermediate gravity wave activity. In 2003-2004 the stratosphere has an elevated stratopause and the stratosphere is significantly colder than the multi-year averages with reduced gravity wave activity relative to 2002-2003. In 2004-2005 the stratosphere has a typical structure and is warmer than the multi-year averages with increased gravity wave activity relative to 2002-2003. These observations are consistent with the work of *Kanzawa* [1989] and *Hitchman et al*. [1989] who studied the structure of the polar winter stratopause. *Kanzawa* [1989] found that the winter polar stratopause was often warmer than at lower latitudes despite the fact that there is more solar heating of stratospheric ozone at lower latitudes. *Hitchman et al*. [1989] found that the winter polar stratopause was often separated from the stratopause at lower latitude indicating the presence of a distinct pool of warm air in the upper stratosphere in the polar region. Both *Kanzawa* [1989] and *Hitchman et al*. [1989] concluded that the heating of the polar stratopause results from adiabatic heating in the descending gravity-wave driven circulation of the winter pole. This adiabatic heating is greater than the radiative cooling. Thus we conclude that, in 2004-2005, more abundant gravity waves in the upper stratosphere propagate upward into the mesosphere, break at mesospheric

heights, and drive a strong meridional circulation that results in stronger descent at the winter pole and stronger adiabatic warming. In 2002-2003, less abundant gravity waves in the upper stratosphere propagate upward into the mesosphere, break at mesospheric heights, and drive a weaker meridional circulation that results in weaker descent at the winter pole and weaker adiabatic warming. In 2003-2004, the gravity waves are suppressed, the meridional circulation is disrupted, the stratosphere is dominated by radiative cooling, and an elevated stratopause forms.

This physical scenario is the same as that presented in the study of *Siskind et al*. [2007] of the elevated stratopause in February 2006. *Siskind et al.* [2007] use a general circulation model to show that a major stratospheric warming results in the disruption of the stratospheric circulation, subsequent suppression of the gravity wave driven circulation and hence the formation of the elevated stratopause. *Siskind et al.* [2007] model the gravity wave activity as a orographic gravity wave drag parameterization which can be turned on and off in the model. In their analysis of the Arctic middle atmosphere in February 2006, the two sets of model results where the model internally suppresses the gravity waves and where the gravity wave drag is turned off in the model both yield the observed elevated stratopause and the authors conclude that the elevated stratopause results from the suppression of orographic gravity waves.

3.6. Summary and Conclusion

We have characterized the gravity wave density fluctuations in the upper stratosphere (40-50 km) from Rayleigh lidar observations at Chatanika over three winters (DJF 2002-2003, DJF 2003-2004, DJF 2004-2005). These winters have significant differences in their meteorological conditions which we have characterized using SABER observations and MetO analyses data. Over all three winters, regardless of the meteorological conditions, we find that the gravity wave potential energy densities are lower than those measured at mid-latitude sites [*Wilson et al*., 1991]. The day-to-day variation in the gravity wave energy densities is positively correlated with the weakest winds in the lower stratosphere. This is consistent with the study of *Dunkerton and*

Butchart [1984], that synoptic conditions in the western Arctic block the upward transmission of gravity waves.

However, the magnitude and vertical growth length of the gravity wave potential energy per unit mass is significantly different in each winter. The magnitude of the gravity wave potential energy densities is significantly lower in 2003-2004 than in the other two winters, with the largest energy densities found in 2004-2005. This reduced gravity wave activity in 2003-2004 coincides with a major disruption of the circulation, the formation of an elevated stratopause, and a reduction in the stratospheric winds. The growth of the waves in 2002-2003 and 2003-2004 appear to be limited by critical layer interactions with the wind, while the growth of the larger amplitude gravity waves in 2004-2005 appears to be limited by internal instabilities.

In each of the three winters the gravity wave activity and temperature structure of the stratosphere and mesosphere are consistent in terms of the gravity-wave driven circulation and formation of the polar stratopause. In 2004-2005, when there are no stratospheric warming events, the gravity wave activity is highest and the stratopause temperatures are warmest. In 2002-2003, when there are several stratospheric warming events, the gravity wave activity is lower and the stratopause temperatures are colder. In 2003-2004, when one of the most prolonged mid-winter stratospheric warming events occurred, the gravity wave activity is lowest, the stratosphere is dominated by radiative cooling, and the stratopause is displaced vertically to ~70 km. These lidar observations provide direct evidence of the suppression of gravity wave activity during an elevated stratopause event and observationally confirm the recent modeling study by *Siskind et al.* [2007] that attributes the formation of the elevated stratopause to the suppression of gravity wave activity. Winters such as 2003-2004 may become more common as recent studies indicate that increase in greenhouse gases could increase the tropospheric wave forcing and strengthen the planetary wave activity in the stratosphere [*Butchart et al*., 2006; *Deckert and Dameris*, 2008].

Acknowledgments The authors thank the staff at Poker Flat Research Range for their ongoing support of the lidar program. The authors thank the following University of Alaska students for their assistance in making the ongoing lidar observations; J. Breese, L. Cutler, T. Hao, S. Nadakuditi, K. Nowicki, M. Peshave, T. Stern, L. Su, W. Wang, and J. Yue. The authors thank Dr. K. Sakanoi of Komazawa University for her assistance with the lidar measurements in spring 2003. The authors acknowledge the SABER science and data processing teams for providing the SABER data presented in the paper. The authors acknowledge support from the United States National Science Foundation under grants ARC 0632387 and ATM 0640340. PFRR is a rocket range operated by Geophysical Institute-University of Alaska Fairbanks with support from the United States National Aeronautic and Space Administration.

References

Andrews, D. G., J. R. Holton, and C. B. Leovy (1987), *Middle atmosphere dynamics*, 489 pp., Academic Press Inc., New York.

Beaumont, K. (2008), SABER: Sounding of the atmosphere using broadband emission radiometry, http://saber.gats-inc.com/, data accessed 2008.

Brewer, A. W. (1949), Evidence for a world circulation provided by the measurements of helium and water vapour distribution in the stratosphere, *Quart. J. Roy. Meteor. Soc*., *75*, 351-363.

Butchart, N., A. A. Sciafe, M. Bourqui, J. de Grandpré, S. H. E. Hare, J. Kettleborough, U. Langematz, E. Manzini, F. Sassi, K. Shibata, D. Shindell, M. Sigmond (2006), Simulations of anthropogenic change in the strength of the Brewer-Dobson circulation, *Clim. Dyn.*, 27, 727-741, doi:10.1007/s00382-006-0612-4.

Charlton, A. L., and L. M. Polvani (2007), A new look at stratospheric sudden warmings. Part 1: Climatology and modeling benchmarks, *J. Clim*, *20*, 449 - 469.

Deckert, R., and M. Dameris (2008), From ocean to stratosphere, *Science*, *322*, 53-55.

Dobson, G. M. B. (1956), Origin and distribution of the polyatomic molecules in the atmosphere, *Proc. Roy. Soc. London*, *A236*, 187-193.

Duck, T. J., J. A. Whiteway, and A. I. Carswell (1998), Lidar observations of gravity wave activity and Arctic stratospheric core warming, *Geophys. Res. Lett.*, *25*(15), 2813-2816.

Duck, T. J., J. A. Whiteway, and A. I. Carswell (2001), The gravity wave-Arctic stratospheric vortex interaction, *J. Atm. Sci.*, *58*, 3581-3596.

Dunkerton, T. J., and N. Butchart (1984), Propagation and selective transmission in internal gravity waves in a sudden warming, *J. Atmos. Sci.*, *41*(8), 1443-1460.

Fritts, D. C., and M. J. Alexander (2003), Gravity wave dynamics and effects in the middle atmosphere, *Rev. Geophys*., 41 (1), 1003, doi:10.1029/2001RG000106.

Fritts, D. C., and P. K. Rastogi (1985) Convective and dynamical instabilities due to gravity wave motions in the lower and middle atmosphere: Theory and observations, *Radio Sci.*, 20, 1247-1277.

Gerrard A. J., T. J. Kane, J. P. Thayer, T. J. Duck, J. A. Whiteway, and J. Fiedler (2002), Synoptic scale study of the Arctic polar vortex's influence on the middle atmosphere, 1, Observations, *J. Geophys. Res.*, *107* (D16), 4276, doi:10.1029/2001JD000681.

Gill, H. E. (1982), *Atmosphere - ocean dynamics*, 662 pp., Academic Press Inc., New York.

Harvey V. L., R. B. Pierce, T. D. Fairlie, and M. H. Hitchman (2002), A climatology of stratospheric polar vortices and anticyclones, *J. Geophys. Res., 107*(D20), 4442, doi:10.1029/2001JD001471.

Hauchecorne, A., J.-L. Bertaux, F. Dalaudier, J. M. Russell III, M. G. Mlynczak, E. Kyrölä, and D. Fussen (2007), Large increase of NO_2 in the north polar mesosphere in January-February 2004: Evidence of a dynamical origin from GOMOS/ENVISAT and SABER/TIMED data, *Geophys. Res. Lett.*, *34*, L03810, doi:10.1029/2006GL027628.

Hitchman, M. H., J. C. Gille, C. D. Rodgers, and G. Brasseur (1989), The separated polar winter stratopause: A gravity wave-driven climatological feature, *J. Atmos. Sci.*, *46*, 410-422.

Holton, J. R., and M. J. Alexander (2000), The role of waves in the transport circulation of the middle atmosphere, in *Atmospheric Science Across the Stratopause*, *Geophys. Monogr. Ser.*, vol. 123, edited by D. E. Siskind, S. D. Eckermann, and M. E. Summers, pp. 21-35, AGU, Washington, D. C.

Holton, J. R., P. H. Haynes, M. E. McIntyre, A. R. Douglass, R. B. Rood, L. Pfister (1995), Stratosphere-Troposphere Exchange, *Rev. Geophys.*, 33 (4), doi:10.1029/95RG02097.

Houghton, J. T. (1978), The stratosphere and mesosphere, *Quart. J. Royal Met. Soc.*, *104*, 1-29.

Kanzawa, H. (1989), Warm stratopause in the Antarctic winter, *J. Atmos. Sci*., *40*, 2497-2507.

Labitzke, K. (1972), Temperature changes in the mesosphere and stratosphere connected with circulation changes in winter, *J. Atmos. Sci*., 29, 756-766.

Manney, G. L., K. Kruger, J. L. Sabutis, S. A. Sena, and S. Pawson (2005), The remarkable 2003-2004 winter and other recent winters in the Arctic stratosphere since the late 1990s, *J. Geophys. Res.*, *110*, D04107, doi:10.1029/2004JD005367.

Manney, G. L., M. L. Santee, L. Froidevaux, K. Hoppel, N. J. Livesey, and J. W. Walters (2006), EOS MLS observations of ozone loss in the 2004-2005 Arctic winter, *Geophys. Res. Lett.*, *33*, L04802, doi:10.1029/2005GL024494.

Manney, G. L., K. Krüger, S. Pawson, K. Minschwaner, M. J. Schwartz, W. H. Daffer, N. J. Livesey, M. G. Mlynczak, E. E. Remsberg, J. M. Russell III, J. W. Waters, (2008), The evolution of the stratopause during the 2006 major warming: Satellite data and assimilated meteorological analyses, *J. Geophys. Res*., 113, D11115, doi:10.1029/2007JD009097.

Matsuno, T. (1971), A dynamical model of the stratospheric sudden warming, *J. Atmos. Sci*. .28, .1479–1494.

Mertens, C. J., F. J. Schmidlin, R. A. Goldberg, E. E. Remsberg, W. D. Pesnell, J. M. Russell III, M. G. Mlynczak, M. Lopez-Puertas, P. P. Wintersteiner, R. H. Picard, J. R. Winick, and L. L. Gordley (2004), SABER observations of mesospheric temperatures and comparisons with falling sphere measurements taken during the 2002 summer MaCWAVE campaign, *Geophys. Res. Lett*., *31*(3), L03105, doi:10.1029/2003GL018605.

Mizutani, K., T. Itabe, M. Yasui, T. Aoki, Y. Murayama, and R. L. Collins (2000), Rayleigh and Rayleigh Doppler lidars for the observations of the Arctic middle atmosphere, *IEICE Trans. Fundam. Electron. Commun. Comput. Sci.,* E83-B, 2003.

Randall, C. E., V. L. Harvey, C. S. Singleton, P. F. Bernath, C. D. Boone, and J. U. Kozyra (2006), Enhanced NO_x in 2006 linked to strong upper stratospheric Arctic vortex, *Geophys. Res. Lett.*, *33*, L18811, doi:10.1029/2006GL027160.

Randel, W., P. Udelhofen, E. Fleming, M. Geller, M. Gelman, K. Hamilton, D. Karoly, D. Ortland, S. Pawson, R. Swinbank, F. Wu, M. Baldwin, M.-L. Chanin, P. Keckhut, K. Labitzke, E. Remsberg, A. Simmons, and D. Wu (2004), The SPARC intercomparison of middle- atmosphere climatologies, *J. Climate*, *17*(5), 986-1003.

Rex, M., R. J. Salawitch, H. Deckelmann, P. von der Gathen, N. R. P. Harris, M. P. Chipperfield, B. Naujokat, E. Reimer, M. Allaart, S. B. Anderson, R. Bevilacqua, G. O. Braathen, H. Claude, J. Davies, H. De Backer, H. Dier, V. Dorokhov, H. Fast, M. Gerding, S. Godin-Beekmann, K. Hoppel, B. Johnson, E. Kyrö, Z. Litynska, D. Moore, H. Nakane, M. C. Parrondo, A. D. Risley Jr., P. Skrivankova, R. Stübi, P. Viatte, V. Yushkov, and C. Zerefos (2006), Arctic winter 2005: Implications for stratospheric ozone loss and climate change, *Geophys. Res. Lett.*, *33*, L23808, doi:10.1029/2006GL026731.

Russell, J. M. III, M. G. Mlynczak, L. L. Gordley, J. Tansock, and R. Esplin (1999), An overview of the SABER experiment and preliminary calibration results, *Proceedings of the SPIE*, 44th Annual Meeting, Denver, Colorado, July 18-23, 3756, 277-288.

Schoeberl, M. R., and D. L. Hartmann, (1991), The dynamics of the stratospheric polar vortex and its relation to springtime ozone depletion, *Science, 251*, 46-52,

Shepherd, T. G. (2000), The middle atmosphere, *J. Atmos. Sol. Terr. Phys.*, *62*, 1587-1601.

Singleton, C. S., C. E. Randall, M. P. Chipperfield, S. Davies, W. Feng, R. M. Bevilacqua, K. W. Hoppel, M. D. Fromm, G. L. Manney, and V. L. Harvey (2005), 2002-2003 Arctic ozone loss deduced from POAM III satellite observations and the SLIMCAT chemical transport model, *Atmos. Chem. Phys.*, *5*, 597-609.

Siskind, D. E., S. D. Eckermann, L. Coy, J. P. McCormack, and C. E. Randall (2007), On recent interannual variability of the Arctic winter mesosphere: Implications for tracer decent, *Geophys. Res. Lett., 34,* L09806, doi:10.1029/2007GL029293.

Smith, S. A., D. C. Fritts, and T. E. VanZandt (1987), Evidence for a saturated spectrum of atmospheric gravity waves, *J. Atmos. Sci., 44*, 1404-1410.

Solomon, S. (1999), Stratospheric ozone depletion: A review of concepts and history, *Rev. Geophys.*, 37 (3), doi:10.1029/1999RG900008.

SPARC, 2002: *SPARC Intercomparison of Middle Atmosphere Climatologies*, SPARC Rep. 3, 96 pp., 2002.

Thurairajah, B., R. L. Collins, and K. Mizutani (2009), Multi-Year temperature measurements of the middle atmosphere at Chatanika, Alaska (65°N, 147°W), *Earth Planets Space*, *61*, 755-764.

Wang, W. (2003) *Spectral estimation of signal and noise power in Rayleigh lidar measurements of the middle atmosphere*, MS Thesis, University of Alaska Fairbanks.

Whiteway, J. A., and A. I. Carswell (1994), Rayleigh lidar observations of thermal structure and gravity wave activity in the high Arctic during stratospheric warming, *J. Atmos. Sci.*, *51*(21), 3122-3136.

Wilson, R., M. L. Chanin, and A. Hauchecorne (1991), Gravity waves in the middle atmosphere observed by Rayleigh lidar 2. Climatology, *J. Geophy. Res., 96*(D3), 5169-5183.

Table 3.1. Buoyancy period and gravity wave activity at 40-50 km at Chatanika, Alaska (65°N, 147°W).

	15-16 January 2004	10-11 January 2005
Buoyancy Period (s) [a]	285	305
RMS Density (%) [b]	0.41	1.10
RMS Vertical Displacement (m)	81	250
Potential Energy Density (J/kg)	1.6	13.3
SNR	1.4	8.2

a. Calculated from nightly average temperature profile.

b. Fluctuations over 2 – 10 km and 0.5 – 4 h.

Table 3.2. Buoyancy period and gravity wave activity at 40-50 km at Chatanika, Alaska (65°N, 147°W) during DJF of 2002-2003, 2003-2004, and 2004-2005.

	2002-2003	2003-2004	2004-2005
Number of Observations	15	8	6
Buoyancy Period (s) [a]			
Average [b]	309 (± 5)	291 (± 9)	301 (± 8)
Range [c]	278-353	264-330	274-328
RMS Relative Density (%) [d]			
Average	0.41 (± 0.04)	0.32 (± 0.03)	0.69 (± 0.13)
Minimum	0.17-0.68	0.21-0.44	0.30-1.10
RMS Vertical Displacement (m)			
Average	96 (± 9)	66 (± 7)	148 (± 25)
Range	46-156	43-110	78-250
Potential Energy Density (J/kg)			
Average	2.1 (± 0.4)	1.1 (± 0.2)	5.7 (± 1.8)
Range	0.4-4.8	0.5-2.4	1.1-13.3

a. Calculated from nightly average temperature profile.

b. Mean value and uncertainty in mean

c. Minimum value and maximum value

d. Fluctuations over 2 – 10 km and 0.5 – 4 h.

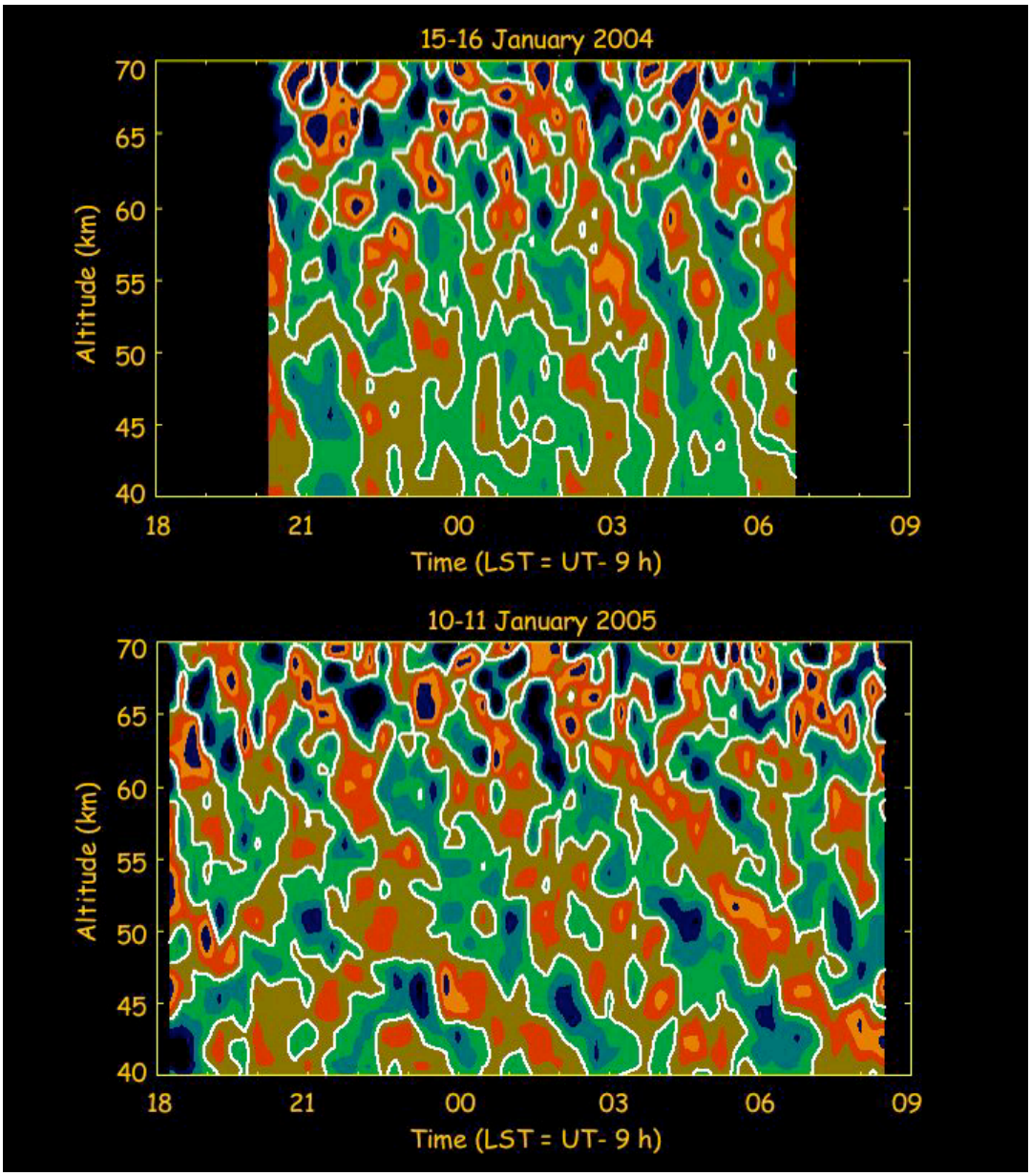

Figure 3.1. Relative density perturbations measured by Rayleigh lidar at Chatanika, Alaska on 15-16 January 2004 and 10-11 January 2005. The perturbations are spatially band-limited between wavelengths 2 km and 30 km and temporally band-limited between time periods of 30 minutes and 4 hours. The positive values are colored red (0-1%, 1-2%, >2%) and the negative values blue (0 - -1%, -1 - -2%, < -2%). The white contour marks the zero line.

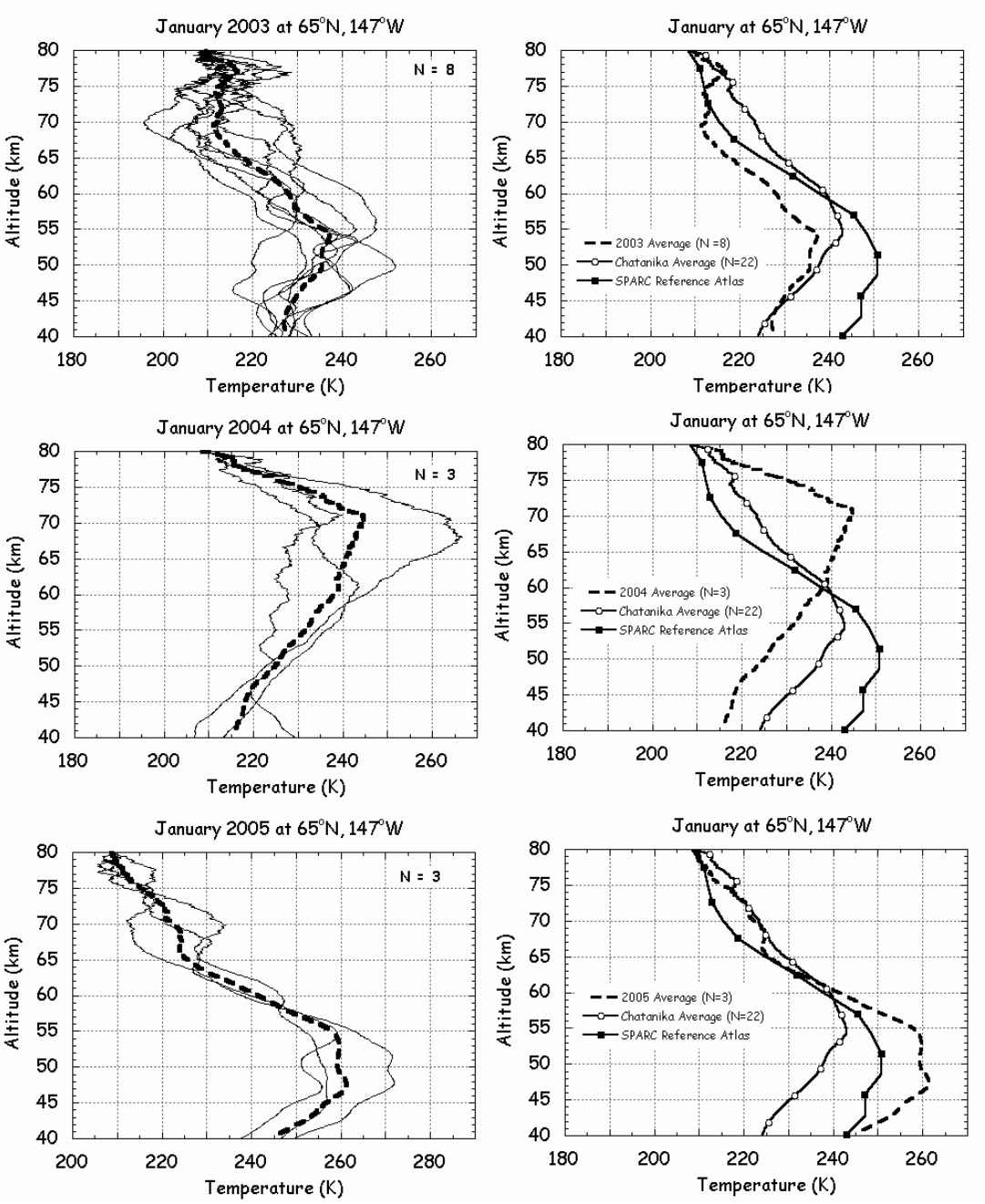

Figure 3.2. Nightly mean temperature profiles (solid line) measured by Rayleigh lidar at Chatanika, Alaska during January 2003 (7th, 10th, 14th, 22nd, 25th, 26th, 29th), 2004 (5th, 15th, 29th), and 2005 (10th, 18th, 27th). The monthly mean profile is plotted as a dashed line. 'N' is number of nighttime profiles for each month. (Right) January mean monthly temperatures at Chatanika averaged over 2003, 2004, 2005 (dashed line), averaged over 1998 to 2005 (solid line with open circle), and SPARC January temperature (solid line with solid square).

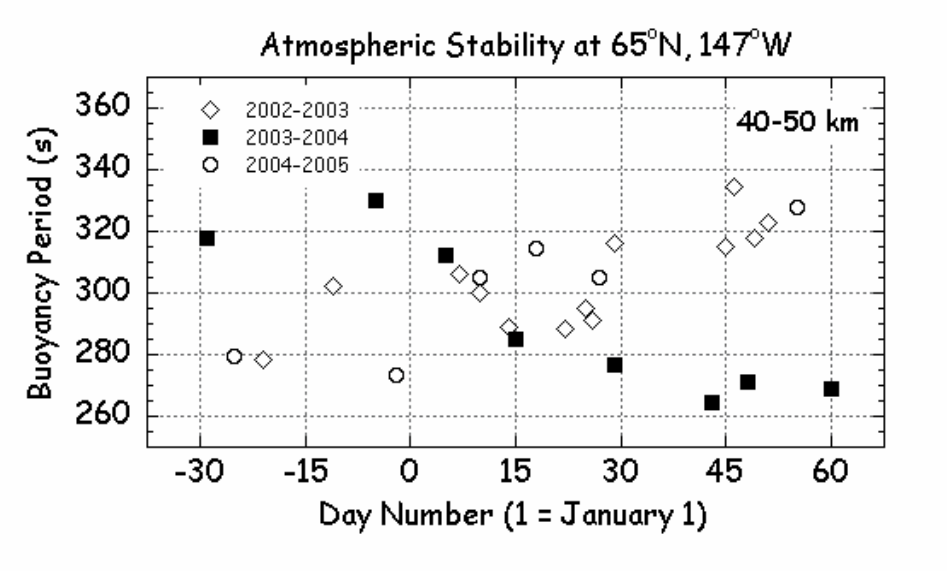

Figure 3.3. Atmospheric stability measured by Rayleigh lidar at Chatanika, Alaska during the 2002-2003, 2003-2004, and 2004-2005 winters averaged over 40-50 km altitude range.

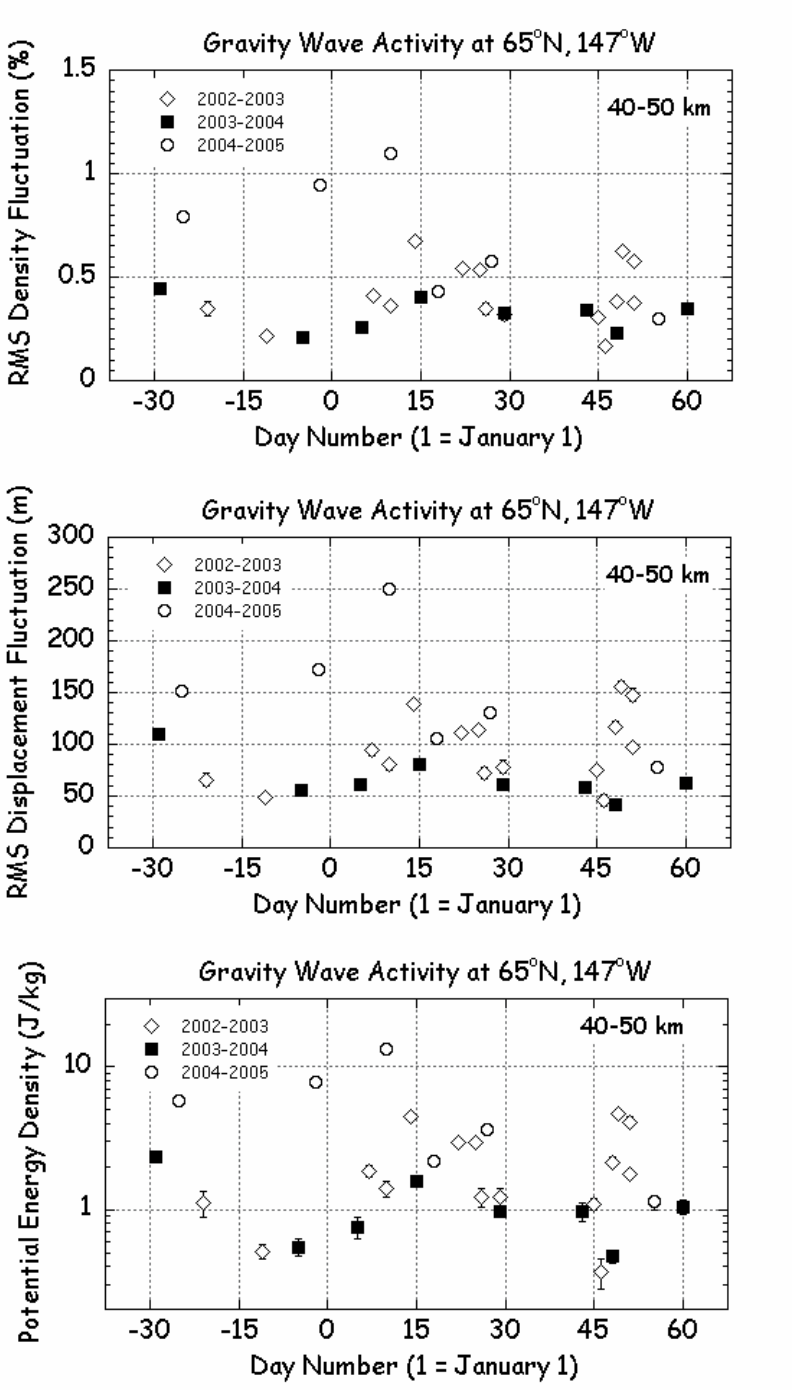

Figure 3.4. Gravity wave activity- (top) rms density fluctuation, (middle) rms displacement fluctuation, and (bottom) potential energy density measured by Rayleigh lidar at Chatanika, Alaska during the 2002-2003, 2003-2004, and 2004-2005 winters averaged over 40-50 km altitude range.

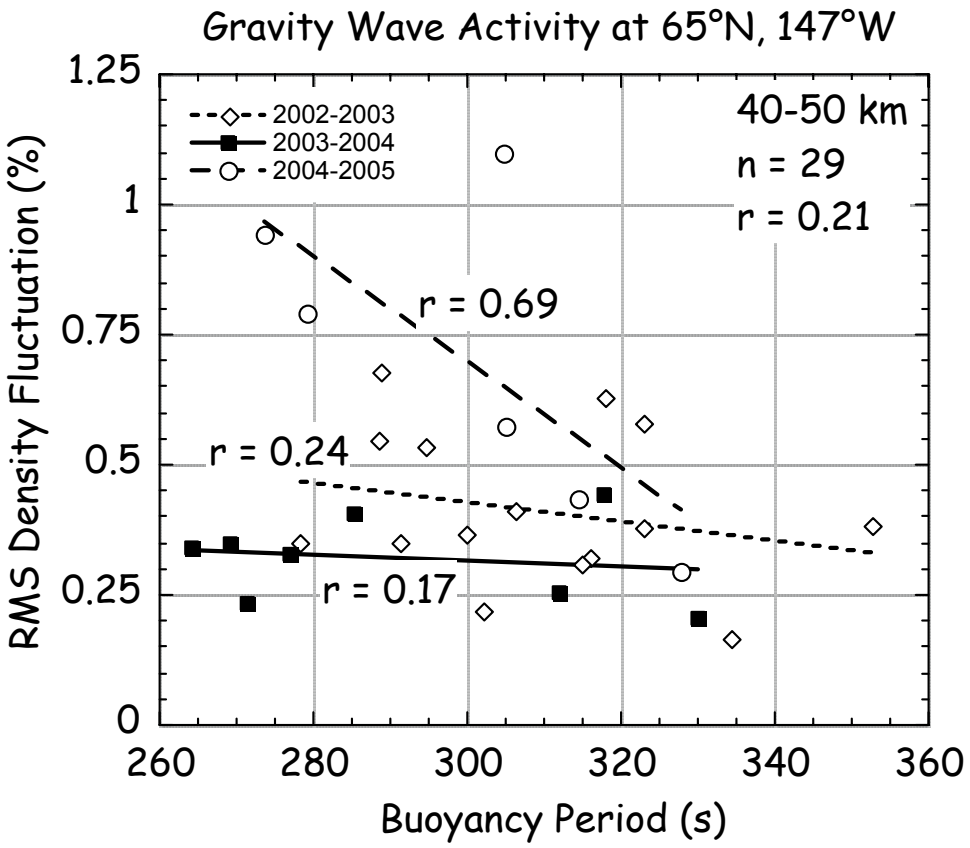

Figure 3.5. Variation of rms density fluctuation as a function of buoyancy period during the 2002-2003, 2003-2004, and 2004-2005 winters averaged over 40-50 km. The overall correlation coefficient is given as well as the linear fit and correlation coefficient for each winter.

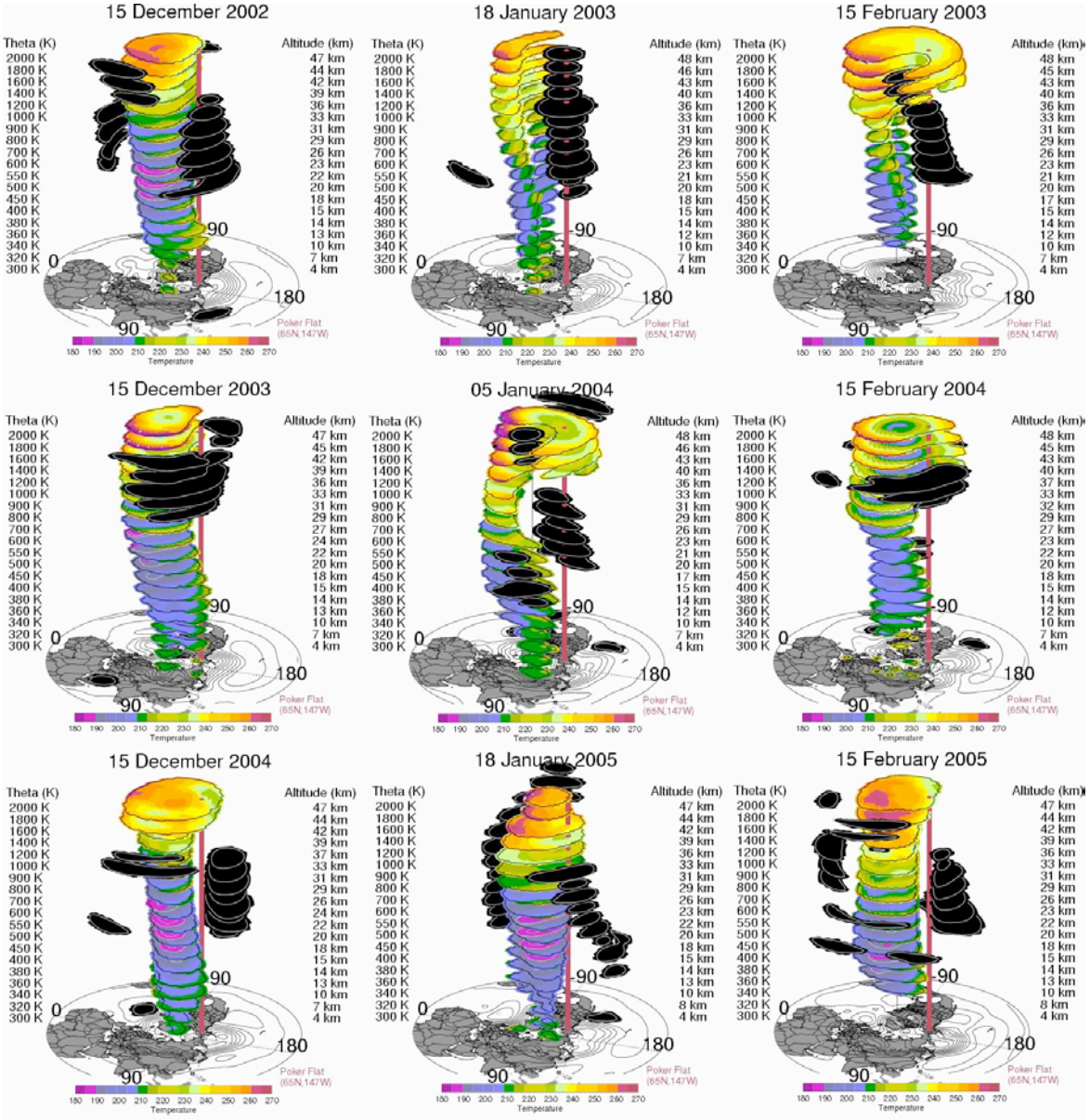

Figure 3.6. 3-D representation of the Arctic stratospheric vortex (color surfaces) and anticyclones (black surface) from 300 K to 2000 K isentropic surface on (top) 15 December, 18 January and 15 February of 2002-2003 (middle) 15 December, 5 January, and 15 February of 2003-2004 (bottom) 15 December, 18 January, and 15 February of 2004-2005. The vertical line is drawn upward from Chatanika, Alaska.

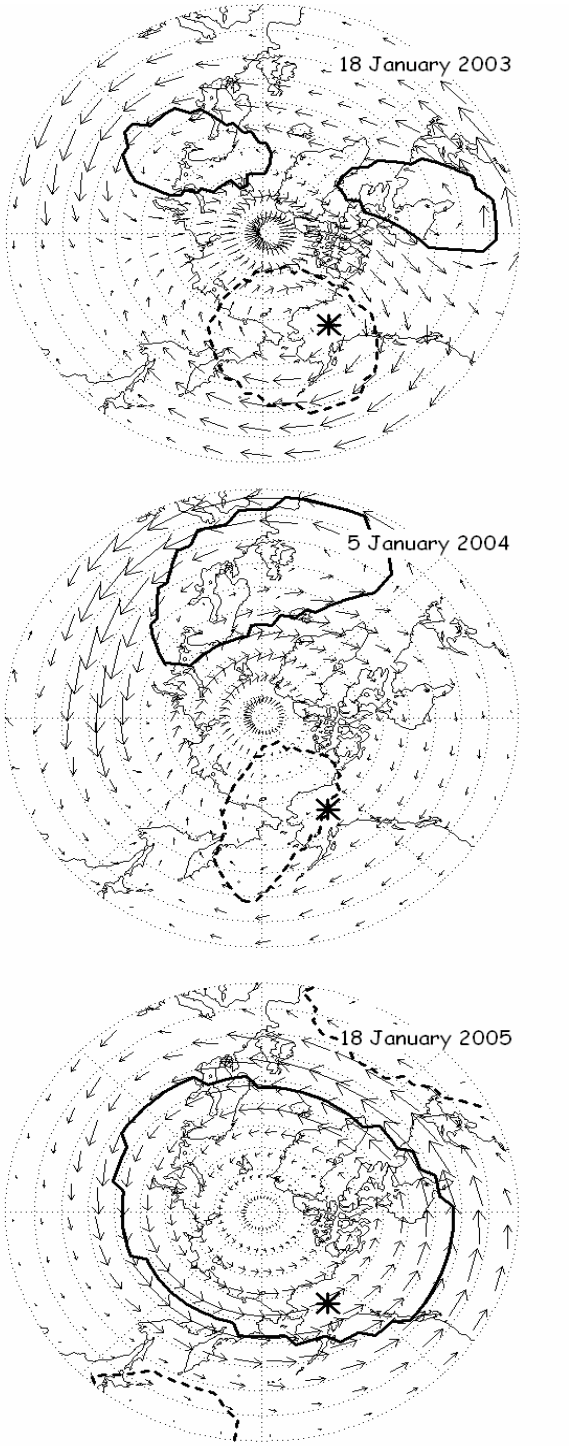

Figure 3.7. Northern hemisphere polar stereographic plots of vortex (thick line) and anticyclone (dashed line) at 800 K (~30 km, ~10 hPa) from MetO analyses data for (upper) 18 January 2003, (mid) 5 January 2004, and (lower) 18 January 2005. The horizontal winds are also plotted. Chatanika is marked with a plus symbol.

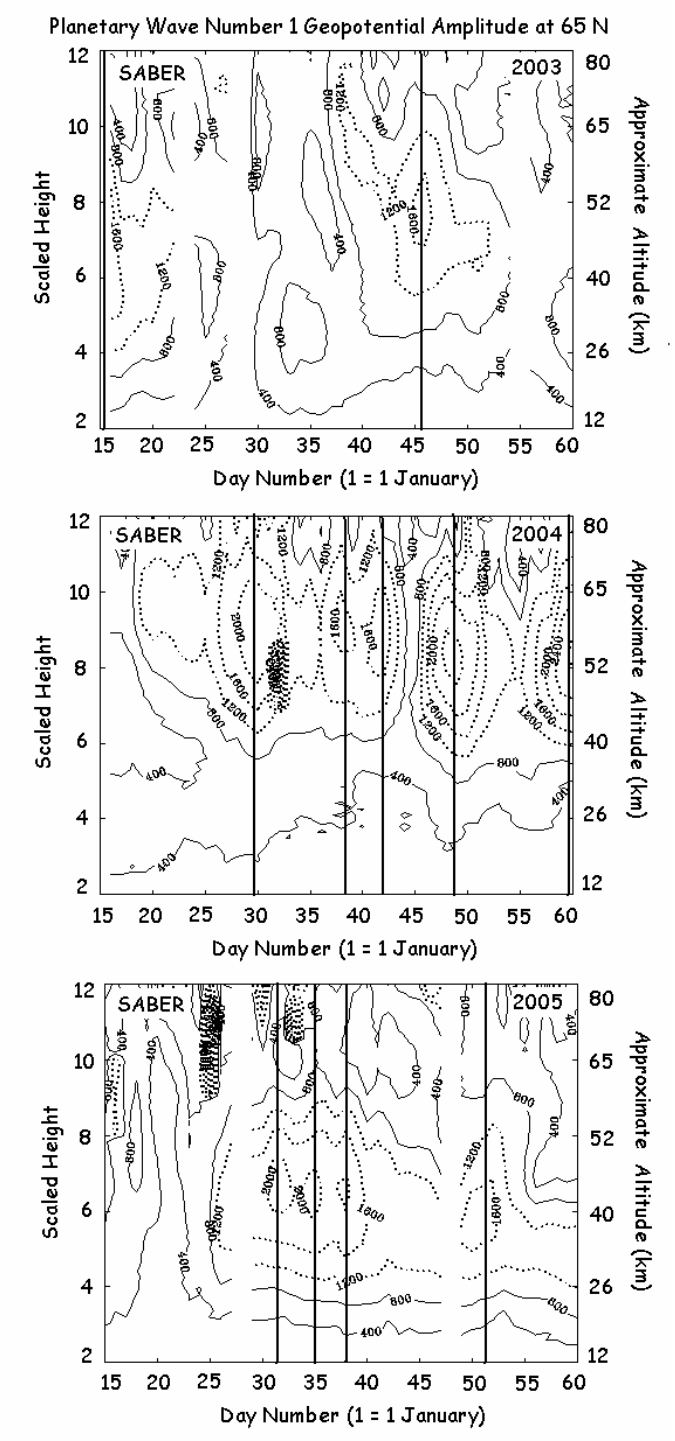

Figure 3.8. Planetary wave-one geopotential amplitude at 65^{o}N for second half of January and February of 2003, 2004, and 2005 measured by SABER. Geopotential amplitudes greater then 1000 are dotted lines. The contour interval is 400 m. The vertical lines mark the maximum amplitudes.

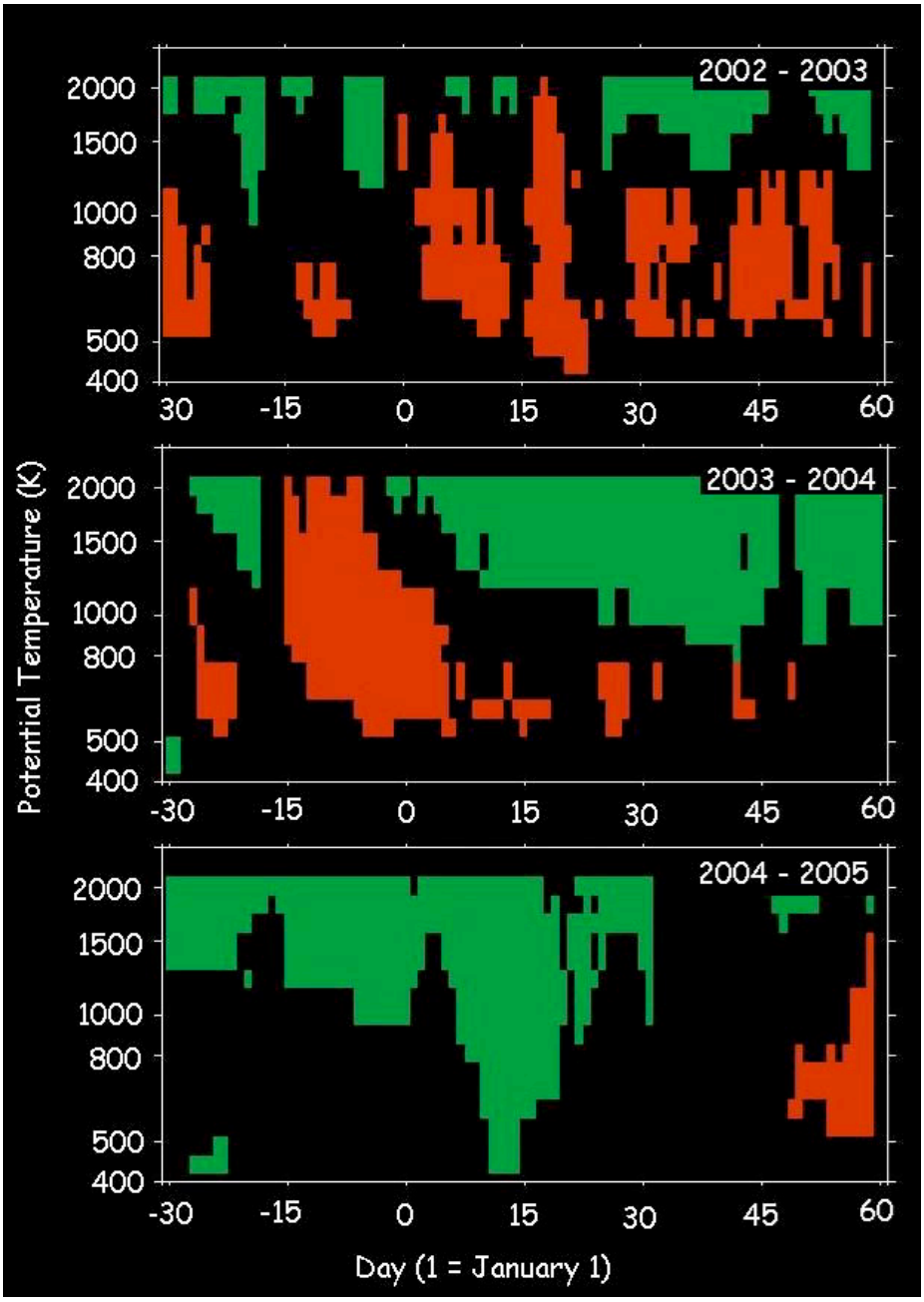

Figure 3.9. Temporal evolution of the stratospheric vortex (green) and Aleutian anticyclone (red) over Chatanika, Alaska from 400 K (~14 km, ~130 hPa) to 2000 K (~48 km, 0.6 hPa) isentropic surface during DJF of 2002-2003(upper), 2003-2004 (middle), and 2004-2005 (lower) winters. Black represents the time period when neither systems were above Chatanika.

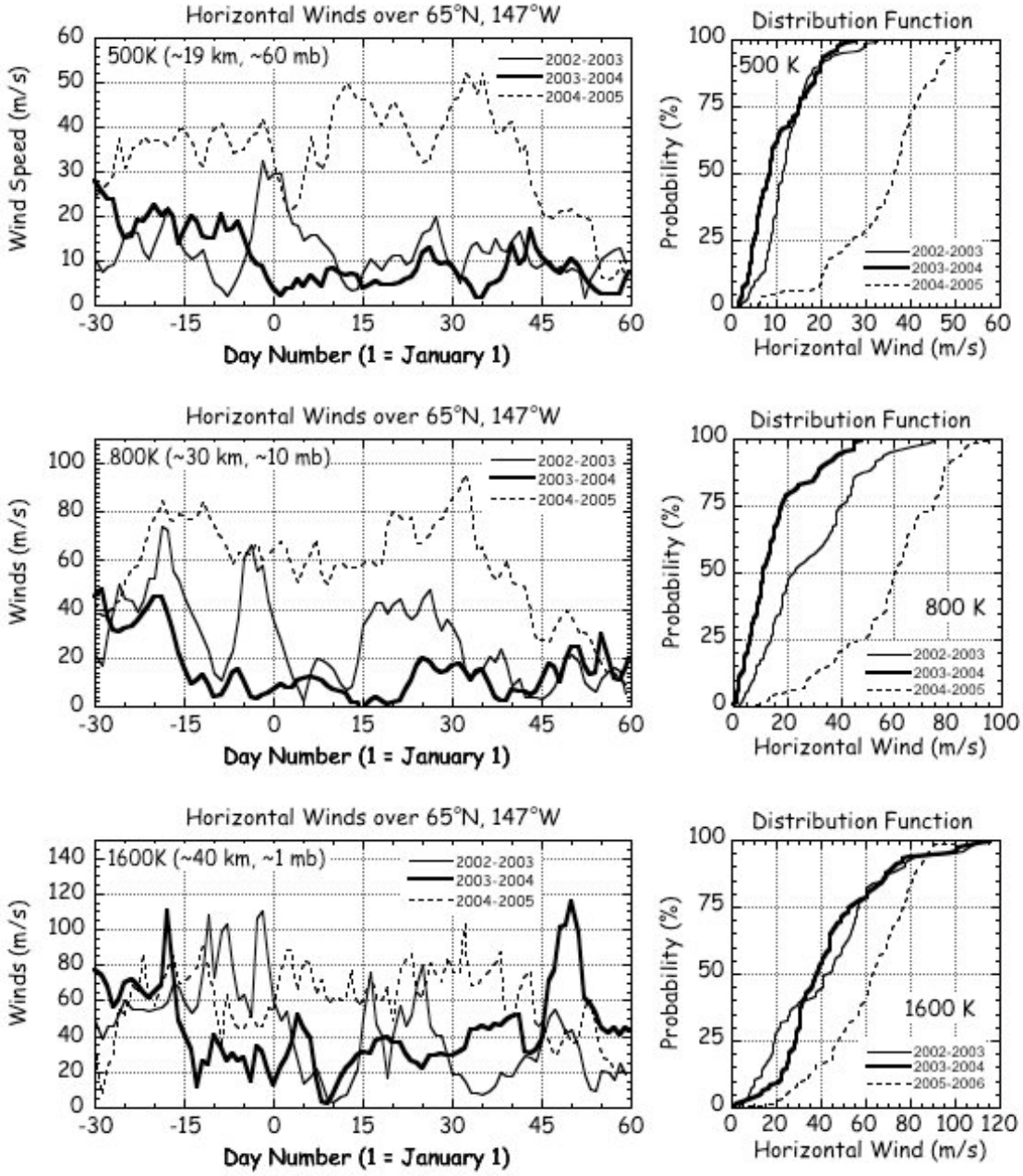

Figure 3.10. Daily wind speed from the MetO analyses data at 1600K, 800 K, and 500 K isentropic surfaces for DJF of 2002-2003 (upper), 2003-2004 (middle), and 2004-2005 (lower) Arctic winters. The corresponding cumulative distribution functions of the winds are plotted to the right.

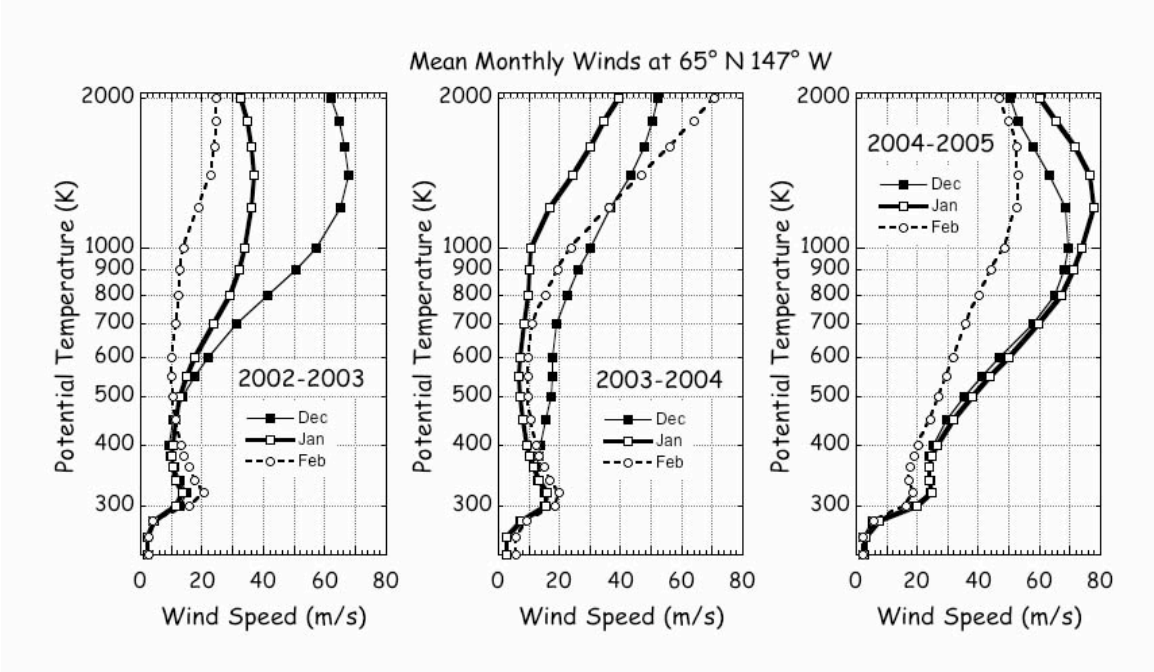

Figure 3.11. Mean monthly wind profiles calculated from the MetO analyses data for DJF of 2002-2003 (left), 2003-2004 (middle), and 2004-2005 (right) Arctic winters.

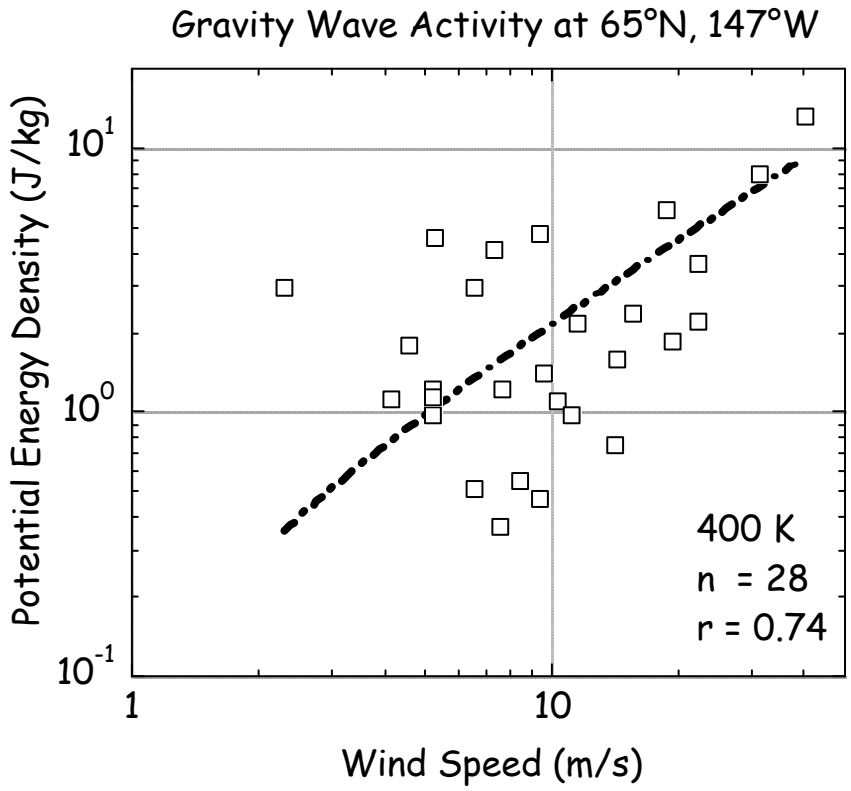

Figure 3.12. Scatter plot of potential energy density per unit mass averaged over the 40-50 km altitude range and MetO wind speed at 400 K isentropic surface. The linear correlation coefficient is 0.74.

Chapter 4. Gravity Wave Activity in the Arctic Stratosphere and Mesosphere during the 2007-2008 and 2008-2009 Stratospheric Sudden Warmings[1]

Abstract. We use Rayleigh lidar measurements of the stratosphere and mesosphere to document the gravity wave activity during the recent Arctic winters of 2007-2008 and 2008-2009 at Poker Flat Research Range, Chatanika, Alaska (65^{o}N, 147^{o}W). Both winters were characterized by different types of mid-winter warmings. Significant variability is observed in the gravity wave potential energy density. Monthly averaged values indicate a broad annual cycle with winter maximum of 4.1 J/kg in November. We use satellite data and global meteorological data to analyze the gravity wave activity in terms of the synoptic structure of the stratospheric vortex and Aleutian anticyclone and planetary wave activity. Although the two winters have different meteorological conditions we do not find any systematic differences between the magnitudes of gravity wave potential energy density during the two winters. We find a positive correlation between the gravity wave potential energy density and horizontal wind speed in the mid-stratosphere during both years. However the correlations are different, with a low correlation of 0.38 in 2007-2008 and a higher correlation of 0.95 in 2008-2009. This suggests that while the gravity wave activity in 2008-2009 winter is modulated by the background flow, other wave sources modulate the gravity wave activity during the 2008 warming.

---

[1]Thurairajah, B., R. L. Collins, V. L. Harvey, R. S. Lieberman, M. Gerding, J. Livingston (2009), Gravity wave activity in the Arctic stratosphere and mesosphere during the 2007-2008 and 2008-2009 stratospheric sudden warmings, in preparation for submission to *J. Geophys. Res.*

4.1. Introduction

Gravity waves have long been known to play a crucial role in the general circulation of the middle atmosphere. These small scale waves drive a pole-to-pole mesospheric circulation with ascending flow in the summer hemisphere and descending flow in the winter hemisphere [*Houghton*, 1978]. These vertical motions influence the cooling of the polar summer mesopause region and the warming of the polar winter stratopause region (e.g., see reviews by *Holton and Alexander*, 2000; *Fritts and Alexander*, 2003; and references therein). Gravity wave propagation is modulated by spatially varying winds. For example, studies [*Duck et al*., 1998; *Dunkerton and Butchart*, 1984] have shown that gravity wave propagation is modulated by the stratospheric vortex and Aleutian anticyclone, with higher gravity wave activity associated with the stronger winds in the edge of the polar vortex, and lighter winds in the anticyclone blocking the upward transmission of orographic gravity waves.

Direct measurements of gravity wave forcing that bring about the mesospheric circulation and the thermal structure is challenging. Recently *Liu et al.* [2009] have used zonal mean zonal momentum equations and direct wind measurements from lidar and satellite data to estimate a strong eastward gravity wave forcing during summer (~75 - 130 $ms^{-1}day^{-1}$) and a weak westward forcing in winter (~50 - 100 $ms^{-1}day^{-1}$) at mid-latitudes between 85-100 km. Tidal mean winds were separated from the wind measurements but winds due to planetary waves were assumed to be reduced at these altitudes due to the monthly averages over several years. However, the method is expected to introduce large errors in gravity wave forcing numbers if applied during stratospheric warming events when temporal winds are significantly different from zonal winds.

More recently *Wang and Alexander* [2009] have used satellite data to show variability in zonal mean gravity wave amplitude with altitude during the 2007-2008 northern hemisphere stratospheric warming events. They observe enhanced/suppressed zonal mean gravity wave amplitudes below/above ~35 km associated with the stratospheric warming/mesospheric cooling. The authors attribute this variability to the

weakening of the zonal winds at lower altitudes that refract the gravity waves in such a way that more waves are observed in the stratosphere (below ~35 km) and to the critical level filtering of upward propagating gravity waves by weak winds resulting in reduction of gravity wave activity in the mesosphere (above ~40 km). A reduction in gravity wave activity would mean less gravity wave forcing and a subsequent cooling of the mesosphere by relaxation to radiative equilibrium. Again, during stratospheric sudden warmings the temporal wind tends to be significantly different from the zonal averaged winds resulting in variable gravity wave activity along a latitude circle.

Thus, in an asymmetric Arctic middle atmospheric circulation with variable gravity wave activity, the occurrence of stratospheric sudden warmings provide an opportunity to understand the complex wave-wave and wave-mean flow interaction occurring in the middle atmosphere. However, the characteristics of individual stratospheric warmings are vastly different. Gravity wave activity during stratospheric warming events is expected to be different depending on the type and characteristics of the warming event. Thus more direct measurements of gravity waves under different types of major mid-winter warmings are needed for a thorough understanding of the middle atmospheric circulation. Two types of warming events, vortex displacement event and vortex split event, and their dynamical differences have been discussed by *Charlton and Polvani* [2007] using NCEP-NCAR and ECMWF reanalysis data sets. By documenting the major mid-winter stratospheric warming events from 1958 to 2002, the authors find that the vortex is preconditioned before the vortex splitting event. During vortex split events the wind reversals are found be longer, stronger, and extend deeper into the lower atmosphere, and the influence of vortex split events on middle stratospheric temperatures last longer. Thus, vortex split events are expected to significantly reduce the vertical propagation of gravity waves.

In a recent study, *Thurairajah et al*. [2009a] reported Rayleigh lidar measurements of reduced gravity wave activity during the formation of an elevated stratopause that followed the stratospheric warming event of early January 2004. The January 2004 warming was a vortex displacement event where the major warming in early January led

to a two month long disruption of the mid and lower stratospheric vortex. The upper stratospheric vortex reformed into a robust, colder cyclone. After the stratosphere warmed the disruption of the vortex led to an isothermal atmosphere, and subsequently an elevated stratopause. *Thurairajah et al*. [2009a] suggested that the weak stratospheric winds associated with the warming suppressed the upward propagating gravity waves thus removing the heat source in the winter stratopause region. This region thus radiatively cooled and the stratopause reformed at higher altitudes (~80 km).

A similar meteorological situation with formation of elevated stratopause occurred after the January 2009 major mid-winter warming. A major warming with reversal of both zonal wind and temperature gradient at 10 hPa and poleward of 60^{o}N occurred on 24 January 2009 [*Manney et al*., 2009]. During this warming the polar vortex split into two making it a vortex split event. After the disruption of the vortex, the stratopause reformed at ~80 km during the first week of February and remained elevated until the first week of March 2009. In contrast to this vortex split event, four pulses of warming have been recorded during the 2007-2008 winter with maximum positive meridional temperature gradients occurring on 25 January, 2, 16, and 23 February 2008 [*Wang and Alexander*, 2009]. The fourth warming on 23 February 2008 was a major warming a vortex displacement event.

In this paper we present Rayleigh lidar measurements of gravity wave activity from Chatanika, Alaska (65^{o}N, 147^{o}W) in the 40-50 km altitude during both the 2007-2008 and 2008-2009 winters. These direct measurements provide an opportunity to study gravity waves under different types of stratospheric warming events. It also allows us to investigate the variability of gravity wave activity between winters of 2003-2004 and 2008-2009 where the major mid-winter warming resulted in an elevated stratopause. In section 4.2 we briefly describe the Rayleigh lidar technique. In section 4.3 we present lidar measurements of temperature over the 40-70 km altitude and gravity wave activity over the 40-50 km altitude at Chatanika during the 2007-2008 and 2008-2009 winters. In section 4.4 we present the meteorology of the 2007-2008 and 2008-2009 winters in the northern hemisphere in terms of the synoptic structure, evolution, and variability of the

Arctic stratospheric vortex and Aleutian anticyclone, and planetary wave activity using satellite data and meteorological data. We discuss the evolution of the vortex and anticyclone and the horizontal wind structure over Chatanika in section 4.5. In section 4.6 we compare the gravity wave activity at Chatanika with the wave activity at two other lidar sites. In section 4.7 we discuss the variability in the gravity wave measurements. We summarize this work in section 4.7.

4.2. Rayleigh Lidar Data and Analysis

Rayleigh lidars work on the principle that in the absence of aerosols the scattered light from neutral molecules in the atmosphere is directly proportional to the atmospheric density. Lidar observations yield temperature measurements of the stratosphere and mesosphere (~30-90 km) under assumptions of hydrostatic equilibrium. The temperature profiles are calculated by downward integration by assuming an initial temperature at the highest altitude. The National Institute of Information and Communications Technology (NICT) Rayleigh lidar at Poker Flat Research Range (PFRR), Chatanika, Alaska has been operated since 1997 [*Murayama et al*. 2007]. The Rayleigh lidar measurements have supported a variety of middle atmospheric studies including mesospheric inversion layers [*Cutler et al*., 2001], noctilucent clouds [*Collins et al*., 2003; *Collins et al*., 2009], temperature measurements [*Thurairajah et al*., 2009b], and gravity wave activity [*Thurairajah et al*., 2009a]. Further technical details about the Rayleigh lidar technique and data processing methods can be found in these references. The Rayleigh lidar measurements at Chatanika from October to March over the two winters (2007-2008 and 2008-2009) have yielded a total of 40 nights of measurements lasting between four and 13 hours for a total of ~324 hours of observations.

We characterize the gravity wave activity in the upper stratosphere (40-50 km) in terms of the background stability (buoyancy period, $T_B=2\pi/N$) of the atmosphere and the wave potential energy density (E_p) calculated from 30 minute resolution density data. The potential energy density is given by [e.g., *Gill*, 1982],

$$E_p = \frac{1}{2} N^2 \overline{\xi^2} = \frac{1}{2}\left(\frac{g}{N}\right)^2 \overline{\left(\frac{\rho'}{\rho_o}\right)^2} \tag{4.1}$$

where N is the buoyancy frequency, ξ is the vertical displacement of air parcel, and ρ'/ρ_o the rms relative density fluctuation. The rms relative density perturbations, the buoyancy frequency (calculated from the nightly averaged temperature profile), and the constant of acceleration due to gravity are independently averaged over the 40-50 km altitude. A detailed description of the gravity wave analysis method is given in *Thurairajah et al*. [2009b]. To reduce noise and obtain short period waves the density perturbations are spatially band-limited between vertical wavenumbers 0.5 km^{-1} and 0.1 km^{-1} (vertical altitude range of 10 km, i.e., between 40-50 km)and temporally band-limited between the Nyquist frequency of 1 h^{-1} and the low frequency of 0.25 h^{-1} (time period between 30 min and four hours).

4.3. Rayleigh Lidar Measurements

4.3.1. Temperature Measurements

In Figure 4.1 we plot individual and monthly mean profiles from late January to third week of February 2008 and February 2009. We average the individual nighttime profiles to form the mean monthly profile. We also compare the mean profile to the monthly mean February profile calculated from 19 nights of lidar measurements at Chatanika from 1997-2005 and reported by *Thurairajah et al*. [2009a], and to the zonal mean temperature climatology from the Stratospheric Processes And their Role in Climate (SPARC) reference atlas [*Randel et al*., 2004; SPARC, 2002] (Figure 4.1, right panel). We choose the profiles from late January and February 2008 and February 2009 to illustrate the response of the thermal structure of the stratosphere and mesosphere to the warmings that occurred during these two winters.

The individual profiles from 2008 indicate a general cooling in the 40-80 km altitude except the one profile from the night of 3-4 February 2008 that indicates the formation of a an elevated stratopause. This could be the result of the minor warming on 2 February 2008. The average temperature profile in 2008 is in general colder than the

Chatanika and SPARC averages, with a stratopause below 40 km. At ~50 km the average temperature is ~12 K colder than the SPARC average. The mesospheric cooling is associated with the pulses of the four warmings during January and February 2008. In February 2009 the individual profiles show less variability below ~65 km. The temperature profiles appear to show near isothermal temperatures or an elevated stratopause. The average February 2009 profile is colder than the Chatanika and SPARC averages below ~70 km and warmer above ~70 km. For example at ~50 km the average February 2009 temperature is ~17 K colder than the SPARC average.

In Figure 4.2 we plot the buoyancy period averaged over the 40-50 km altitude as a function of day during October to March of 2007-2008 and 2008-2009 at Chatanika, Alaska. During the 2007-2008 winter, the background atmosphere increased in stability (decreased in buoyancy period) from 340 s in late November 2007 to 255 s in late December 2007, and again became less stable (347 s) in late January 2008. The stability generally increased through March 2008 with an average buoyancy period of 311 s in February and 301 s in March 2008. During the 2008-2009 winter, the background atmosphere was generally stable through late January 2009 (average 293 s) after which the stability decreased (i.e. buoyancy period increased) to a high buoyancy period of 343 s in late January 2009. The atmosphere was more stable through March 2009 (but with lower than 2008 values) with an average value of 296 s in February and 294 s in March 2009.

4.3.2. Gravity Wave Activity

In Figure 4.3 we plot the nightly gravity wave activity in terms of the potential energy density averaged over 40-50 km as a function of day from October to March of 2007-2008 and 2008-2009 at Chatanika. We plot the monthly average values from the two winters in Figure 4.4 and compare them to the average potential energy measured from the 1997-2005 winters at Chatanika. We tabulate the average and range of potential energy values and buoyancy periods at Chatanika during both winters in Table 4.1. The individual potential energy densities at Chatanika exhibit a high degree of nightly

variability with the highest value of 8.6 J/kg (± 0.5) measured on the night of 19-20 November 2009 and lowest value of 0.13 J/kg (± 0.04) measured on 25-26 March 2008. The monthly averaged potential energy densities from the 2007-2008 and 2008-2009 winters exhibit a broad annual cycle with a winter maximum value of 4.1 J/kg in November and minimum value of 0.29 J/kg in April. This cycle is also observed in the monthly averaged potential energy density measured at Chatanika, Alaska from 1997-2005. The data from 1997-2005 includes 90 nights of measurements varying between four and 15 hours for a total of ~750 hours of observations. The individual values from both March 2008 and 2009 are found to be lower then the averaged March value from 1997-2005.

The potential energy density varies as a function of both the rms relative density fluctuation, ρ'/ρ_o and the buoyancy frequency, N. To investigate the effect of local stability conditions on the gravity-wave fluctuation, we plot the rms relative density fluctuation as a function of buoyancy period averaged over 40-50 km for the 2007-2008 and 2008-2009 winters at Chatanika in Figure 4.5. Linear fits to the data from each winter indicate a low correlation of 0.15 for 18 nights during the 2007-2008 winter and 0.30 for 22 nights during the 2008-2009 winter. The overall correlation coefficient for all 40 nights of data is 0.28. Since there is no significant correlation of rms relative density fluctuation with buoyancy period we conclude that the wave activity in terms of the potential energy density is not a measure of the local stability. However, we observe that during the 2008-2009 winter the rms relative density fluctuations are larger and the atmosphere more stable compared to the 2007-2008 winter. The fact that during the 2008-2009 winter the rms relative density fluctuation decreases with decreasing stability suggests that the gravity wave amplitudes are limited by internal instabilities [*Fritts and Rastogi*, 1985].

In summary, the Rayleigh lidar temperature profiles during the 2007-2008 and 2008-2009 winters are significantly different with mesospheric cooling observed after the January 2008 warming, and a tendency toward isothermal atmosphere or elevated stratopause observed after the January 2009 warming. The buoyancy period is less stable

after the warming during both winters with the 2009 values less than the 2008 values. The gravity wave activity is characterized in terms of potential energy density and we observe a high degree of nightly variability. The monthly averaged potential energy densities indicate a broad annual cycle with a winter maximum similar to the averaged potential energy density from Rayleigh lidar measurements during 1997-2005 from the same site. The individual values from March 2008 and 2009 are lower than the 1997-2005 March average.

4.4. Synoptic View and Planetary Wave Activity during the 2007-2008 and 2008-2009 Winters

The two winters of 2007-2008 and 2008-2009 were characterized by different meteorological conditions with four warming events in late January (25^{th}), early (2^{nd}), mid (16^{th}), and late (23^{rd}) February 2008 [*Wang and Alexander*, 2009], and a major warming in late-January (24^{th}) 2009. This major warming in January 2009 has been recorded as the strongest and most prolonged on record [*Manney et al*., 2009]. In this section we present an overview of the dynamic structure of the middle atmosphere in terms of the position and evolution of the polar vortex and anticyclones, gradient winds, and the planetary wave activity. The characteristics of the vortices are calculated using the United Kingdom Meteorological Office (MetO) global analyses data [*Harvey et al*., 2002]. The planetary wave activity is described in terms of the wave geopotential amplitude and Eliassen Palm (EP) flux divergence calculated from temperature, pressure, and geopotential measured by the Sounding of the Atmosphere using Broadband Emission Radiometry (SABER) instrument data (Level 2A version 1.07) [*Beaumont*, 2008] aboard the Thermosphere Ionosphere Mesosphere Energetics Dynamics (TIMED) satellite [*Mertens et al*., 2004; *Russell et al*., 1999]. The gradient winds are also calculated from the SABER data.

In Figures 4.6 and 4.7 we show examples of 3D structure of the polar vortex and anticyclone over the northern hemisphere during active and quiet times during the 2007-2008 and 2008-2009 winters. In Figures 4.8 and 4.9 we plot the geopotential amplitude of

planetary wave one and wave two, gradient winds and EP flux divergence at 65^{o}N during the 2007-2008 winter, and 2008-2009 winter respectively. The EP flux provides a measure of the zonal-forcing of the zonal-mean flow. The flux values have been scaled by the basic density to give the zonal force per unit mass exerted by eddies [*Holton*, 2004].

4.4.1. The 2007-2008 Arctic Winter

The stratospheric vortex and Aleutian anticyclone were dynamically active during the second half of January, and February 2008. In Figure 4.6 (top panel) we show the 3-D structure of the stratospheric vortex and anticyclones on 25 December 2007 and 15 January 2008. There is a high degree of interaction between the traveling anticyclones and the stratospheric vortex, with the vortex beginning to elongate and move off pole center on 15 January 2008. Four pulses of warming events have been recorded during this time with the fourth warming recorded as a major warming event. Figure 4.6 (mid and lower panel) shows the structure of the vortex and anticyclones on 23 January 2008, 4, 15, and 22 February 2008 when large planetary wave-one amplitudes are observed in the SABER data. The Aleutian high strengthened, thus displacing the vortex toward the North Atlantic during the first three events, while the stronger anticyclone, weakened and distorted the vortex during the last event leading to a major stratospheric warming.

The planetary wave analysis (Figure 4.8 left panel) indicates the four periods of strong planetary wave-one amplitudes with maximum amplitudes on 23 January 2008, 4, 15, and 22 2008. The amplitudes vary between 1800 m and 2600 m at altitudes between 6.3 (~44 km) and 9.5 (~66 km) scaled heights. There are also four periods of large wave-two amplitudes during the same time period (with maximum amplitudes on 24 January 2008, 2, 20, and 27 February 2008) with geopotential amplitudes varying from 700 m and 800 m between altitudes of 6.9 (~48 km) and 8.6 (~60 km) scaled heights. Weakening and reversal of the gradient winds and convergence of EP flux is observed (Figure 4.8 right panel) during increases in planetary wave amplitudes. During the major warming in late February 2008, the winds reversed to a maximum of -34.6 m/s (negative implies

easterly winds) at 6 (~42km) scale heights. The maximum reversals were on 23 January 2008, the same day as the maximum planetary wave-one amplitude, and on 7, 17, and 24 February 2008, a few days later than the maximum planetary wave-one amplitudes.

Large values of EP flux divergence preceded the maximum values of easterly winds, except during the first warming. Maximum values were recorded on 23 January, 4, 14, and 22 February 2008. The maximum flux values varied between -171.6 m/s/day to -135.6 m/s/day at 6 (~42km) scale heights. The flux convergence (i.e. negative EP flux divergence) is a measure of the westward zonal force exerted by eddies on the atmosphere and is linked to the entwining of the upper stratospheric vortex around the Aleutian anticyclone on 22 February 2008 in Figure 4.6. After the late February major warming, the mid and lower stratospheric vortex remained weak and quasi stationary until the final warming in March 2008 (not shown).

4.4.2. The 2008-2009 Arctic Winter

During the 2008-2009 winter a major stratospheric warming occurred during the third week of January 2009 when the Aleutian high strengthened and split the vortex into two. In Figure 4.7 (top panel) we show the pole centered, undisturbed polar vortex on 25 December 2008 and 5 January 2009. The vortex first split in the upper stratosphere on 19 January, continued to split downward to the mid stratosphere (800 K) on 21 January, and was split through the entire stratosphere by the 24 January (Figure 4.7 lower left panel). The vortex remained split for almost three weeks until ~6 February (Figure 4.7, lower left panel) when the upper stratospheric vortex recovered with colder temperatures. During the major warming, planetary wave analysis at 65^{o}N shows large planetary wave two geopotential amplitude of 1400 m at altitude of 5.9 (~41 km) scaled height on 19 January 2009 (Figure 4.9 left panel). Maximum planetary wave one amplitude of 1200 m and 1000m at higher altitude of 8.1 (~57 km) and 9.6 (~67 km) scaled height are also observed on 21 January and 10 February 2009.

A stronger and deeper wind reversal extending from the mesosphere to the lower stratosphere in mid January 2009 is seen in Figure 4.9 (right panel). The wind reversed to

a maximum of -53.8 m/s at scale height of 8 (~49 km) on 23 January 2009 two days after the maximum planetary wave-one amplitude was observed. Such wind reversals in the mesosphere (also seen during the 2008 warming events) have been reported previously [*Hoffman et al*., 2007 and references therein] and show the downward progression of disturbances to the middle atmospheric circulation from the mesosphere/lower thermosphere to the stratosphere. The altitude extent of the reversal from the mesosphere to the lower stratosphere has been noted by *Charlton and Polvani* [2007] as a feature of a vortex split warming events that is not observed in vortex displacement events (as observed in February 2008). The maximum EP flux convergence of -137.6 m/s/day at 6.0 scale heights (~42 km) occurred on 20 January 2009, three days before the maximum wind reversal was observed. This large EP flux convergence indicates the westward zonal force exerted by eddies on the atmosphere.

By the second week of February the upper stratospheric vortex had completely recovered (Figure 4.7 lower right panel) and strengthened while the mid and lower stratospheric vortex remained weak. The temperature inside the vortex was anomalously cold and led to the formation of an elevated stratopause in February 2009. The lower stratospheric vortex remained weak until late March 2009.

4.5. The 2007-2008 and 2008-2009 Winters at Chatanika

In this section we document the temporal evolution of the stratospheric vortex and anticyclone over Chatanika during the 2007-2008 and 2008-2009 winters. We analyze the variability of the horizontal winds from year to year at a single site, and between different locations. In Figure 4.10 we plot the temporal evolution the stratospheric vortex (green) and anticyclone (red) from 400 K to 2000 K (~15-47 km) altitude region during the 2007-2008 and 2008-2009 winters. In Figure 4.11 we show the polar plot (30^o N-90^o N) of the vortex, anticyclone, and horizontal wind at 800 K (~30 km, ~10 hPa). These winds are calculated from the MetO global analyses data by combining the zonal, u, and meridional, v, wind ($\sqrt{u^2 + v^2}$).

Distinct differences exist in the temporal evolution of the stratospheric vortex and anticyclone over the two winters. During the 2007-2008 winter the Aleutian anticyclone is dominant over Chatanika in January and February when the planetary wave activity is the strongest. At 800 K the Aleutian anticyclone grows in size over Chatanika while sampling the anticyclones edge on 22 January and inside the anticyclone on 22 February 2008. The horizontal winds decrease from 32.3 m/s to 14.2 m/s. The major stratospheric warming during the third week of February disrupts the vortex. The upper stratospheric vortex reappears over Chatanika in early March 2008.

During the 2008-2009 winter the major stratospheric warming during the third week of January is evident as the presence of a dominant anticyclone at Chatanika (Figure 4.10 lower panel). At 800 K the split vortex with two anticyclones is seen on 22 January 2009 (Figure 4.11). The anticyclone is over Chatanika with a wind speed of 24.5 m/s. After the major warming the upper stratospheric vortex strengthens followed by the mid stratospheric vortex. The upper and mid-stratospheric vortices reappear over Chatanika with reduced wind speeds, while the lower stratospheric vortex remains disrupted. For example, on 22 February 2009 the 800 K (mid stratospheric vortex) winds are reduced to 5.9 m/s at Chatanika when the vortex is present overhead. By early March 2009 the vortex appears at all stratospheric altitudes.

In Figure 4.12 we compare the daily horizontal wind at 800 K isentropic surface above Chatanika during the 2007-2008 and 2008-2009 winters with the 2003-2004 winter. The decrease in winds in the second week of January 2008 and third week of January 2009 coincide with the strengthening of the Aleutian anticyclone and occurrence of stratospheric warmings. The 800 K horizontal wind speed on 15 January 2008 was 25.1 m/s, 3 times less than the wind speed on 15th January 2009 (73.3 m/s). The wind increased to 45.6 m/s on 21 January 2008 while it decreased to 19.3 m/s on 21 January 2009 during the major warming. While the winds in both 2008 and 2009 continued to decrease following the January warming event until mid March 2009, the 2008 winds increased and decreased periodically between each warming event.

In summary, distinct differences exist in the temporal evolution of the stratospheric vortex and anticyclones during the 2007-2008 and 2008-2009 winters. Over Chatanika the stratospheric warming events during the 2007-2008 and 2008-2009 winters are observed as growth of the anticyclone over Chatanika. The daily winds indicate a decrease in wind speed prior to the peak of the stratospheric warming. The reduced monthly averaged horizontal wind speeds in February also indicate the disruption of the stratospheric circulation during and after the stratospheric warming of 2008 and 2009.

4.6. Comparison of Gravity Wave Activity at Chatanika with Kühlungsborn and Kangerlussuaq

In this section we analyze the geographical variability in gravity wave activity during the 2007-2008 warming event using Rayleigh lidar measurements from Chatanika, Alaska (65°N, 147°W), Kühlungsborn, Germany (54°N, 12°E), and Kangerlussuaq, Greenland (67°N, 51°W). We process the data available from January and February 2008 at Kangerlussuaq and Kühlungsborn, and October and March of 2009 at Kühlungsborn, uniformly to avoid biases due to data processing methods.

During January and February 2008 the background atmosphere was stable at all three locations with average values of 317 s, 321 s, and 302 s. The potential energy densities were lower at Chatanika with an average value of 1.5 J/kg (± 0.3), and higher at Kangerlussuaq with a value of 4.7 J/kg (± 1.1). The average potential energy density at Kühlungsborn (2.6 J/kg ± 0.6) is between the high average value at Kangerlussuaq and low average value at Chatanika. During the 2008-2009 winter the background atmosphere is stable at both Chatanika and Kühlungsborn. The potential energy values at Kühlungsborn in October 2009 (average, 2.2 J/kg ± 0.6) are higher than at Chatanika (average, 1.7 J/kg ± 0.5). The potential energy values at Kühlungsborn in March 2009 (average, 1.0 J/kg ± 0.2) are similar to the Chatanika (average, 1.2 J/kg ± 0.3) March 2009 values.

From the SABER data analysis, we observe the same pulses of four warmings during the 2007-2008 winter and the major warming in January 2009 at 55^{o}N and 75^{o}N.

We observe similar tendencies in planetary wave activity, wind reversals, and zonal forcing by eddies as seen at 65^{o}N, but with stronger poleward activity. However, distinct differences exist in the temporal evolution of the stratospheric vortex and anticyclone at the three sites and over the two winters. Chatanika was generally under the influence of the Aleutian anticyclone, Kangerlussuaq under the vortex and Kühlungsborn in and out of the vortex. The difference in wind speeds associated with the movement of the vortex and Aleutian anticyclone is apparent from Figure 4.11. At 800 K the Aleutian anticyclone grows in size over Chatanika while sampling the anticyclones edge on 22 January and inside the anticyclone on 22 February 2008. The horizontal winds decrease from 32.3 m/s to 14.2 m/s. On these two days the vortex is over Kühlungsborn and Kangerlussuaq with wind speeds decreasing from 61.8 m/s to 23.9m/s at Kühlungsborn, and staying almost constant at 37.1 m/s and 42.3 m/s at Kangerlussuaq as the vortex moves overhead. We find a positive correlation between wind speed and wave potential energy density at all three sites. The correlation is, however, higher at Kühlungsborn and Kangerlussuaq compared to Chatanika.

4.7. Variability in Gravity Wave Activity

4.7.1. Variability in Gravity Wave during the 2007-2008 and 2008-2009 Winters

To understand the effect of the horizontal wind speed on the gravity wave activity in the upper stratosphere we plot the correlation between wind speed and potential energy density in Figure 4.13. We calculate the correlation at Chatanika for observations after the first warming in January 2008 and after the major warming in January 2009 until the end of February. During the 2007-2008 winter for nine nights of measurements the correlation is highest at 800 K (~30 km) with a low correlation coefficient of 0.38. We remove the outlier point of 1.9 J/kg at ~36 m/s to obtain a correlation coefficient of 0.50. This potential energy value is that observed on 3rd February 2008, the one 'anomalous' temperature profile discussed in section 3. During the 2008-2009 winter the correlation is greater than 0.80 from 550 K (~22 km) to 900 K (~30 km) with maximum correlation of 0.95 at 800 K. This suggest that while there is very little correlation between the nightly

variability of the gravity wave activity in the upper stratosphere and the variation of the mean wind speed in the mid-stratosphere in 2007-2008, about 90% ($r^2 = 0.90$) of the nightly variability of the gravity wave activity in the upper stratosphere is related to the variation of the mean wind speed in the mid and upper stratosphere in 2008-2009.

After the January stratospheric warmings, while the correlations between the wind speed in the mid-stratosphere and gravity wave activity in the upper stratosphere are different during the two winters, the magnitude of the average gravity wave activity remains similar. The average value from the first major warming to the end of February in 2008 and 2009 are 1.5 J/kg (± 0.3) and 1.6 J/ kg (± 0.4), respectively. This suggests that while the gravity waves during the 2008-2009 winter were modulated by mid-stratospheric wind speeds, some other physical process like variable wave source intensity or in-situ generation of gravity waves for example by 'spontaneous imbalance' (unbalanced flows are restored to a balanced state [*Wang and Alexander*, 2009]) could explain the variability in gravity wave energy during the 2007-2008 winter.

We also observe a broad annual cycle in the monthly averaged potential energy densities from the 2007-2008 and 2008-2009 winters. Such an annual variation in gravity wave activity with a maximum in winter and minimum in summer have been reported at both high and mid-latitudes. For example, *Eckermann et al*. [1994] used rocket measurements of temperature and winds from 20-60 km and found that variances in horizontal wind associated with gravity wave fluctuations were at a minimum in summer and peaked during winter at latitudes ~50^{o}N – 80^{o}N. An annual cycle in gravity wave activity has also been reported at the mid-latitudes sites of Observatoire de Haute Provence (OHP, 44^{o}N, 6^{o}E) and the Centre d'Essais des Lands at Biscarosse (BIS, 44^{o}N, 1^{o}W) in France using Rayleigh lidar measurements between 30-75 km by *Wilson et al*. [1991] and at the Syowa Station (69^{o}S, 39.6^{o}E) in Antarctica using radiosonde measurements between 15-25 km by *Yoshiki et al*. [2004]. An annual increase in gravity wave activity over the 30-35 km in late-December has also been reported by *Duck et al*. [1998] between 1992-1993 and 1996-1997 using Rayleigh lidar measurements. The

authors attribute this increase to the movement of the vortex jet over the lidar site at Eureka, Canada (80°N, 86°W).

4.7.2. Comparison of Gravity Wave Activity during the 2008-2009 Winter with the 2003-2004 Winter

The effect of the early January 2004 major mid-winter warming on the stratospheric circulation [*Manney et al*., 2008] is similar to that of the January 2009 warming. The disruption of the vortex after the major warming, the recovery of the colder, robust upper stratospheric vortex, and the reformation of the stratopause at higher altitudes occurred during both the January 2004 and 2009 major warming. The type of warming was different, with the January 2004 warming being a vortex displacement event and the January 2009 warming being a vortex split event. To analyze the differences (if any) in gravity wave activity during the two warmings we compare the synoptic structure of the vortex, anticyclone, planetary wave activity and gravity wave activity during the two winters.

After the major warming in early January 2004, the planetary wave activity during the 2003-2004 winter had repeated periods of large wave one and wave two amplitudes in the upper stratosphere and mesosphere between mid-February and January 2004. The EP flux divergence was negative throughout the period from mid-January through early March 2004. In contrast, there is only one period of large planetary wave one and wave two amplitudes, and negative EP flux divergence during the major warming in the third week of January 2009. The temporal evolution of the stratospheric vortex and anticyclone was also different. In contrast to the 2008-2009 winter the Aleutian anticyclone was over Chatanika at all stratospheric heights for a longer time during the 2003-2004 warming, and the vortex never appeared below 800 K after the warming. Since the 2004 warming occurred in early January the horizontal winds decreased earlier (second half of December 2003) and remained low through the rest of the winter, while the winds decreased only during the third week of January 2009.

Thurairajah et al. [2009a] have reported the reduced gravity wave activity at Chatanika during the 2003-2004 winter compared to the 2002-2003 and 2004-2005 winters. For comparison between the two warmings we average the potential energy density and horizontal wind speed from the day of the initial wind reversal until the end of February. We average the wind speeds only on the days were lidar data is available. This average potential energy was lower with a value of 0.72 J/kg (±0.1) in 2004 compared to the value of 1.6 J/kg (±0.4) in 2009. The average horizontal wind speeds at 1600 K (~44 km, ~1 hPa) was higher in 2004 with a value of 41.2 m/s compared to 2009 value of 29.8 m/s, but at 800 K (~30 km, ~10 hPa) and 500 K (~19 km, ~60 hPa) the average horizontal wind speed was lower in 2004 (10.1 m/s; 8.7 m/s) compared to 2009 (15.9 m/s; 13.5 m/s). This suggests that the lower winds in the mid- and lower stratosphere in 2004 critically filtered more gravity waves in 2004 compared to 2009.

Manney et al. [2005] and *Manney et al*. [2009] have documented both the major-mid winter warmings in January 2004 and January 2009. The authors report that both the warmings were unpredicented at their time in terms of the effect on the lower stratosphere and the duration of the warming; the January 2009 warming has been documented as the strongest and longer lasting on record. Our analysis shows that while the response of the synoptic vortex and thermal structure of the middle atmosphere to the 2004 and 2009 warmings were similar, the 2004 warming had a stronger influence on the gravity wave activity at Chatanika in the 40-50 km altitude.

4.7.3. Geographic Variability in Gravity Wave Activity

In a recent satellite study of gravity wave activity during the 2007-2008 stratospheric sudden warming, *Wang and Alexander* [2009] have reported a zonal asymmetry in gravity wave amplitudes with reduced gravity wave transmission over the North Pacific. Their analysis indicated larger gravity wave amplitude near the polar vortex edge. Our measurements of gravity wave potential energy density at the three sites of Chatanika, Kühlungsborn, and Kangerlussuaq indicate a similar geographical variability with higher potential energy density at Kühlungsborn and Kangerlussuaq

where the vortex is overhead, and lower values at Chatanika where the Aleutian high is overhead. The larger positive correlation of potential energy density with horizontal wind speeds at Kühlungsborn and Kangerlussuaq is consistent with the theory of selective transmission of gravity waves [*Dunkerton and Butchart*, 1984] where higher gravity wave activity is associated with the stronger wind speeds in the vortex jet. But the lower correlation of potential energy density with horizontal wind speeds at Chatanika is not consistent with the selective transmission theory where weak winds in the Aleutian high system over the western Arctic would filter the stratospheric gravity waves propagating into the mesosphere.

A longitudinal variability in gravity wave activity has also been reported by *Chandran et al*. [2009] from gravity wave signatures detected on Polar Mesospheric Clouds (PMC). The authors report a concentration of gravity wave activity over North West Greenland, eastern Canada, and over the Arctic Ocean north of Central Siberia. This longitudinal variation and the fact that horizontal winds are not modulating the gravity wave activity at Chatanika during the 2007-2008 winter emphasize the role of gravity wave sources in changing the vertical propagation of gravity waves.

4.8. Conclusion

We have used Rayleigh lidar data from Chatanika, Alaska (65°N, 147°W) to characterize the gravity activity in the upper stratosphere and lower mesosphere (40-50 km) during the winters of 2007-2008 and 2008-2009. The two winters were different with four stratospheric warming events during late January and late February 2008, and one warming in late January 2009. The 2008 fourth warming event was a vortex displacement event and the 2009 warming a vortex split event. We find a large nightly variability in gravity wave potential energy density during the two winters. The monthly average potential energy density exhibits a broad annual cycle with winter maximum and summer minimum. We find lower gravity wave activity at Chatanika compared to the wave activity in Kühlungsborn and Kangerlussuaq. We attribute this geographic variability to the selective transmission of gravity waves by the varying background winds. The wave

potential energy densities and horizontal wind speeds are positively correlated during both winters and at all three sites, albeit with lower correlation at Chatanika during the 2007-2008 winter compared to the 2008-2009 winter, and compared to Kühlungsborn and Kangerlussuaq.

We do not observe any systematic differences in gravity wave potential energy between the vortex displacement stratospheric warming of 2008 and the vortex split stratospheric warming of 2009. The different correlations of the potential energy density with horizontal wind speeds indicates that while the gravity waves are modulated by winds during the January 2009 warming, a mix of physical processes with different wave sources modulate the gravity wave activity during the 2008 warming.

Although the response of the synoptic and thermal structure of the middle atmosphere to both the 2008-2009 warming and the 2003-2004 warming was similar we observe a higher wave activity over Chatanika after the 2009 warming compared to the 2004 warming. In general the variability in temporal winds associated with each stratospheric warming appears to influence the gravity wave variability at a particular location. A network of gravity wave measurements around the Arctic could give us more insight into the global variability of gravity wave activity with height during different types of stratospheric warming events.

Acknowledgments The authors thank the staff at Poker Flat Research Range for their ongoing support of the lidar program. The authors thank Agatha Light and Brita Irving for their assistance in making the 2007-2008 and 2008-2009 lidar observations at Chatanika. The authors acknowledge the SABER science and data processing teams for providing the SABER data presented in the paper. The authors acknowledge support from the United States National Science Foundation under grants ARC 0632387 and ATM 0640340. PFRR is a rocket range operated by Geophysical Institute-University of Alaska Fairbanks with support from the United States National Aeronautic and Space Administration.

References

Beaumont, K. (2008), SABER: Sounding of the atmosphere using broadband emission radiometry, http://saber.gats-inc.com/, accessed 2008.

Chandran, A., D. W. Rusch, S. E. Palo, G. E. Thomas, and M. J. Taylor (2009), Gravity wave observations in the summertime polar mesosphere from the Cloud Imaging and Particle Size (CIPS) experiment on the AIM spacecraft, *J. Atmos. Sol. Terr. Phys*., *71*, 393-400, doi:10.1016/j.jastp.2008.09.041.

Charlton, A. L., and L. M. Polvani (2007), A new look at stratospheric sudden warmings. Part 1: Climatology and modeling benchmarks, *J. Clim.*, *20*, 449 - 469.

Collins R. L., M. C. Kelley, M. J. Nicolls, C. Ramos, T. Hou, T. E. Stern, K. Mizutani and T. Itabe (2003), Simultaneous lidar observations of a noctilucent cloud and an internal wave in the polar mesosphere, *J. Geophys. Res., 108*(D8), 8435, doi:10.1029/2002JD002427.

Collins, R. L., M. J. Taylor, K. Nielsen, K. Mizutani, Y. Murayama, K. Sakanoi, M. T. DeLand (2009), Noctilucent cloud in the western Arctic in 2005: Simultaneous lidar and camera observations and analysis, *J. Atmos. Sol. Terr. Phys*., *71*, 446-452, doi:10.1016/j.jastp.2008.09.044.

Cutler L. J., R. L. Collins, K. Mizutani, and T. Itabe (2001), Rayleigh lidar observations of mesospheric inversion layers at Poker Flat, Alaska (65 °N, 147° W), *Geophys. Res. Lett.*, *28*(8), 1467-1470.

Duck, T. J., J. A. Whiteway, and A. I. Carswell (1998), Lidar observations of gravity wave activity and Arctic stratospheric vortex core warming, *Geophys. Res. Lett*., *25* (13), 2813-2816.

Dunkerton, T. J., and N. Butchart (1984), Propagation and selective transmission in internal gravity waves in a sudden warming, *J. Atmos. Sci.*, *41*(8), 1443-1460.

Eckermann, S. D., I. Hirota, and W. K. Hocking (1994), Gravity wave and equatorial wave morphology of the stratosphere derived from long-term rocket soundings, *Q. J. R. Meteorol. Soc*., *121*, 149-186.

Fricke-Begemann, C., and J. Höffner (2005), Temperature tides and waves near the mesopause from lidar observations at two latitudes, *J. Geophys. Res*, *110*, D19103, doi:10.1029/2005JD005770.

Fritts, D. C., and M. J. Alexander (2003), Gravity wave dynamics and effects in the middle atmosphere, *Rev. Geophys*., *41* (1), 1003, doi:10.1029/2001RG000106.

Fritts, D. C., and P. K. Rastogi (1985), Convective and dynamical instabilities due to gravity wave motions in the lower and middle atmosphere: Theory and observations, *Radio Sci.*, 20, 1247-1277.

Gill, H. E. (1982), *Atmosphere - ocean dynamics*, 662 pp., Academic Press Inc., New York.

Harvey V. L., R. B. Pierce, T. D. Fairlie, and M. H. Hitchman (2002), A climatology of stratospheric polar vortices and anticyclones, *J. Geophys. Res., 107*(D20), 4442, doi:10.1029/2001JD001471.

Hoffmann, P., W. Singer, D. Keuer, W.K. Hocking, M. Kunze, Y. Murayama (2007), Latitudinal and longitudinal variability of mesospheric winds and temperatures during stratospheric warming events, *J. Atmos. Sol. Terr. Phys*., *69*, 2355–2366.

Holton, J. R. (2004), *An introduction to dynamic meteorology*, 535 pp., Elsevier Academic Press, Massachusetts, USA.

Holton, J. R., and M. J. Alexander (2000), The role of waves in the transport circulation of the middle atmosphere, in *Atmospheric Science Across the Stratopause*, *Geophys*. *Monogr*. *Ser*., vol. 123, edited by D. E. Siskind, S. D. Eckermann, and M. E. Summers, pp. 21-35, AGU, Washington, D. C.

Houghton, J. T. (1978), The stratosphere and mesosphere, *Quart. J. Royal Met. Soc*., *104*, 1-29.

Liu, H.-L., D. R. Marsh, C.-Y. She, Q. Wu, and J. Xu (2009), Momentum balance and gravity wave forcing in the mesosphere and lower thermosphere, *Geophys. Res. Lett.*, 36, L07805, doi:10.1029/2009GL037252.

Manney, G. L., K. Kruger, J. L. Sabutis, S. A. Sena, and S. Pawson (2005), The remarkable 2003-2004 winter and other recent winters in the Arctic stratosphere since the late 1990s, *J. Geophys. Res.*, *110*, D04107, doi:10.1029/2004JD005367.

Manney, G. L., W. H. Daffer, K. B. Strawbridge, K. A. Walker, C. D. Boone, P. F. Bernath, T. Kerzenmacher, M. J. Schwartz, K. Strong, R. J. Sica, K. Kruger, H. C. Pumphrey, L. Froidevaux, A. Lambert, M. L. Santee, N.J. Livesey, E. E. Remsberg, M. G. Mlynczak, and J. R. Russell III (2008), The high Arctic in extreme winters: vortex, temperature, and MLS and ACE-FTS trace gas evolution, *Atmos. Chem. Phys.*, *8*, 505-522.

Manney, G. L., M. J. Schwartz, K. Krüger, M. L. Santee, S. Pawson, J. N. Lee, W. H. Daffer, R. A. Fuller, and N. J. Livesey (2009), Aura Microwave Limb Sounder observations of dynamics and transport during the record-breaking 2009 Arctic stratospheric major warming, *Geophys. Res. Lett.*, *36*, L12815, doi:10.1029/2009GL038586.

Mertens, C. J., F. J. Schmidlin, R. A. Goldberg, E. E. Remsberg, W. D. Pesnell, J. M. Russell III, M. G. Mlynczak, M. Lopez-Puertas, P. P. Wintersteiner, R. H. Picard, J. R. Winick, and L. L. Gordley (2004), SABER observations of mesospheric temperatures and comparisons with falling sphere measurements taken during the 2002 summer MaCWAVE campaign, *Geophys. Res. Lett.*, *31*(3), L03105, doi:10.1029/2003GL018605.

Murayama, Y., M. Ishii, M. Kubota, M. Hirotaka, K. Mizutani, S. Ochiai, Y. Kasai, S. Kawamaura, Y. Tanaka, H. Masuko, T. Iguchi, H. Kumagai, T. Kikuchi, K. Sata, R. L. Collins, B. J. Watkins, M. Conde, W. B. Bristow, and R. W. Smith (2007), Comprehensive Arctic atmosphere observing system and observed results for system performance demonstration, *J. Nat. Instit. Info. Comms. Tech*, *54*(1/2), 5-16.

Pancheva, D., Mukhtarov, and B. Andonov (2009), Nonmigrating tidal activity related to the sudden stratospheric warming in the Arctic winter of 2003/2004, *Ann. Geophys.*, *27*, 975–987.

Randel, W., P. Udelhofen, E. Fleming, M. Geller, M. Gelman, K. Hamilton, D. Karoly, D. Ortland, S. Pawson, R. Swinbank, F. Wu, M. Baldwin, M.-L. Chanin, P. Keckhut, K. Labitzke, E. Remsberg, A. Simmons, and D. Wu (2004), The SPARC intercomparison of middle- atmosphere climatologies, *J. Climate*, *17*(5), 986-1003.

Russell, J. M. III, M. G. Mlynczak, L. L. Gordley, J. Tansock, and R. Esplin (1999), An overview of the SABER experiment and preliminary calibration results, *Proceedings of the SPIE*, 44th Annual Meeting, Denver, Colorado, July 18-23, 3756, 277-288.

SPARC, 2002: *SPARC intercomparison of middle atmosphere climatologies*, SPARC Rep. 3, 96 pp., 2002.

Thurairajah, B., R. L. Collins, V. L. Harvey, R. S. Lieberman, K. Mizutani (2009a), Rayleigh lidar observations of reduced gravity wave activity during the formation of an elevated stratopause in 2004 at Chatanika, Alaska (65°N, 147°W), *submitted to J. Geophys. Res.,* 2009JD013036.

Thurairajah, B., R. L. Collins, and K. Mizutani (2009b), Multi-Year temperature measurements of the middle atmosphere at Chatanika, Alaska (65°N, 147°W), *Earth Planets Space*, *61*, 755-764.

Wang, L., and M. J. Alexander (2009), Gravity wave activity during stratospheric sudden warmings in the 2007–2008 Northern Hemisphere winter, *J. Geophys. Res.*, 114, D18108, doi:10.1029/2009JD011867.

Wilson, R., M. L. Chanin, and A. Hauchecorne (1991), Gravity waves in the middle atmosphere observed by Rayleigh lidar 2. Climatology, *J. Geophy. Res., 96*(D3), 5169-5183.

Yoshiki, M., N. Kizu, and K. Sato (2004), Energy enhancements of gravity waves in the Antarctic lower stratosphere associated with variations in the polar vortex and tropospheric disturbances, *J. Geophys. Res.*, *109*, D23104, doi:10.1029/2004JD004870

Table 4.1. Buoyancy period and potential energy density at Chatanika, Alaska (65°N, 147°W) averaged over the 40-50 km altitude from October to March of 2007-2008 and 2008-2009

	2007-2008	2008-2009
Number of Observations	18	22
Buoyancy Period (s) [a]		
Average [b]	307	298
Range [c]	255 - 347	270 - 343
Potential Energy Density (J/kg) [d]		
Average	1.4 (± 0.2)	2.5 (± 0.4)
Range	0.13 – 3.0	0.40 – 8.6

[a] Calculated from nightly average temperature profile.

[b] Mean value and uncertainty in mean

[c] Minimum value and maximum value

[d] Fluctuations over 2 – 10 km and 0.5 – 4 h.

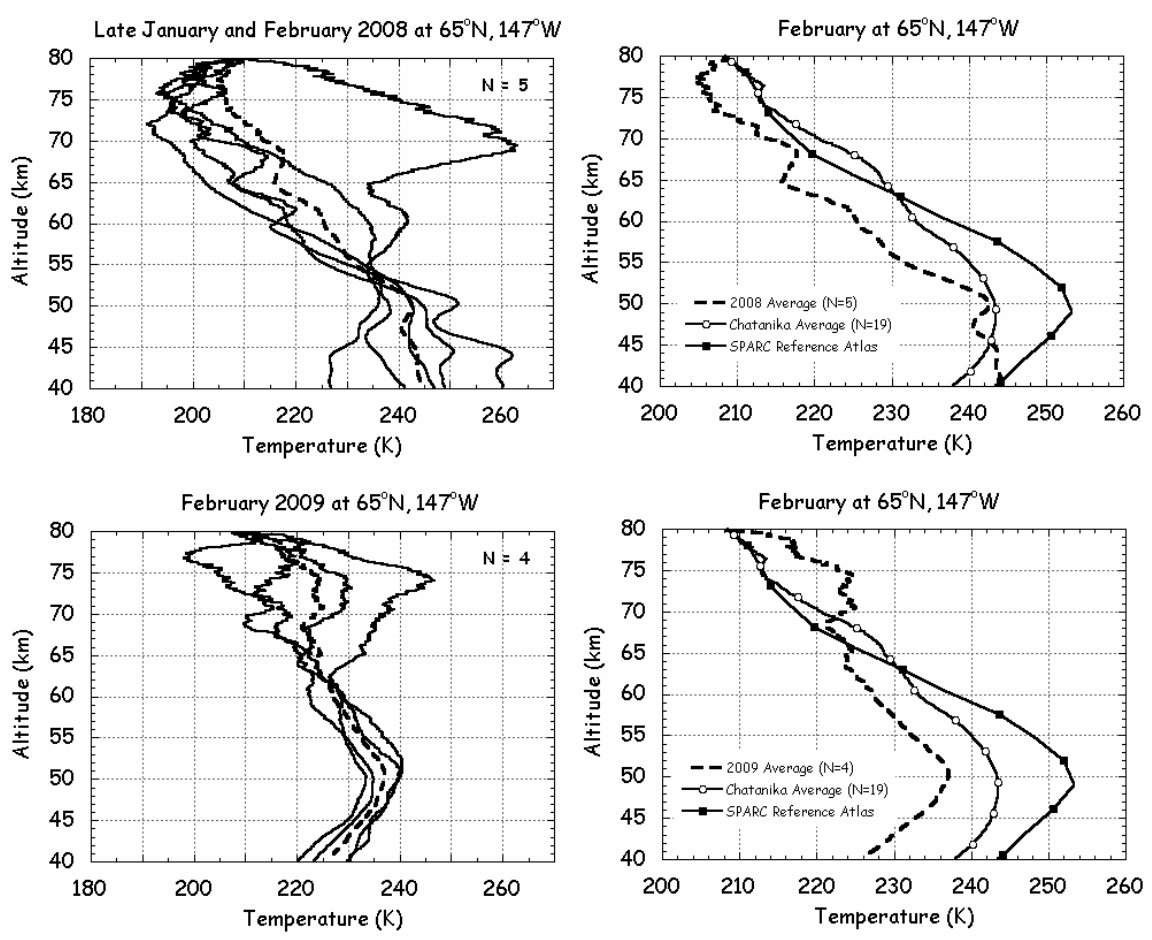

Figure 4.1. (Left) Nightly mean temperature profiles (solid line) measured by Rayleigh lidar during late January 2008 (24^{th}, 26^{th}), February 2008 (3^{rd}, 8^{th}, 10^{th}), and February 2009 (2^{nd}, 10^{th}, 17^{th}, 23^{rd}). The mean profile is plotted as a dashed line. 'N' is number of nighttime profiles for each month. (Right) The mean monthly temperatures at Chatanika averaged over late January 2008 and February 2008, and February 2009 (dashed line), averaged over February 1998-2005 (solid line with circle), and SPARC February zonal mean temperature (solid line with filled square)

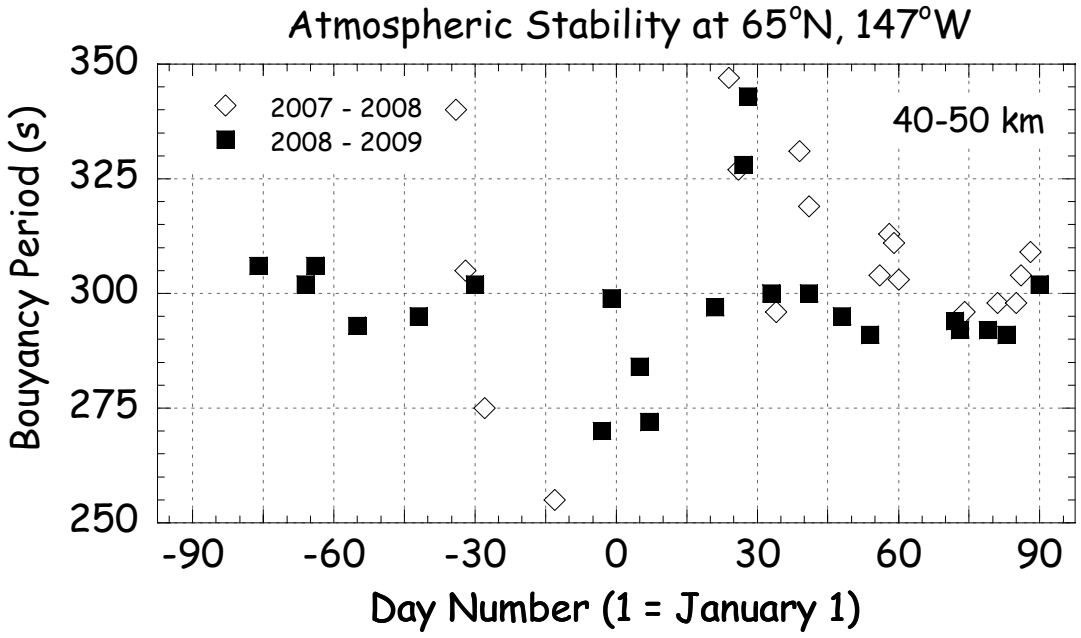

Figure 4.2. Atmospheric stability measured by Rayleigh lidar at Chatanika, Alaska (65°N, 147°W) during the 2007-2008 and 2008-2009 winters averaged over 40-50 km altitude range.

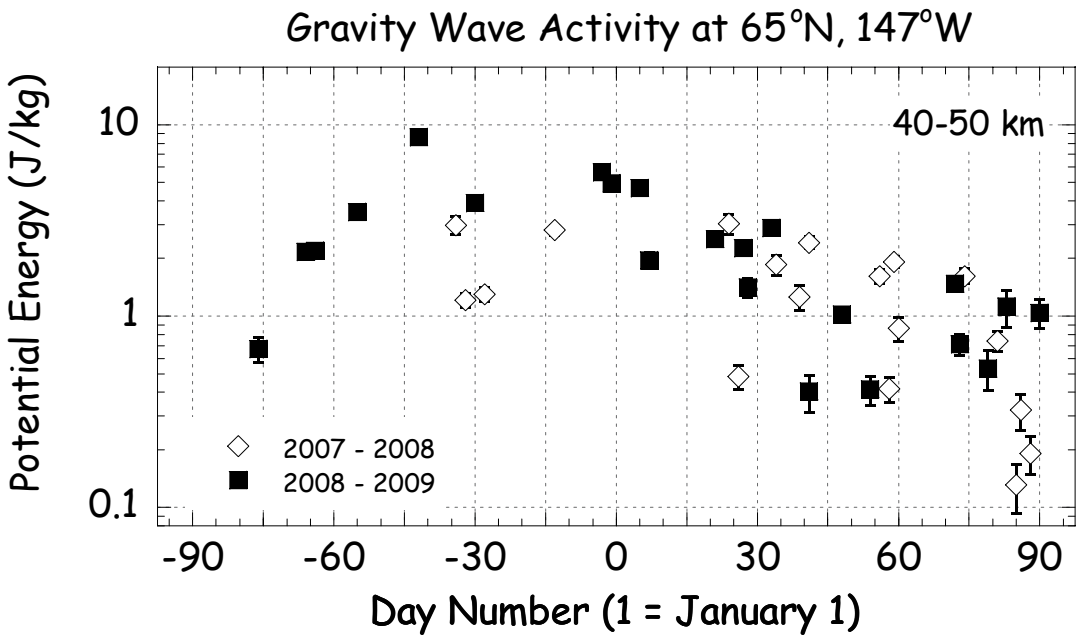

Figure 4.3. Potential energy density measured by Rayleigh lidar at Chatanika, Alaska during 2007-2008 and 2008-2009 winters averaged over 40-50 km altitude range.

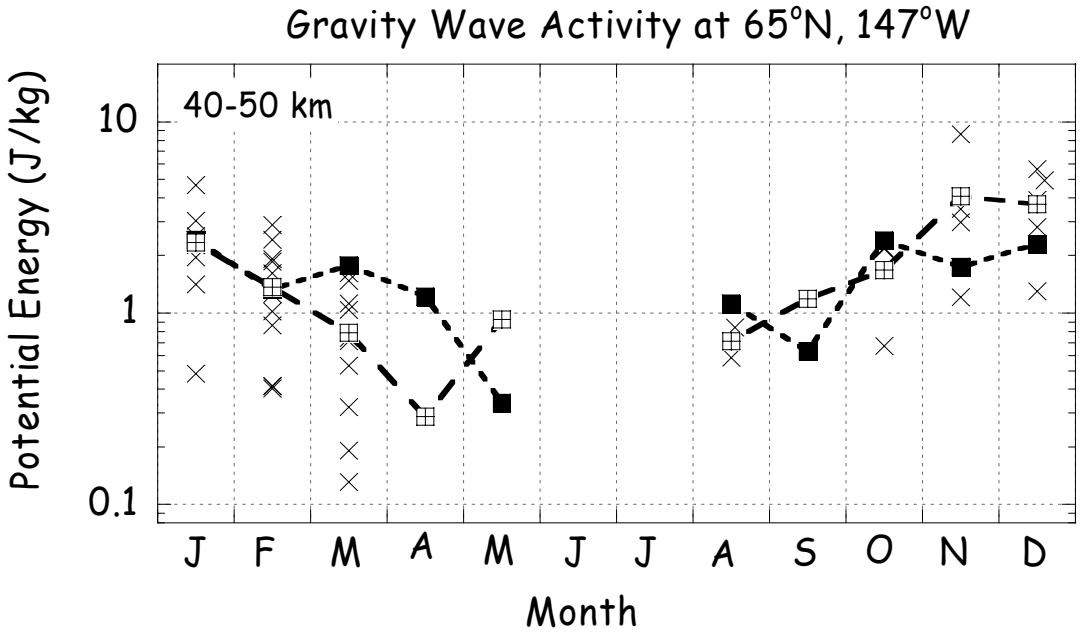

Figure 4.4. Monthly variation of potential energy density at Chatanika, Alaska (65°N, 147°W) averaged over the 40-50 km altitude. Individual nighttime values are from the 2007-2008 and 2008-2009 winters (×), monthly averaged value is from the 1997-2005 winters (dashed line with closed square) and 2007-2009 winters (dashed line with crossed square).

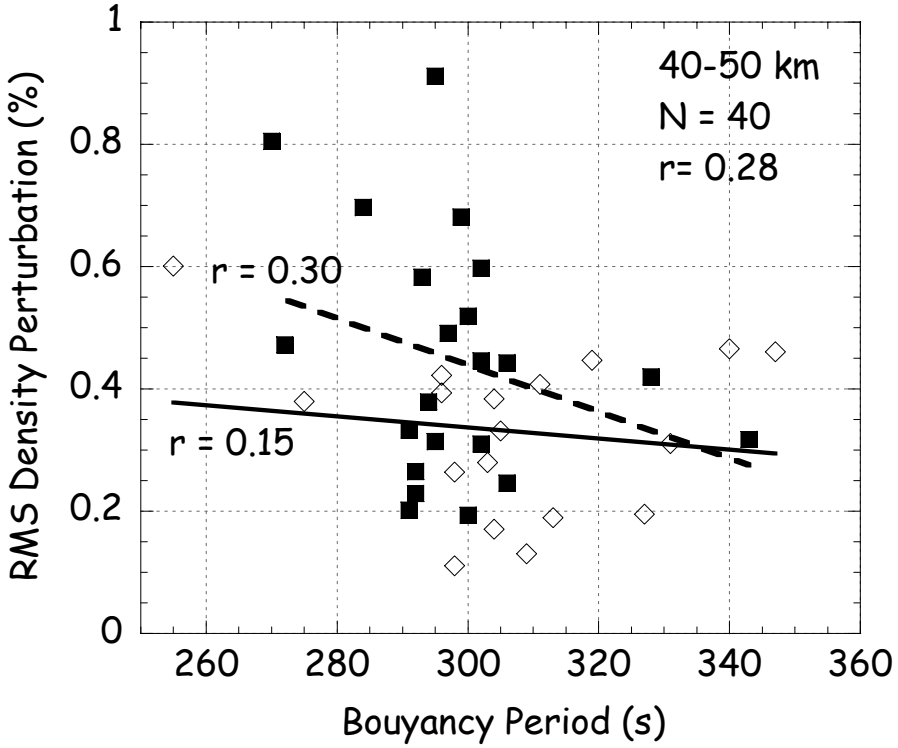

Figure 4.5. Variation of rms density fluctuation as a function of buoyancy period during October to March of 2007-2008 and 2008-2009 at Chatanika, Alaska averaged over 40-50 km altitude range. The overall correlation coefficient is given as well as the linear fit and correlation coefficient for each winter.

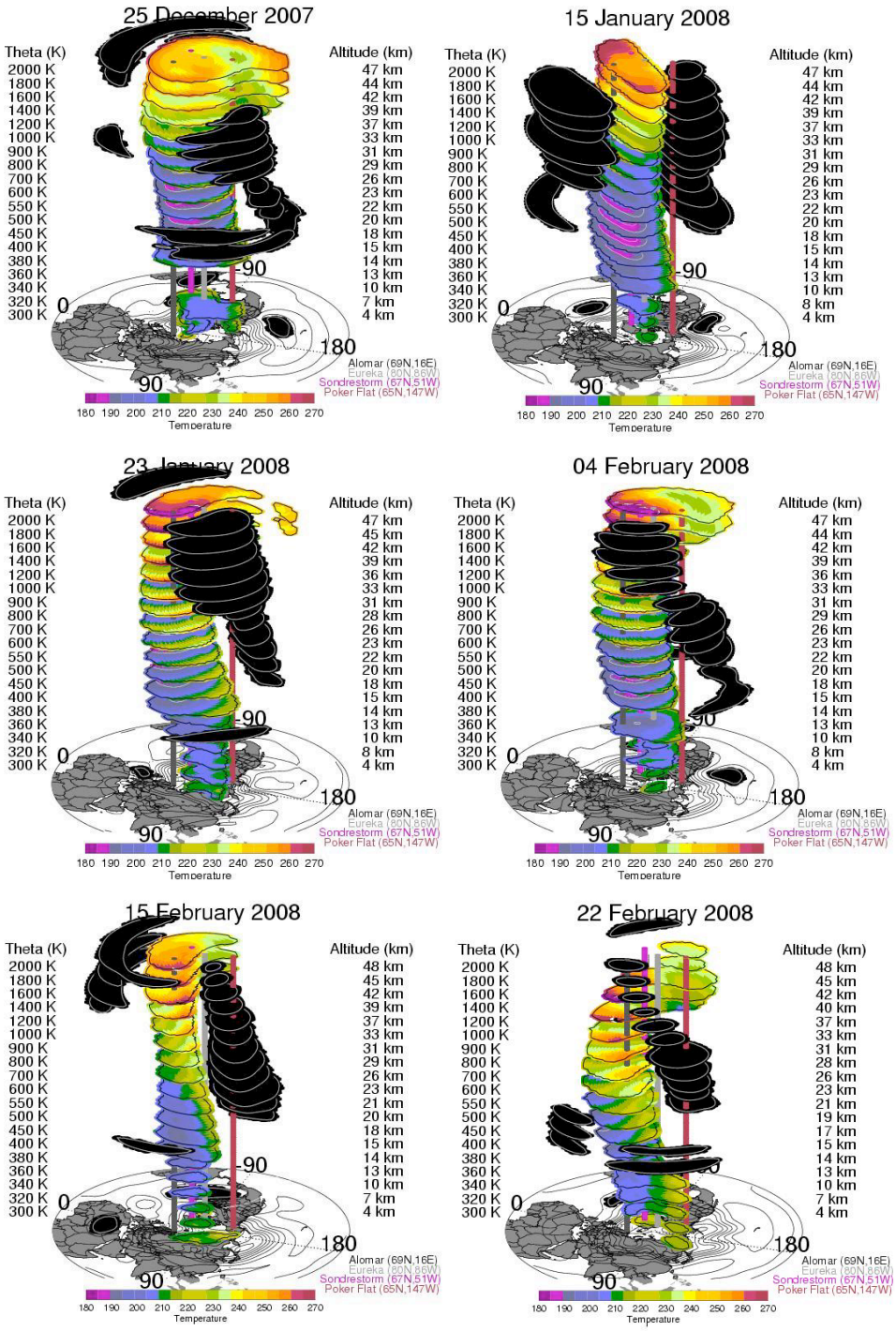

Figure 4.6. 3-D representation of the Arctic stratospheric vortex (color surfaces) and anticyclones (black surface) from 300 K to 2000 K isentropic surface on (top) 25 December 2007 and 15 January 2008, (mid) 23 January 2009 and 4 January 2009, (bottom) 15 and 22 February 2009.

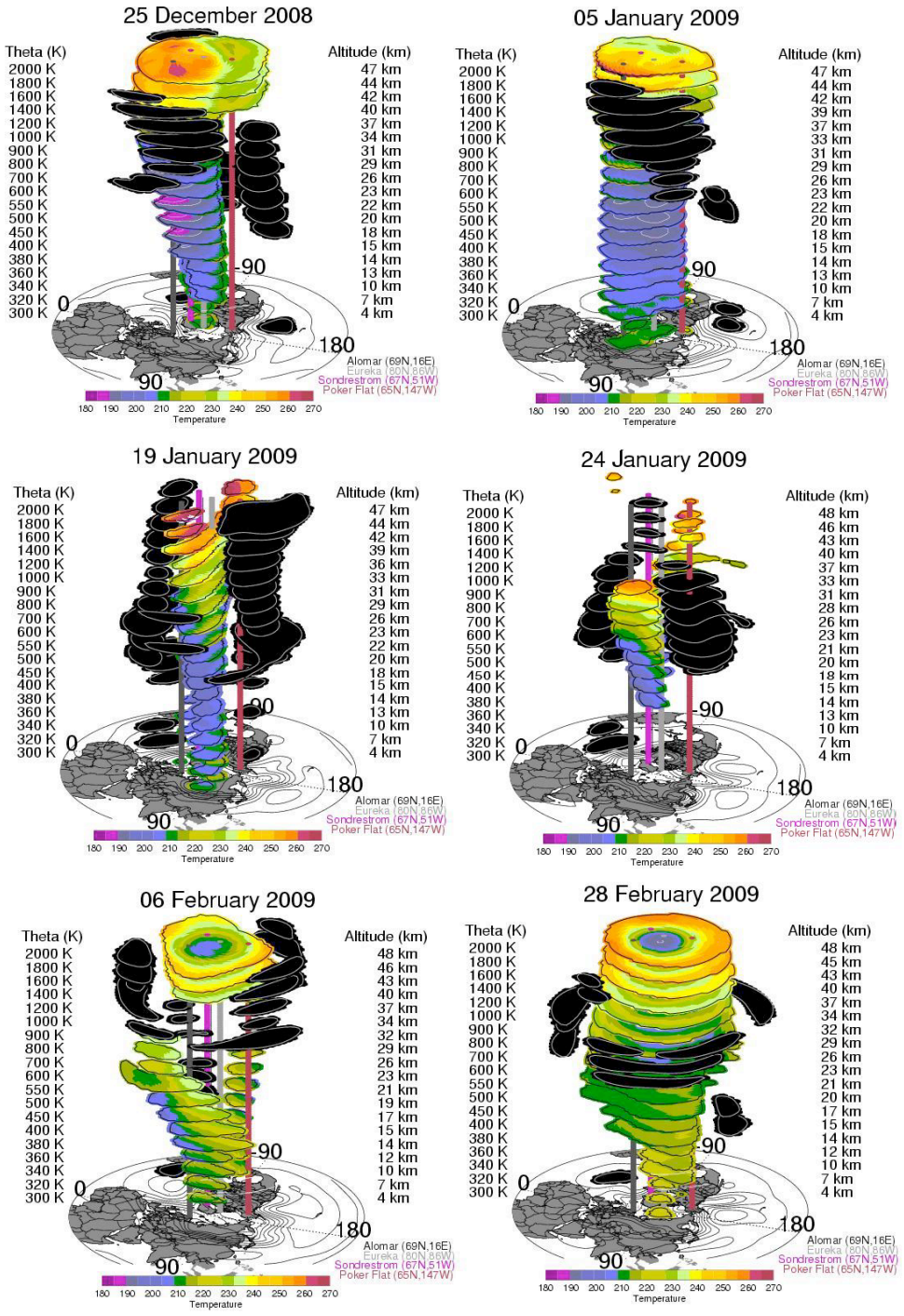

Figure 4.7. 3-D representation of the Arctic stratospheric vortex (color surfaces) and anticyclones (black surface) from 300 K to 2000 K isentropic surface on (top) 25 December 2008 and 5 January 2008, (mid) 19 and 24 January 2009, (bottom) 6 and 28 February 2009.

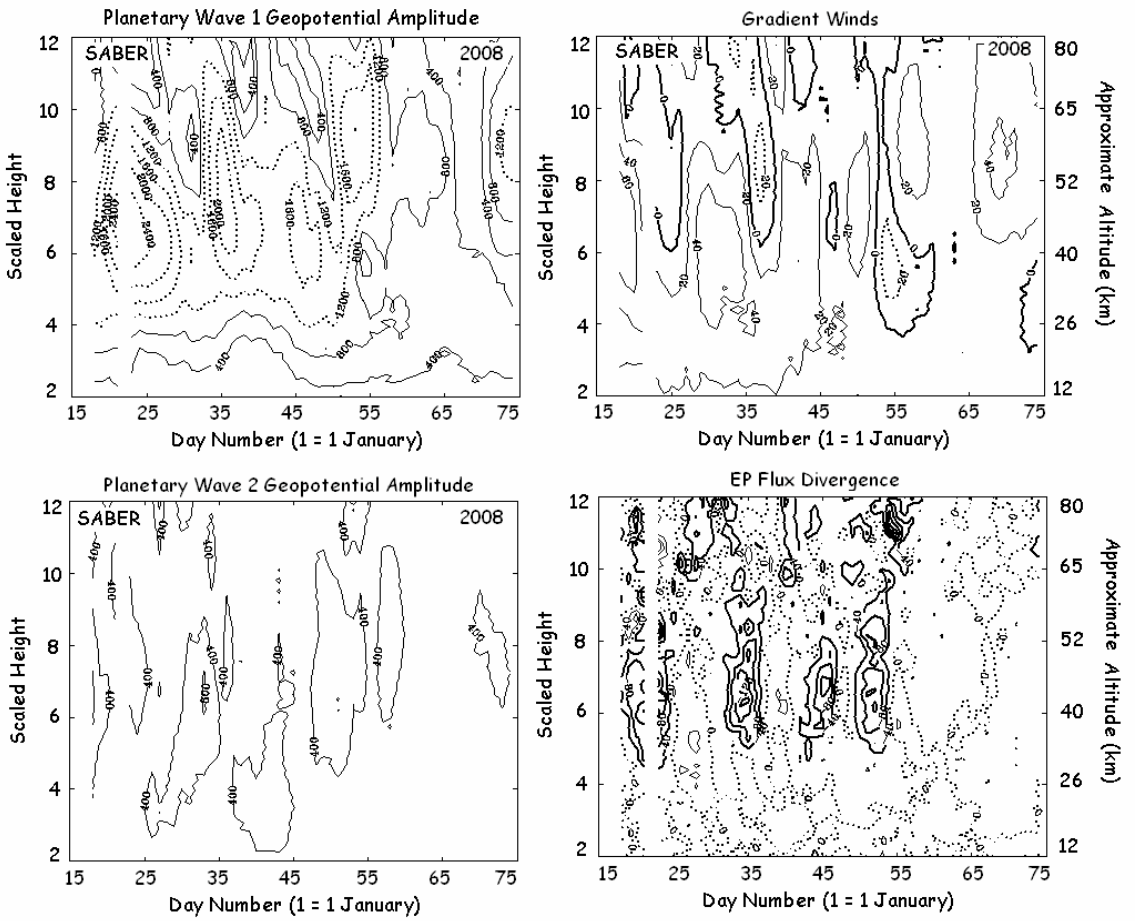

Figure 4.8. SABER planetary wave number one and two geopotential amplitude, gradient winds, and divergence of EP flux at 65^{o}N from mid-January to mid-March of 2008. Geopotential amplitudes greater then 1000 are dotted lines and the contour interval is 400 m. Negative winds are dotted lines and the zero wind line is solid thick line. Negative divergence values are solid lines. The contour intervals are 20 ms^{-1} for gradient winds and 40 $ms^{-1}day^{-1}$ for EP flux divergence.

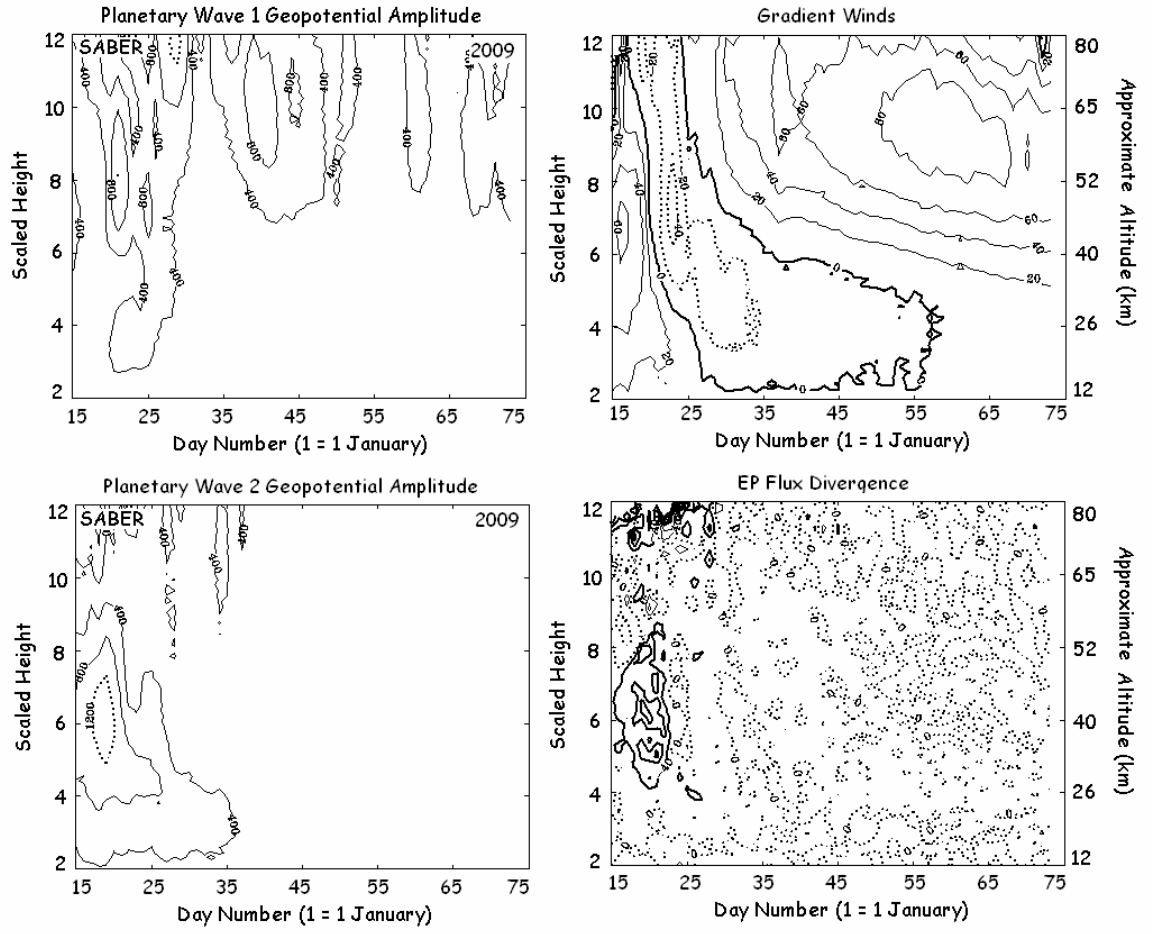

Figure 4.9. SABER planetary wave number one and two geopotential amplitude, gradient winds, and divergence of EP flux at 65^{o}N from mid-January to mid-March of 2009. Geopotential amplitudes greater then 1000 are dotted lines and the contour interval is 400 m. Negative winds are dotted lines and the zero wind line is solid thick line. Negative divergence values are solid lines. The contour intervals are 20 ms^{-1} for gradient winds and 40 ms^{-1}day^{-1} for EP flux divergence.

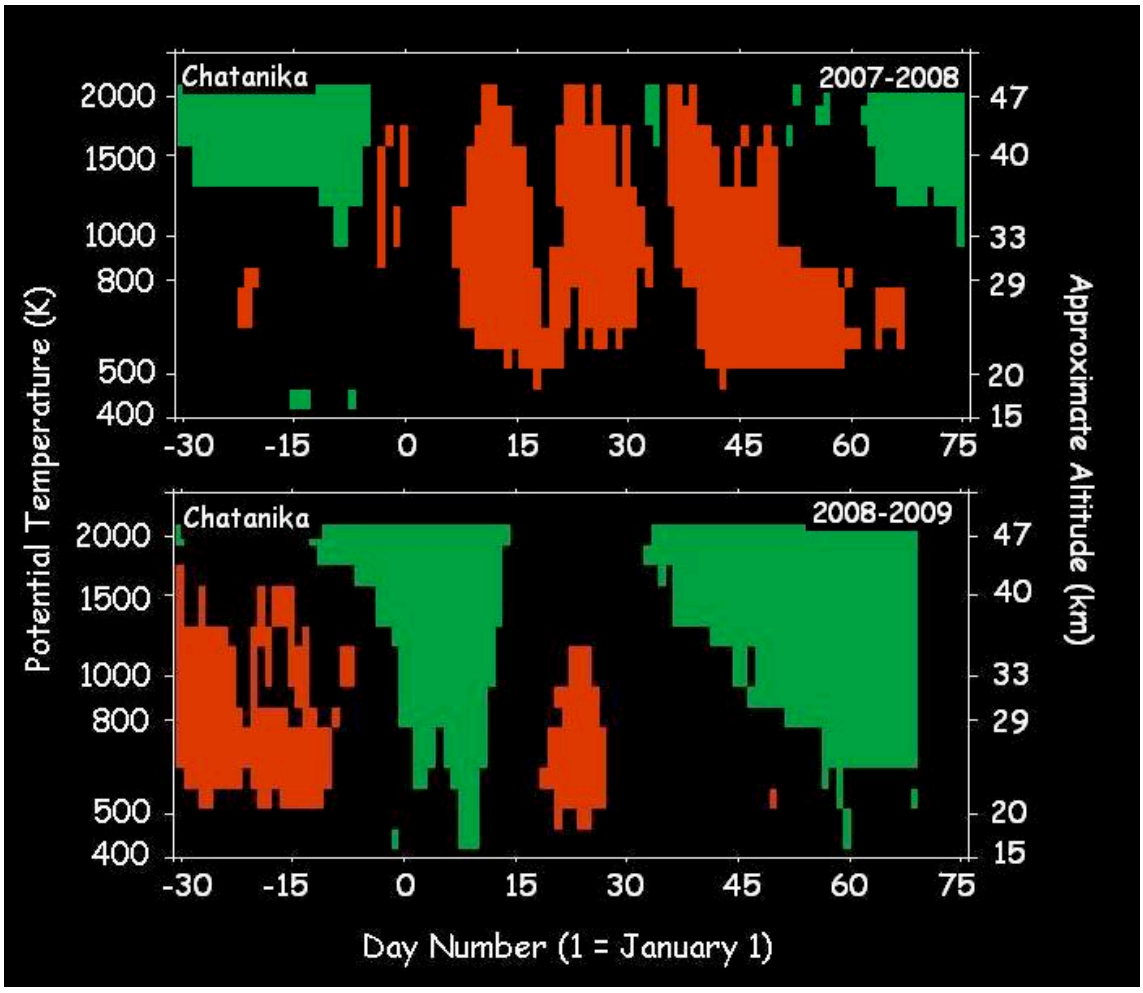

Figure 4.10. Temporal evolution of the stratospheric vortex (green) and Aleutian high anticyclone (red) over Chatanika, Alaska from 400 K (~14 km, ~130 hPa) to 2000 K (~48 km, 0.6 hPa) isentropic surface during DJF and mid March of 2007-2008 winter. Black represents the time period when neither system were above Chatanika.

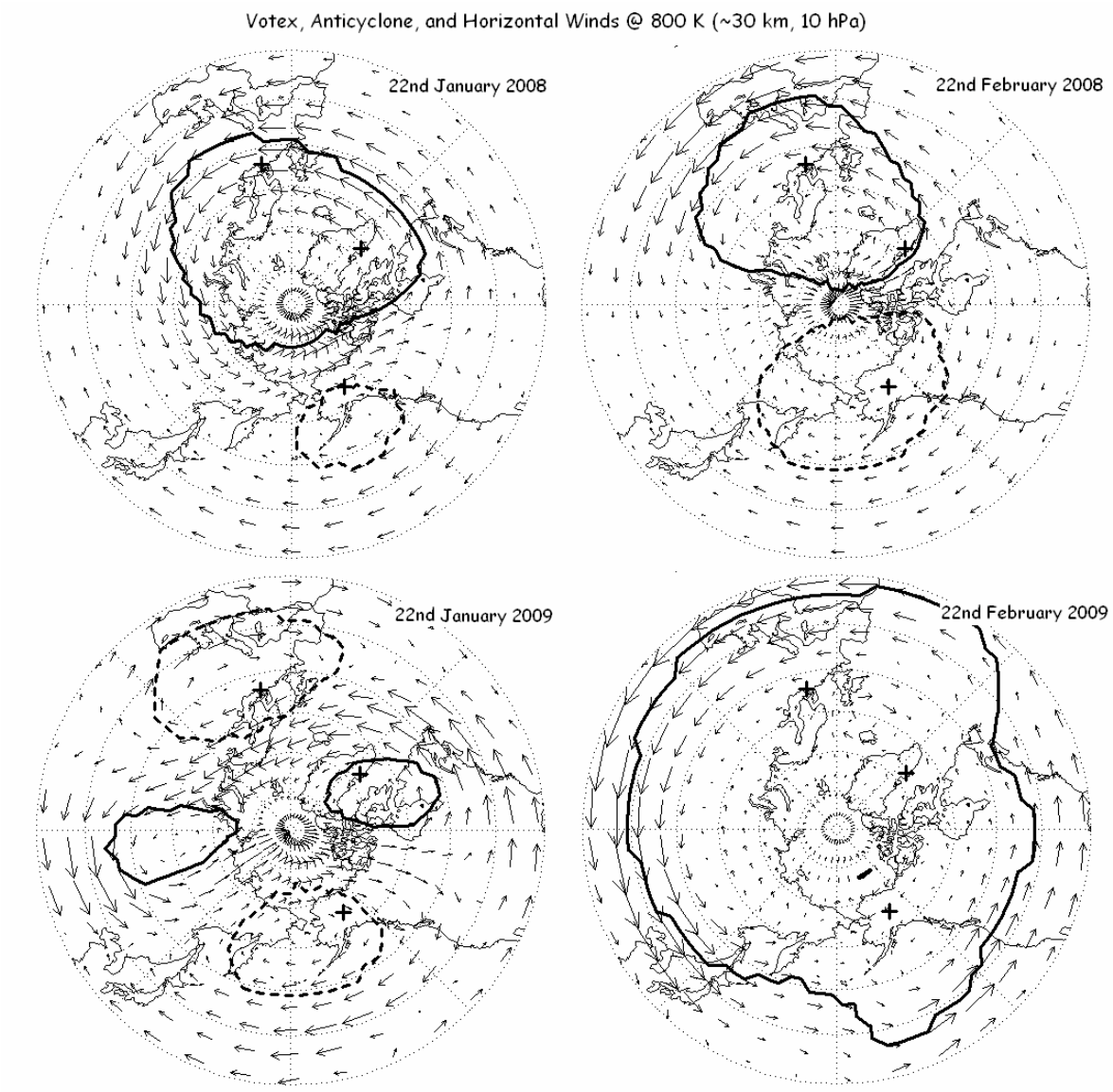

Figure 4.11. Northern hemisphere polar stereographic plots of vortex (thick line) and anticyclone (dashed line) at 800 K (~30 km, ~10 hPa) from MetO analyses data for (top) 22 January and 22 February 2008 and (bottom) 22 January and 22 February 2009. The horizontal winds are also plotted. The three sites Chatanika, Kühlungsborn, and Kangerlussuaq are marked with a plus symbol.

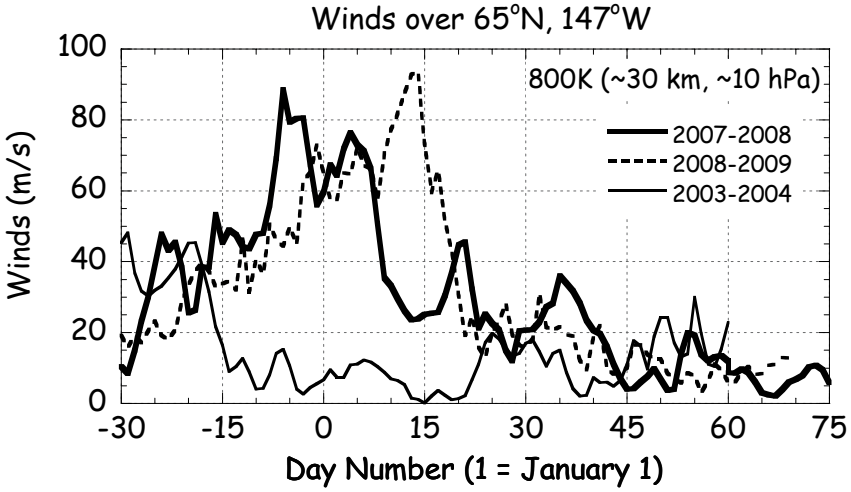

Figure 4.12. Daily horizontal wind speed from MetO analyses data at 800 K (~30 km, ~10 hPa) isentropic surfaces from December, January, February and mid-March of (top) 2003-2004, 2007-2008, and 2008-2009 Arctic winters at 65°N, 147°W.

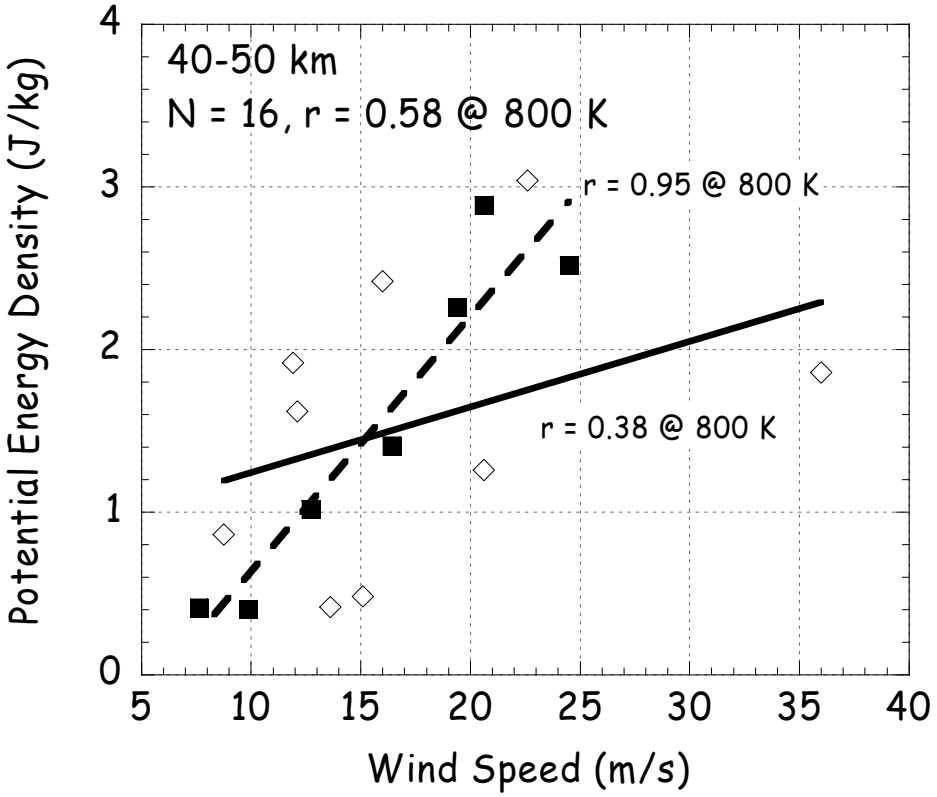

Figure 4.13. Scatter plot of potential energy density averaged over the 40-50 km altitude range and MetO wind speed after the first warming (late January and February) of 2007-2008 and 2008-2009 winters at Chatanika, Alaska. The overall correlation coefficient is given as well as the linear fit and correlation coefficient for each winter.

Chapter 5. Conclusions and Further Work

Rayleigh lidar measurements of the upper stratosphere and mesosphere are made on a routine basis over Poker Flat Research Range (PFRR), Chatanika, Alaska, (65°N, 147°W). Rayleigh lidar measurements have yielded high-resolution measurements of the density and temperature profile in the 40-80 km altitude. From these measurements we have calculated the gravity wave activity in the 40-50 km altitude. We documented the thermal structure of the stratosphere and mesosphere using an eight year data set, and analyzed the role of small-scale gravity waves on the large scale meridional circulation in terms of the synoptic structure of the Arctic stratospheric vortex, Aleutian anticyclone, and planetary wave activity.

5.1. Middle Atmosphere Temperature Measurements at Chatanika, Alaska

In Chapter 2 we used an eight year Rayleigh lidar data (1997-2005) to examine the temperature structure of the upper stratosphere and mesosphere over Chatanika, Alaska. Although individual measurements indicate a high degree of variability in the wintertime temperature profiles, the monthly mean temperatures follow an expected annual cycle with summer maximum and winter minimum below 60 km and an annual cycle with winter maximum and summer minimum above 60 km. The monthly mean temperatures are in general colder than those reported at other sites in Greenland and Scandinavia, and by the SPARC reference zonal mean temperature climatology. The Chatanika measurements were made during recent years with frequent major stratospheric warmings, while no warmings were reported during the climatology presented by other instruments at other locations. We attribute the colder January temperatures at Chatanika to the occurrence of major stratospheric warmings and the subsequent formation of an elevated stratopause with colder stratosphere.

5.2. Suppression of Gravity Wave Activity during the Formation of an Elevated Stratopause at Chatanika, Alaska

In Chapter 2 we presented a detailed analysis of the temperature structure of the upper stratosphere and mesosphere above Chatanika, Alaska. We associated the elevated stratopause with the observed colder temperatures. Model studies have shown that an elevated stratopause is the result of reduced gravity wave activity. In Chapter 3 we compared the gravity wave activity during three winters (2002-2003, 2003-2004, and 2004-2005) with different meteorological conditions and presented the first direct observational evidence of the suppression of gravity wave activity during the formation of an elevated stratopause during the 2003-2004 winter. This result observationally confirms recent modeling studies. Potential energy densities are positively correlated to winds in the lower stratosphere with a positive correlation coefficient of 0.74. This suggests that at least 50% of the observed gravity waves are modulated by winds in the lower stratosphere. The reduced gravity wave potential energy density and the reduced wind speeds during the 2003-2004 winter suggests that these waves are being modulated by critical layer interaction with weak winds. The largest amplitude waves during the 2004-2005 winter appear to be limited by saturation due to internal instabilities rather than the wave interaction with the mean flow.

5.3. Gravity Wave Activity during Different Types of Stratospheric Warmings

In Chapter 4 we extended the analysis in Chapter 3, and have compared the gravity wave activity during two different types of stratospheric warming events, a vortex displacement event during the 2007-2008 winter and a vortex split during the 2008-2009 winter. We do not find significant differences in magnitude of gravity wave potential energy density during the two warming events. However, we find different correlations of the potential energy densities with horizontal wind speeds, with low correlation during the 2007-2008 winter and high correlation during the 2008-2009 winter. This indicates that while the gravity waves are modulated by winds during the January 2009 warming, a

mix of physical processes with different wave sources modulate the gravity wave activity during the 2008 warming.

We also find a geographical variability in gravity wave potential energies from Chatanika, Kangerlussuaq, and Kühlungsborn during the 2007-2008 winter. The gravity waves at Kangerlussuaq and Kühlungsborn appear to be modulated by horizontal winds in the mid-stratosphere, and the gravity waves at Chatanika during this winter appear to be modulated by some other process (e.g. 'geostrophic adjustment' due to variable winds, a major source of gravity waves where unbalanced flow is restored to balanced flow). An elevated stratopause formed after the disruption of the middle atmospheric circulation after both the mid-winter warmings of January 2004 and 2009. We observe a higher wave activity over Chatanika after the 2009 warming compared to the 2004 warming. Our gravity wave analyses during different stratospheric warmings with different characteristics suggest that, in general the temporal variability in winds associated with each stratospheric warming influence the gravity wave variability at a particular location.

5.4. Further Work

While we can speculate that the colder stratospheric temperatures measured over Chatanika in Chapter 2 reflect the changing climate in the troposphere it is important to conduct a more comprehensive analysis of the contribution of the position of the polar vortex and stratospheric warming events to the observed thermal structure. Such an analysis would require a higher frequency of observations uniformly distributed across the Arctic. A detailed pan-Arctic multiyear analysis could be conducted using a combination of Rayleigh lidar data, SABER data for the period starting in 2002, and simulations from the WACCM model. The SABER data analysis would however be limited by its yaw cycle that extends only from mid-January to mid-March of each northern hemisphere winter.

Rayleigh lidars, in addition to temperature measurements, can also provide the much needed temporal measurements of gravity wave activity in the zonally asymmetric Arctic middle atmosphere. Owing to limitations in sampling resolution (i.e. 15 minute

density data used in Chapter 3) Rayleigh lidar measurements are limited in resolving the highest frequency gravity waves. Moreover measurements of zonal and meridional winds in the stratosphere are needed to obtain gravity wave characteristics like kinetic energy and direction of propagation (i.e. eastward or westward propagating). This can be provided by improving the current Doppler wind lidar technology. More direct measurements of temporal variability in gravity wave activity under different stratospheric warming events with a network of Arctic lidars in combination with the zonal mean measurements from satellites could give us more insight into the global variability of gravity wave activity and its role on the middle atmospheric circulation.

Appendix A. Calculation of Constant of Acceleration due to Gravity and Radius of the Earth at 65°N

Rayleigh lidar temperature retrieval algorithms are sensitive to the precision of the constants used. An accurate estimate of the gravitational constant and the radius of the Earth at Chatanika, Alaska, (65°N, 147°W) are necessary to obtain a precision of one part in 10^4 in retrieved temperatures. This appendix explains the methods used to compute the required constants of acceleration due to gravity at the surface and radius of the Earth, both at 65°N. The acceleration due to gravity can be computed using the following formula,

$$g_i = \frac{g_0}{\left(1 + z_i / a\right)^2} \tag{A.1}$$

where, g_i is the acceleration due to gravity at level i

g_0 is the acceleration due to gravity at the Earth's surface

z_i is the altitude at level $_i$

a is the radius of the Earth

The above equation is derived from Newton's law of universal gravitation which states that for two elements with mass M and m separated by a distance r, the force exerted by mass M on mass m due to gravity is,

$$F_g = -\frac{GMm}{r^2} \tag{A.2}$$

where G is the gravitational constant.

If M and m represent the mass of the Earth and the mass element of the atmosphere then the gravitational acceleration of the Earth exerts a force per unit mass on the atmosphere given by,

$$\frac{F_g}{m} = g = -\frac{GM}{r^2} \tag{A.3}$$

Assuming a constant radius of the Earth, *a,* substituting the distance $r = a + z$ in equation (A.3), $g_0 = -(GM/a^2)$ which is the acceleration due to gravity as a function of height z given by equation (A.1).

Both the radius of the Earth and the acceleration due to gravity varies as a function of latitude (φ). To estimate an accurate temperature profile from the lidar photon count data, accurate values of the gravitational constant and the radius of the Earth at 65°N are necessary. An equation of the acceleration due to gravity as a function of both latitude and altitude can be found in the CRC Handbook of Physics and Chemistry [*Lide*, 2007].

$$g_i = 9.780356 \times (1 + 0.0052885 \sin^2 \phi - 0.0000059 \sin^2 \phi) - 0.003086 z_i \qquad \text{(A.4)}$$

This equation has been referenced from *Jursa* [1985] who in turn refer to the Smithsonian meteorological tables [*List*, 1968]. *List* [1968] has adopted the equation from the "Meteorological Gravity System" based on the International Ellipsoid of Reference. This equation was recommended by W. D. Lambert (President of the International Association of Geodesy) in 1949 in his report on Gravity Formulas for Meteorological Purposes to the International Meteorological Organization.

Using the expressions for the acceleration due to gravity i.e. equations (A.1) and (A.4) and their rms error, two different methods (described below) have been used to find the acceleration due to gravity at the surface (g_0) and the Earth's radius (RE) at 65°N, with the least error. From equation (A.1) the root mean square error is given by,

$$erms = \frac{1}{N} \sum_{i=1}^{n} \left(g_i - \frac{g_0}{\left(1 + z_i / RE\right)^2} \right)^2 \qquad \text{(A.5)}$$

$$erms = \frac{1}{N} \sum_{i=1}^{n} \left(g_i^2 - \frac{2 g_i g_0}{\left(1 + z_i / RE\right)^2} + \frac{g_0^2}{\left(1 + z_i / RE\right)^4} \right) \qquad \text{(A.6)}$$

A.1. Method 1

In this method the Earth's radius is calculated for acceleration due to gravity that is constant at the surface (g_0), and varies as equation (A.4) with latitude and altitude. To derive an equation for the Radius of the Earth, *RE* I first differentiate *erms* in (A.6) with respect to *RE* and equate it to zero, and let $1/RE = \alpha$. Therefore,

$$\sum_{i=1}^{n} \frac{g_i z_i}{(1+\alpha z_i)^3} = \sum_{i=1}^{n} \frac{g_0 z_i}{(1+\alpha z_i)^5} \tag{A.7}$$

A.1.1. Linear Approximation

The following approximation is made,

$$\frac{1}{(1+\alpha z_i)^n} \approx 1 - n\alpha z_i \tag{A.8}$$

Applying this approximation to equation (A.7),

$$\sum_{i=1}^{n} g_i z_i (1 - 3\alpha z_i) = \sum_{i=1}^{n} g_0 z_i (1 - 5\alpha z_i) \tag{A.9}$$

Expanding and rearranging the variables, and substituting $RE = 1/\alpha$,

$$RE = \frac{3\sum_{i=1}^{n} g_i z_i^2 - 5g_0 \sum_{i=1}^{n} z_i^2}{\sum_{i=1}^{n} g_i z_i - g_0 \sum_{i=1}^{n} z_i} \tag{A.10}$$

A.1.2. Quadratic Approximation

From Taylor series,

$$(1+x)^n = 1 + nx + \frac{n(n-1)x^2}{2!} + \text{.....} \tag{A.11}$$

or,

$$(1+\alpha z_i)^{-n} = 1 - n\alpha z_i + \frac{n(n-1)(\alpha z_i)^2}{2!} + \text{.....} \tag{A.12}$$

Thus,

$$(1+\alpha z_i)^{-3} \approx 1-3\alpha z_i+6\alpha^2 z_i^2$$

(A.13)

$$(1+\alpha z_i)^{-5} \approx 1-5\alpha z_i+15\alpha^2 z_i^2 \qquad \text{(A.14)}$$

Substituting (A.13) and (A.14) in (A.7), and rearranging,

$$A\alpha^2+B\alpha+C=0 \qquad \text{(A.15)}$$

where,

$$A=6\sum_{i=1}^{n} g_i z_i^3-15g_0\sum_{i=1}^{n} z_i^3 \qquad \text{(A.16)}$$

$$B=5g_0\sum_{i=1}^{n} z_i^2-3\sum_{i=1}^{n} g_i z_i^2 \qquad \text{(A.17)}$$

$$C=\sum_{i=1}^{n} g_i z_i-g_0\sum_{i=1}^{n} z_i \qquad \text{(A.18)}$$

Solving the quadratic equation (A.14), and substituting $RE = 1/\alpha$,

$$RE=\frac{2A}{-A\pm\sqrt{B^2-4AC}} \qquad \text{(A.19)}$$

A constant value of g_0 = 9.82281 at 65^{o}N, and equation (A.4) for variable g_i are substituted in equation (A.10) and (A.19) to determine the value of *RE* at different altitude levels, N. Equation (A.6) is used to determine the rms error, *erms*. A best fit to the *RE* determined by quadratic approximation with 10 m resolution was also determined. The results with N=11, and N=101 are given in Table A.1.

A.2. Method 2

In this method both the values of g_0 and *RE* are computed by deriving two equations with two unknowns, g_0 and *RE*. To derive the equations with unknowns g_0 and *RE, erms* in (6) is differentiated with respect to g_0 (*RE*) and equated to zero, and $1/g_0 = \alpha$ ($1/RE = \beta$). This implies,

$$\alpha\sum_{i=1}^{n}(1-4\beta z_i)=\sum_{i=1}^{n} g_i(1-2\beta z_i) \qquad \text{(A.20)}$$

and,

$$n\alpha - 4\alpha\beta\sum_{i=1}^{n} z_i = \sum_{i=1}^{n} g_i - 2\beta\sum_{i=1}^{n} g_i z_i \tag{A.21}$$

Similarly,

$$\alpha\sum_{i=1}^{n}(1-5\beta z_i)z_i = \sum_{i=1}^{n} g_i z_i(1-3\beta z_i) \tag{A.22}$$

implies

$$\alpha\sum_{i=1}^{n} z_i - 5\alpha\beta\sum_{i=1}^{n} z_i^2 = \sum_{i=1}^{n} g_i z_i - 3\beta\sum_{i=1}^{n} g_i z_i^2 \tag{A.23}$$

From (22) and (23),

$$\alpha\beta = \frac{\alpha n - \sum_{i=1}^{n} g_i + 2\beta\sum_{i=1}^{n} g_i z_i}{4\sum_{i=1}^{n} z_i} \tag{A.24}$$

$$\alpha\beta = \frac{\alpha\sum_{i=1}^{n} z_i - \sum_{i=1}^{n} g_i z_i + 3\beta\sum_{i=1}^{n} g_i z_i^2}{5\sum_{i=1}^{n} z_i^2} \tag{A.25}$$

Solving (24) and (25) for α,

$$\alpha = \frac{1}{g_0} = \frac{\gamma - \beta C_\beta}{C_\alpha} \tag{A.26}$$

where,

$$\gamma = 4\sum_{i=1}^{n} z_i \sum_{i=1}^{n} g_i z_i - 5\sum_{i=1}^{n} z_i^2 \sum_{i=1}^{n} g_i \tag{A.27}$$

$$C_\beta = 10\sum_{i=1}^{n} g_i z_i \sum_{i=1}^{n} z_i^2 - 12\sum_{i=1}^{n} z_i \sum_{i=1}^{n} g_i z_i^2 \tag{A.28}$$

$$C_\alpha = 5n\sum_{i=1}^{n} z_i^2 - 4\sum_{i=1}^{n} z_i \sum_{i=1}^{n} z_i \tag{A.29}$$

Substituting the expression for α (A.26) into equation (A.21) and solving for the quadratic equation for β,

$$RE = \frac{1}{\beta} = \frac{2A}{-A \pm \sqrt{B^2 - 4AC}} \tag{A.30}$$

where,

$$A = \frac{4\sum_{i=1}^{n} z_i C_\beta}{C_\alpha} \tag{A.31}$$

$$B = -\frac{nC_\beta}{C_\alpha} - \frac{4\sum_{i=1}^{n} z_i \gamma}{C_\alpha} + 2\sum_{i=1}^{n} g_i z_i \tag{A.32}$$

$$C = \frac{n\gamma}{C_\alpha} - \sum_{i=1}^{n} g_i \tag{A.33}$$

The values of g_0, *RE*, and RMS from equations from (A.26), (A.30), and (A.5) respectively, for N=11 at latitude 65^{o}N altitude levels are tabulated in Table A.2

A.3. Result

From method 2 a surface acceleration due to gravity of 9.8227 m/s^2 is obtained which is equal to three significant digits of the value of 9.8228 m/s^2 reported in the CRC Handbook of Physics and Chemistry [*Lide*, 2007]. The Earth's radius, *RE* is different in the linear approximation, quadratic approximation, and 'best fit' quadratic approximation in method 1, and in method 2. The smallest rms error, *erms* is in method 1 – 'best fit' Earth radius at 11 altitude levels. In summary, at 65^{o}N the acceleration due to gravity of 9.8228 m/s^2 and the radius of the Earth of 6.354 x 10^3 km are used in the Rayleigh lidar temperature retrieval algorithm.

References

Jursa, A. S. (1985), Ed., *Handbook of geophysics and the space environment*, p. 7-14, 4th ed., Air Force Geophysics Laboratory.

Lide, D. R. (2007), Ed., *CRC handbook of physics and chemistry*, 87th ed., p. 14-12, CRC Press.

List, R. J. (1968), *Smithsonian Meteorological Tables*, p. 488, 6th revised ed., Smithsonian Institution Press.

Table A.1. Variation of Earth's radius (*RE*) in km and root mean square error (*erms*) at different altitude levels for the linear approximation, quadratic approximation, and the best fit, at latitude (a) 65° N (b) 65.1° N (c) equator (0°), and (d) pole (90° N).

Altitude Levels: N(z)	Linear approximation: RE_L [km], (*erms*)	Quadratic approximation: RE_Q [km], (*erms*)	Best Fit: RE_B [km], (*erms*)
11 [a]	6389.62 (1.01×10^{-4})	6354.13 (8.69×10^{-6})	6354.26 (8.68×10^{-6})
101 [a]	6592.16 (9.07×10^{-3})	6240.33 (9.00×10^{-4})	6253.16 (8.25×10^{-4})
11 [b]	6389.66 (1.01×10^{-4})	6354.18 (8.69×10^{-6})	6354.31 (8.68×10^{-6})
101 [b]	6592.21 (9.07×10^{-3})	6240.37 (9.00×10^{-4})	6253.20 (8.25×10^{-4})
11 [c]	6362.10 (1.02×10^{-4})	6326.62 (8.73×10^{-6})	6326.75 (8.72×10^{-6})
101 [c]	6564.65 (9.11×10^{-3})	6212.75 (9.05×10^{-4})	6225.64 (8.29×10^{-4})
11 [d]	6395.63 (1.01×10^{-4})	6360.14 (8.68×10^{-6})	6360.27 (8.67×10^{-6})
101 [d]	6598.17 (9.06×10^{-3})	6246.35 (8.99×10^{-4})	6259.16 (8.24×10^{-4})

[a] Latitude 65° N

[b] Latitude 65.1° N

[c] Equator

[d] Pole 90° N

Table A.2. Acceleration due to gravity, variation of Earth's radius (*RE*), and root mean square error (*rms*) at different altitude levels for latitude (a) 65° N (b) 65.1° N (c) equator (0°), and (d) pole (90° N).

Altitude Levels: N(z)	Acceleration due to gravity, g_0 [m/s^2]	*RE* [km], *erms*
11 [a]	9.82273	6413.35 (1.12×10^{-4})
101 [a]	9.81485	6842.63 (9.55×10^{-3})
11 [b]	9.82280	6413.39 (1.12×10^{-4})
101 [b]	9.81492	6842.67 (9.55×10^{-3})
11 [c]	9.78028	6385.84 (1.12×10^{-4})
101 [c]	9.77237	6815.03 (9.59×10^{-3})
11 [d]	9.83200	6419.36 (1.11×10^{-4})
101 [d]	9.82413	6848.65 (9.54×10^{-3})

[a] Latitude 65° N

[b] Latitude 65.1° N

[c] Equator

[d] Pole 90° N

Appendix B. Effect of Binning Photon Counts on Rayleigh Lidar Temperature Retrieval

This appendix describes the stratospheric and mesospheric temperatures calculations from the lidar backscattered photon counts, using IDL© program. The procedure describes how the photon counts are binned and temperatures calculated at the center of each range bin. The error in temperature profile if the photon counts are not binned correctly is also described. The Rayleigh lidar raw photon count data extends from the ground (0.394 km) to 307.575 km. The altitude of the lidar system at PFRR is 0.394 km above mean sea level (ASL). The altitude resolution (Δz) of the data is 75 m.

The temperature profile is calculated at the center of each range bin, Δz = 75 m by taking a running geometric mean between two successive altitude levels (i.e. apply smoothing to center integration). For example if the ground is assumed to be at 0 km then for a range resolution of 75 m the first temperature ASL is calculated at 37.5 m, the second is calculated at 112.5 m etc. Since the Rayleigh lidar at PFRR is at 0.394 km ASL the first data will be at a height of 431.5 m (37.5 m + 394.0 m), the second at 506.5 m (431.5 + 75.0) etc. A schematic of the range bins and center of each range bin for ground at 0 km and ground at 0.394 km is shown in Figure B.1. Since the relative density is calculated directly from the photon count data (i.e. no integration is required) geometric mean is not used.

To test the IDL© algorithm the photon counts are created to generate an isothermal atmosphere (i.e. an atmosphere where the temperature remains constant with altitude). The density profiles are defined using, $\rho = \rho_o \exp\left(-z/H\right)$ where the scale height $H = RT/g$, ρ_o is the density at the surface, z the geometric height, R the gas constant for dry air, T the isothermal temperature, g the gravitational acceleration. This density profile is used to generate photon counts. These photon counts are then converted to relative density and temperature profiles. The following sections illustrate the various steps for

the creating an isothermal atmosphere and the errors in temperatures if the photon counts are not binned correctly.

B.1. Density Calculation

First the density is generated over the altitude range of 0.4315 km to 307.557 km as predictor integration. The one-dimensional altitude array *ZKM* of size 4096 is at the center of each range bin. The acceleration due to gravity varies as a function of altitude and is given by,

$$GRAV = \frac{G}{\left[1.0 + ZKM/REARTH\right]^2} \tag{B.1}$$

Where, the gravitational constant G = 9.8228 m/s^2, and the radius of the earth at 65^{o}N *REARTH* = 6.354 x 10^3 km (see Appendix A1 for more details). The density data is placed in the array *DEN* of size 4096 and is defined as,

$$DEN_j = DEN_{j-1} \text{ x } exp(-C1 \text{ x } GRAV_{j-1}) \tag{B.2}$$

where, *DEN(0)* = 1 is the normalized density at the lowest altitude of 0.4315 km, and the constant $C1 = \frac{Mair \times \Delta z \times 1000.0}{R \times TK0}$, the mean molecular weight of air *Mair* = 0.028964 kg/mol, the universal gas constant *R*= 8.3145 J/(mol.K), and the isothermal temperature *TK*0 = 200.0 K. Figure B.2 shows the normalized density profile.

B.2. Photon Count Calculation

The second step is to generate photon counts over the entire altitude range of 0.4315 km to 307.557 km. The photon count data is placed in an array *RYDATA* of size 4096 by scaling the density by *Z2*. Figure B.3 shows the generated photon count profile.

$$RYDATA = DEN \times \left(1.0/Z2\right) \tag{B.3}$$

where,

$$Z2 = \left(\frac{ZKM - 0.394}{ZKM(0) - 0.394}\right)^2 \tag{B.4}$$

$$ZKM(0) = 0.4315 \text{ km} \tag{B.5}$$

The photon counts data is then normalized over the 60.0 to 65.0 km range using *RyNORM* which is the total of *RYDATA* over 60.0 to 65 km. Array number 795 and 860 point to 60.0 km and 65.0 km

$$RYDATA = RYDATA/RyNORM \tag{B.6}$$

$$RyNORM = \text{TOTAL}(RYDATA(WNORM(795{:}860))) \tag{B.7}$$

B.3. Temperature Calculation

The final step is to calculate the isothermal temperature profile from the generated photon counts in the desired altitude of 40.0 to 80.0 km. This is a subset of the entire altitude range over altitudes from ZKM(528) = 40.0315 km and ZKM(1060) = 79.9315 km, and constitutes an array of 533 points. The temperature retrieval is a progressive downward integration from the highest to lowest altitude. The temperature is temporarily stored in an array *TEMPI* before being stored in *RYTEMP*. As an example a description of how temperatures are calculated at the first top three points, 532, 531, and 530 is given below.

In this example the highest temperature at 80 km is assumed to be equal to 200.0 K (i.e. *TEMPI*(532) = 200.0 K). This initial or seed temperature used in the Rayleigh lidar retrival is obtained from the SPARC reference atlas [SPARC, 2002]. The photon counts are then scaled by *Z2* to obtain the relative density stored in an array *WORK*.

$$WORK(0{:}1) = RyDATA(531{:}532) \text{ x } Z2(531{:}532) \tag{B.8}$$

The relative density is normalized by the value of the density at the bottom altitude, and save the value of the relative density at the altitude of the temperature guess in *Rat0*. Then a running geometric mean of WORK is taken to obtain a value at the center of the integration.

$$WORK(0{:}1) = WORK(0{:}1) \,/\, WORK(0) \tag{B.9}$$

$$Rat0 = WORK(1) \tag{B.10}$$

$$WORK(0) = \sqrt{WORK(0) \times WORK(1)} \tag{B.11}$$

Then *IntD* is calculated as the part of the solution from the integration and *Int0* is the part of the solution from the guess. Finally the temperature *TempI*(531) is calculated as the sum of *IntD* and *Int0*.

$$IntD = \text{TOTAL}(WORK(0) \text{ x } GRAV(531)) \tag{B.12}$$

$$IntD = IntD \times Mair/R \times \Delta z \times 10^3 \tag{B.13}$$

$$Int0 = Rat0 \text{ x } TK0 \tag{B.14}$$

$$TempI(531) = Int0 + IntD \tag{B.15}$$

To obtain *TempI*(530) the above steps are repeated with WORK initialized to an array of three points.

$$WORK(0{:}2) = RyDATA(530{:}532) \text{ x } Z2(530{:}532) \tag{B.16}$$

$$WORK(0{:}2) = WORK(0{:}2) / WORK(0) \tag{B.17}$$

$$Rat0 = WORK(2) \tag{B.18}$$

$$WORK(0) = \sqrt{WORK(0) \times WORK(1)} \tag{B.19}$$

$$WORK(1) = \sqrt{WORK(1) \times WORK(2)} \tag{B.20}$$

$$IntD = \text{TOTAL}(WORK(0{:}1) \text{ x } GRAV(530{:}531)) \tag{B.21}$$

$$IntD = IntD \times Mair/R \times \Delta z \times 10^3 \tag{B.22}$$

$$Int0 = Rat0 \text{ x } TK0 \tag{B.23}$$

$$TempI(530) = Int0 + IntD \tag{B.24}$$

Finally all the *TempI* values are stored in the temperature array *RYTEMP* of size 533.

$$RYTEMP = TempI(0{:}532) \tag{B.25}$$

Figure B.4 shows the isothermal temperature profile obtained from the above calculations on two different x-axis ranges.

The above IDL© algorithm calculates an isothermal temperature profile that is accurate within 1 part in 10^6 parts. Figure B.5 shows the temperature profile obtained when the photon counts are shifted by one and 10 range bins. Introducing a shift of one bin gives an error of ~0.05%. A comprehensive methodology of calculating the temperatures and density from the real Rayleigh lidar data from Chatanika can be found in the Appendix of *Wang* [2003].

References

SPARC, 2002 (2002): *SPARC intercomparison of middle atmosphere climatologies*, SPARC Rep. 3, 96 pp.

Wang, W. (2003), *Spectral estimation of signal and noise power in Rayleigh lidar measurements of the middle atmosphere*, MS Thesis, University of Alaska Fairbanks, 2003.

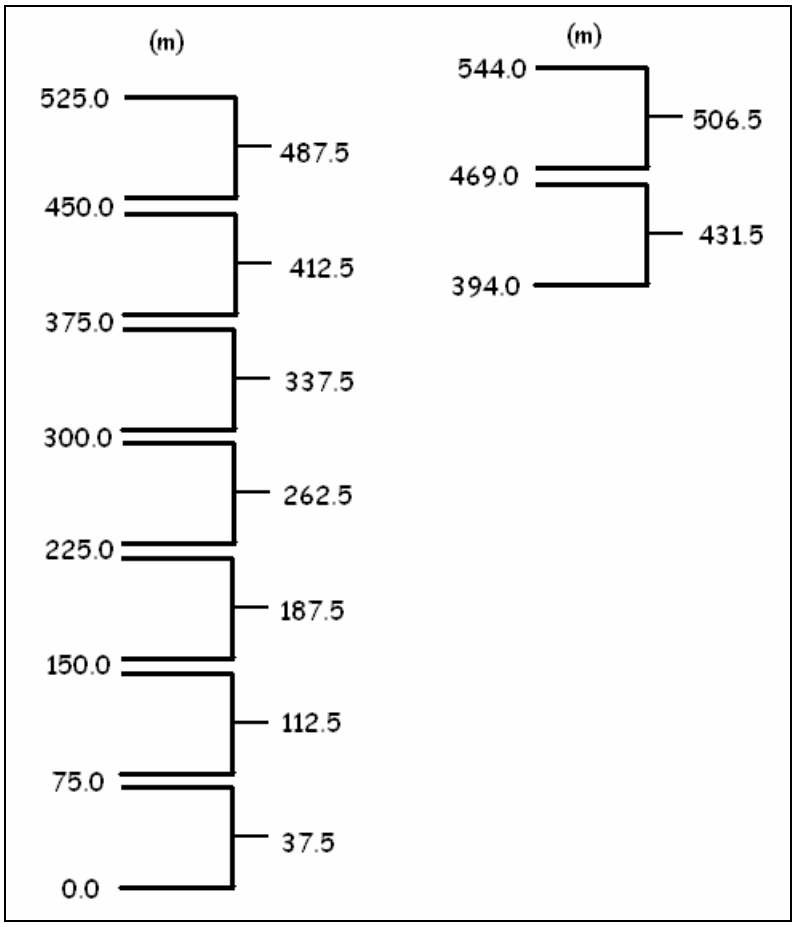

Figure B.1. Range bins and center of range bin in meters starting from (left) ground and (right) from 394.0 m. The altitude of the lidar system at PFRR is 394.0 m above mean sea level.

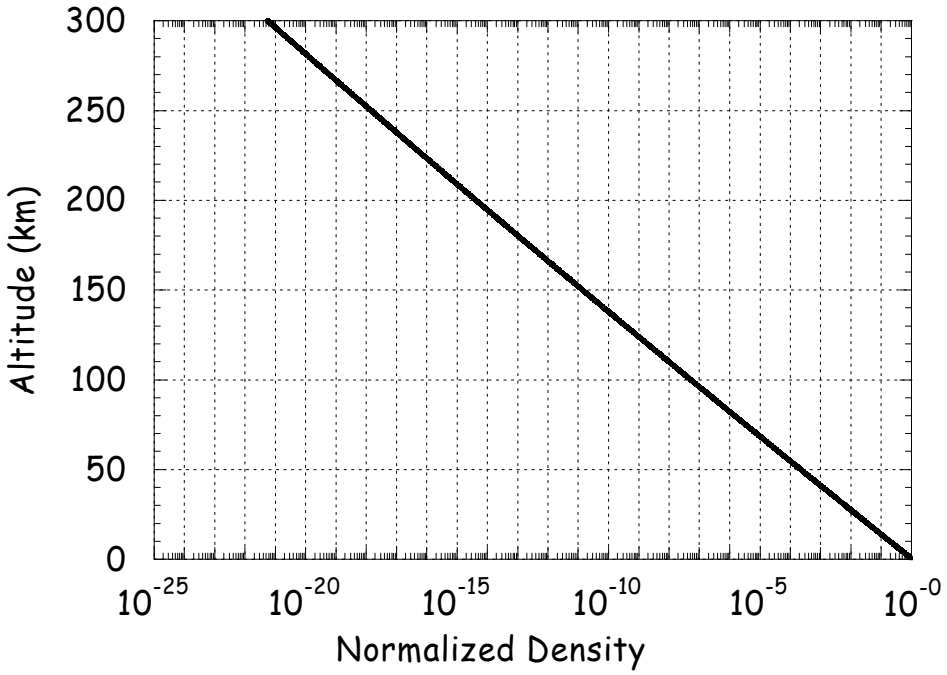

Figure B.2. Normalized density profile from 0.0 to 300.0 km plotted on a logarithmic x-axis.

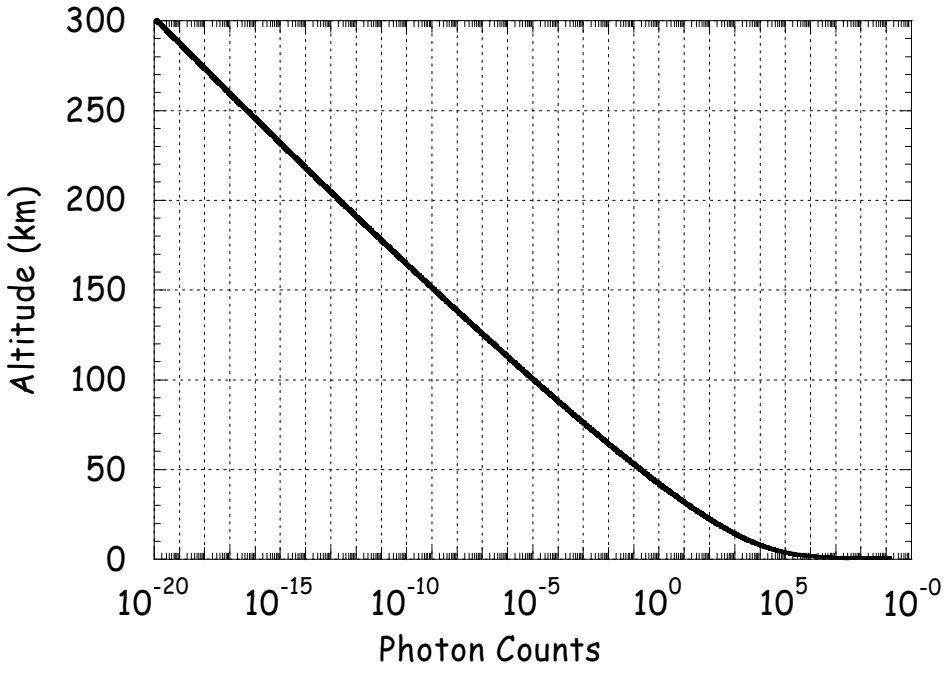

Figure B.3. Generated photon count profile from 0.0 to 300.0 km plotted on a logarithmic x-axis

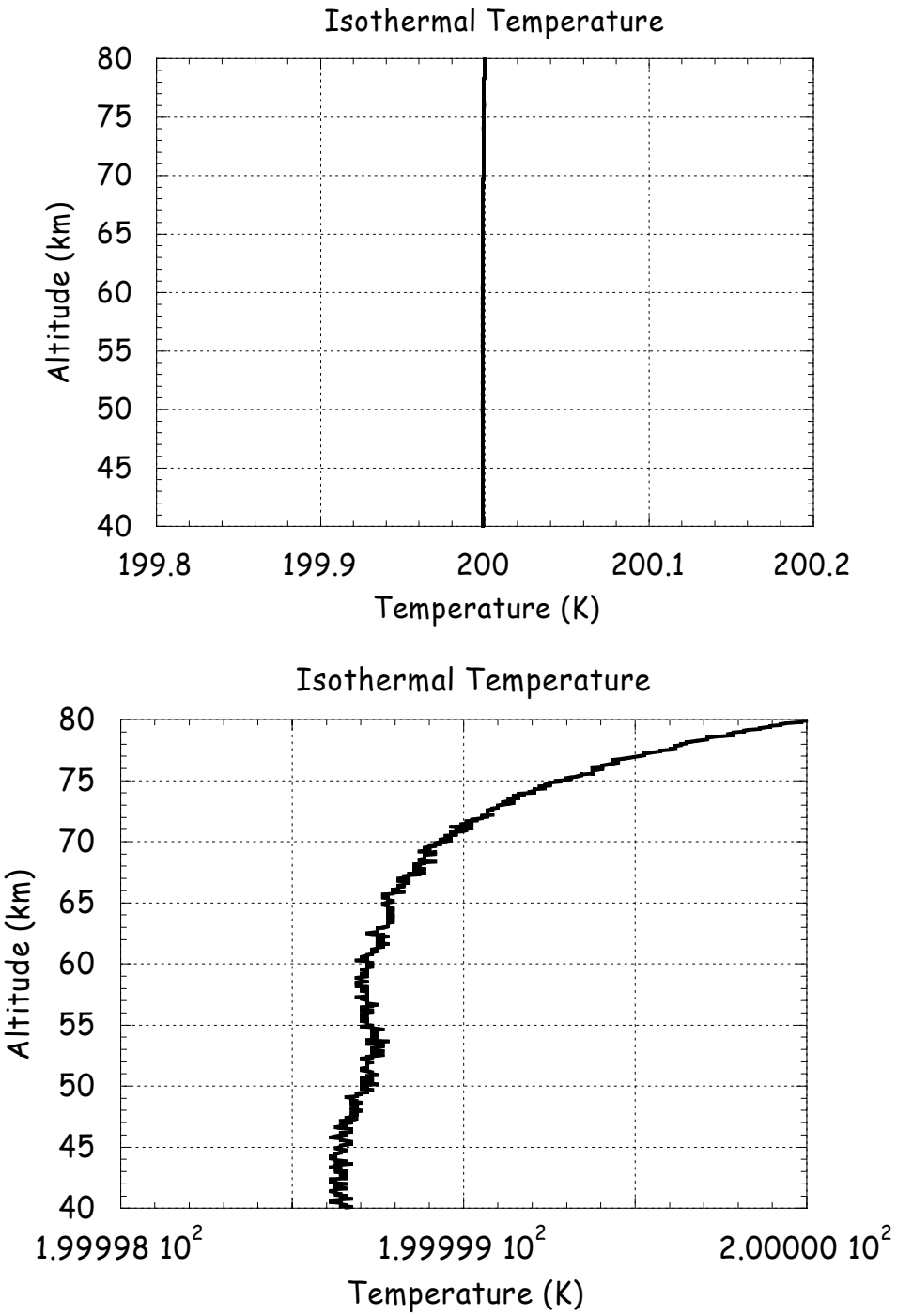

Figure B.4. Isothermal temperature profile from 40.0 to 80.0 km. The bottom plot shows the same profile on an x-axis with six significant digits.

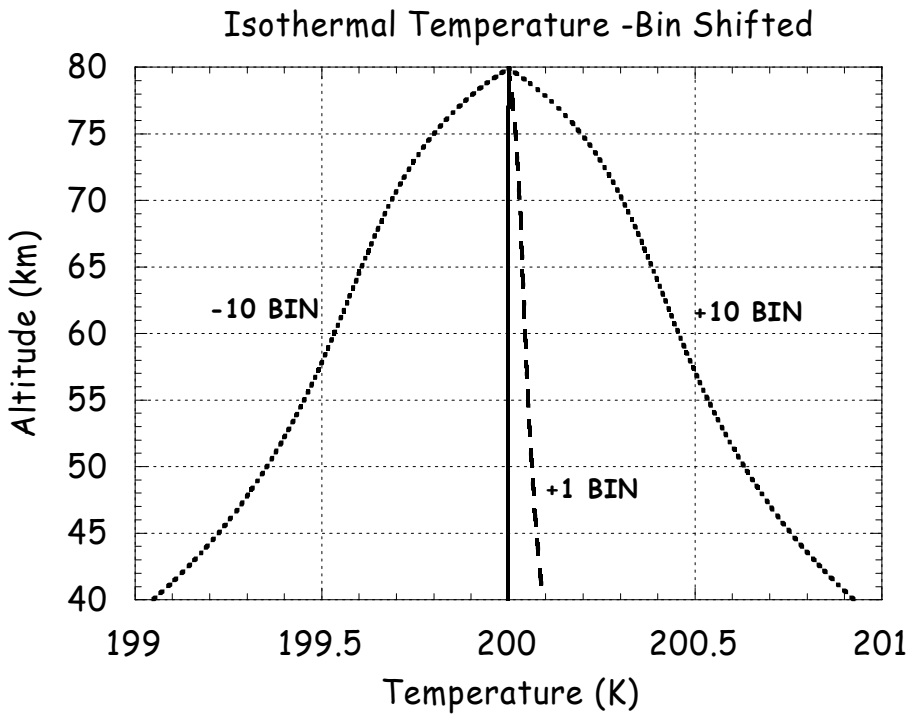

Figure B.5. Isothermal temperature profiles from 40.0 to 80.0 km with no bin shift (solid line), shifted by +1 bin (dashed line), and by +10 and -10 bins (dotted line).

Appendix C. Effect of Exponential Smoothing on Gravity Wave Variances

The raw photon count data are spatially filtered (smoothed) to obtain more robust estimates of density and temperature profile. The photon counts are exponentially smoothed by applying a running average over 2.0 km (27 range bins), to the logarithm of the photon count profile. Averaging over N bins reduces the standard deviation in the counts by $N^{1/2}$ thus reducing the noise fluctuations. In this appendix the effect of this smoothing on the geophysical variability (associated with gravity wave variance) of the lidar data is investigated.

To examine the effect of exponential smoothing of photon counts on gravity wave variances, first the unsmoothed data in the relative density perturbation m-spectrum is considered. The density perturbations calculated from the unsmoothed photon count data are spatially band-limited between vertical wavelengths of 2 km (mc2 = 1.0/2.0 = 0.5 km^{-1}) and the vertical altitude range of 15 km (45-60 km altitude range, mc1 = 1/15.0 km = 0.067 km^{-1}) and temporally band-limited by the Nyquist frequency, 0.5 h (double the sampling time of 15 minute and the low frequency 0.25 h^{-1} (corresponding to a period of 4 h). Then the spectrum of the density perturbation is calculated using the periodogram method [*Koopmans*, 1974]. The periodogram estimates the spectrum as the square of the magnitude of the Fast Fourier Transform (FFT) [*Wang*, 2003]. Filtering the data at a cutoff wavenumber m, eliminates all spectral components at wavenumbers greater than m.

The relative density perturbation spectrum is a superposition of the base-band spectrum which is the signal component and a white noise spectrum, which is the noise component. The total power (signal + noise) in the spectrum is given by integrating the spectrum over the wavenumber range mc1 = 0.067 km^{-1} and mc2 = 0.5 km^{-1}, and is stored in the array *PCFFT_TOT*. The noise spectrum (*NZC_TOT*) is calculated by averaging the value of the relative density perturbation spectrum over the high wavenumber range that is dominated by white noise. The calculations are repeated to

determine the total power in the spectrum using the smoothed photon count data to obtain *PCFFT_TOTs*.

The signal component of the unsmoothed total power is compared to the smoothed total power by calculating their ratio.

$$RATIO = \frac{PCFFT\_TOT - NZC\_TOT}{PCFFT\_TOTs - 0.45 \times NZC\_TOT} \tag{C.1}$$

The 0.45 is the cutoff wavenumber required to smooth the noise floor spectrum.

From 15 nights of observation during the winter of 2007-2008, the signal to noise ratio (SNR) over the 45-60 km altitude range in the 15 minute lidar data varies from a minimum of 0.12 to a maximum of 1.66. The mean value is 0.73 and median is 0.63. The ratio of variance (*RATIO*) varies from 0.91 to 5.65 with a mean value of 2.03 and a median of 1.74. A scatter plot of SNR vs *RATIO* is shown in Figure C.1. If the two outlier RATIO points of 3.28 and 5.65 are removed, the RATIO for the 13 points varies from 0.91 to 2.40 with a mean of 1.66 and median of 1.71.

In the gravity wave analysis in Chapter 3 the lidar wave potential energy was compared to the potential energies reported by Wilson *et al*. [1991] at Observatoire de Haute Provence (44^{o}N, 6^{o}E) and the Centre d'Essais des Landes at Biscarosse (44^{o}N, 1^{o}W) in France. Wilson *et al*. [1991] used Rayleigh lidar data from the two sites with 300 m vertical integration and 15 minute integration time. For wave energy comparison the values reported by *Wislon et al*. [1991] are scaled by a factor of 1.7 based on the above mean and median values to account for the exponential smoothing in our lidar retrievals.

References

Koopmans, L. H. (1974), *Probability and mathematical statistics, the spectral analysis of time series*, New York, NY.

Wang, W. (2003), *Spectral estimation of signal and noise power in Rayleigh lidar measurements of the middle atmosphere*, MS Thesis, University of Alaska Fairbanks.

Wilson, R., M. L. Chanin, and A. Hauchecorne (1991), Gravity waves in the middle atmosphere observed by Rayleigh lidar 2. Climatology, *J. Geophy. Res., 96*(D3), 5169-5183.

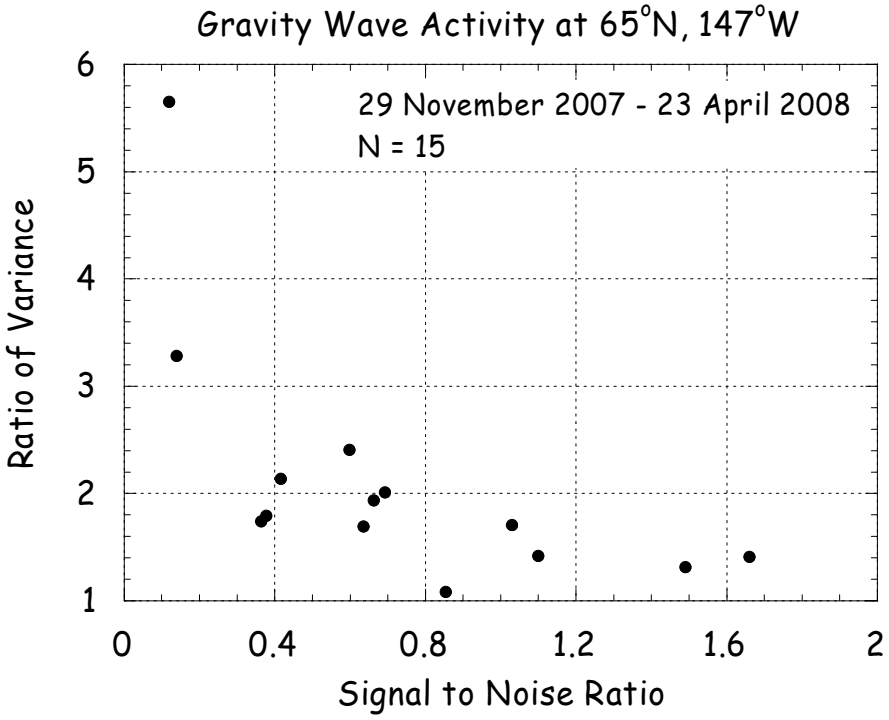

Figure C.1. Scatter plot of signal to noise ratio (SNR) and ratio of gravity wave variance

Appendix D. Effect of Aerosols on Rayleigh Lidar Temperature Retrieval

Rayleigh lidar density and temperatures are calculated from the backscattered photon counts based on the assumption that the upper stratosphere and lower mesosphere are free of aerosols (i.e. Rayleigh scattering only). In this appendix the effect of aerosols on the retrieved lidar temperature profile (the backscattered signal is a combination of Rayleigh and Mie scattering) is investigated using Rayleigh lidar data from the night of 21-22 January 1999, 10-11 February 1999, and 24-25 February 2000. Analysis of the photon count data indicates the appearance of an aerosol (rocket exhaust) layer on all three nights, a few minutes after a rocket was launched. The Rayleigh lidar start and end times and rocket launch time are tabulated in Table D.1. This Appendix follows the experimental method used to characterize Noctilucent Clouds over Chatanika, Alaska from *Collins et al*. [2009].

The photon count data is integrated over 4000 pulses (200 s) and smoothed with a running average of 0.225 km. The aerosol layer is characterized in terms of the backscatter ratio, volume backscatter coefficient, and integrated backscatter coefficient. The backscatter coefficient is calculated by using MSISE-90 [*Hedin*, 1991] densities. This density profile is normalized to the lidar signal below the aerosol layer to determine the backscatter coefficient. The aerosol backscatter ratio is calculated by interpolating the signal through the aerosol layer from below the layer to above the layer. The total backscatter ratio is the ratio of the total lidar signal (Rayleigh plus Mie scatter) to the estimated Rayleigh scatter signal by interpolation. The volume backscatter coefficient is the product of the aerosol backscatter ratio and the Rayleigh backscatter coefficient. The integrated backscatter coefficient is the integration of the backscatter coefficient over the altitude range of the aerosol layer.

The false color plot of the volume backscatter coefficient, and backscatter ratio, and the integrated backscatter coefficient, variation of altitude and backscatter coefficient of the peak aerosol layer on the night of 21-22 January 1999 is plotted in Figure D.1 and

D.2, on the night of 10-11 February 1999 in Figure D.3 and D.4, and on the night of 24-25 February 2000 in Figure D.5 and D.6.

The characteristics of the observed aerosol layers are tabulated in Table D.2, and summarized in this paragraph. On the night of 21-22 January 1999 the exhaust from the 0457 LST rocket launch is seen as an aerosol layer from ~0515 to 0545 LST between ~78-81 km in both the false color plots of backscatter coefficient and backscatter ratio. The integrated backscatter coefficient (Figure D.2 top) varies from 2 x 10^{-8} sr^{-1} to a maximum of 3 x 10^{-6} sr^{-1} at 0518 LST. The maximum peak backscatter coefficient is measured at 80.9 km at 0548 LST with a peak backscatter coefficient of 4.2 x 10^{-9} m^{-1} sr^{-1} at 0518 LST. On the night of 10-11 February 1999 the exhaust from the 2145 LST rocket launch is seen as an aerosol layer from ~2315 to 0045 LST between ~66-69 km in both the false color plots of backscatter coefficient and backscatter ratio. The integrated backscatter coefficient (Figure D.4 top) is a maximum of 2 x 10^{-7} sr^{-1} at 2315 LST. The maximum peak backscatter coefficient is measured at 69.0 km at 0018 LST with a peak backscatter coefficient of 1.5 x 10^{-10} m^{-1} sr^{-1} at 2315 LST. On the night of 24-25 February 2000 the exhaust from the 2245 LST rocket launch is seen as an aerosol layer from ~2315 to 0015 LST in both the false color plots of backscatter coefficient and backscatter ratio. The integrated backscatter coefficient (Figure D.6 top) varies is a maximum of 6 x 10^{-7} sr^{-1} at 2339 LST. The maximum peak backscatter coefficient is measured at 70.1 km at 0012 LST with a peak backscatter coefficient of 3.6 x 10^{-10} m^{-1} sr^{-1} at 2339 LST.

In Figure D.7 the temperature profile by integrating all the photon count profiles for the night and the temperature profile corrected for the presence of aerosols are plotted. On the night of 21-22 January 1999 the average temperature profile indicates a cold layer (from ideal gas law, if pressure is constant then as density increases temperature should decrease) with peak minimum temperature of 143.2 K at 78.6 km. On this night since the aerosol layer is near the seed temperature a large backlash owing to the downward integration technique is observed as a warmer temperatures with a maximum of 391.2 K at 76.0 km. On the nights of 10-11 February 1999 and 24-25 February 2000 a similar cold layer due to aerosols is measured with peak minimum temperature at 68.2 km (212.4 K)

and 69.2 km (200.4 K) respectively. The difference in temperature between the nightly mean temperature profile including the aerosol data and that not including the aerosol data is larger than errors on all three nights. Clearly the presence of an aerosol layer can cause problems with accurate temperature estimation of the stratosphere and mesosphere. The raw photon count data from the Rayleigh lidar at PFRR, Chatanika, Alaska are always analyzed for the possible presence of aerosols before integrating it for neutral temperature calculations.

References

Collins, R. L., M. J. Taylor, K. Nielsen, K. Mizutani, Y. Murayama, K. Sakanoi, M. T. DeLand (2009), Noctilucent cloud in the western Arctic in 2005: Simultaneous lidar and camera observations and analysis, *J. Atmos. Sol. Terr. Phys.*, *71*, 446-452, doi:10.1016/j.jastp.2008.09.044.

Hedin, A. E. (1991), Extension of the MSIS Thermospheric model into the middle and lower atmosphere, *J. Geophys. Res.*, *96*, 1159-1172.

Table D.1. Rayleigh lidar observation times and rocket launch times at Chatanika, Alaska (65^{o}N, 147^{o}W)

Date	Time	Total Time (hr)	Rocket Launch Time
21-22/01/1999	2135-0835	11.0	0457
10-11/02/1999	2005-0737	11.5	2145
24-25/02/2000	2124-0655	9.5	2245

Table D.2. Characteristics of aerosol layer from rocket exhaust observed at Chatanika, Alaska (65^{o}N, 147^{o}W)

Date	Time (LST)	Maximum Integrated Backscatter Coefficient (sr^{-1})	Maximum Peak Altitude (km)	Maximum Peak Backscatter Coefficient (m^{-1} sr^{-1})
22/01/1999	0515-0545	3×10^{-6}	80.9	4.1×10^{-9}
10/02/1999	2315-0045	2×10^{-7}	69.0	1.5×10^{-10}
24/02/2000	2315-0015	6×10^{-7}	70.1	3.6×10^{-10}

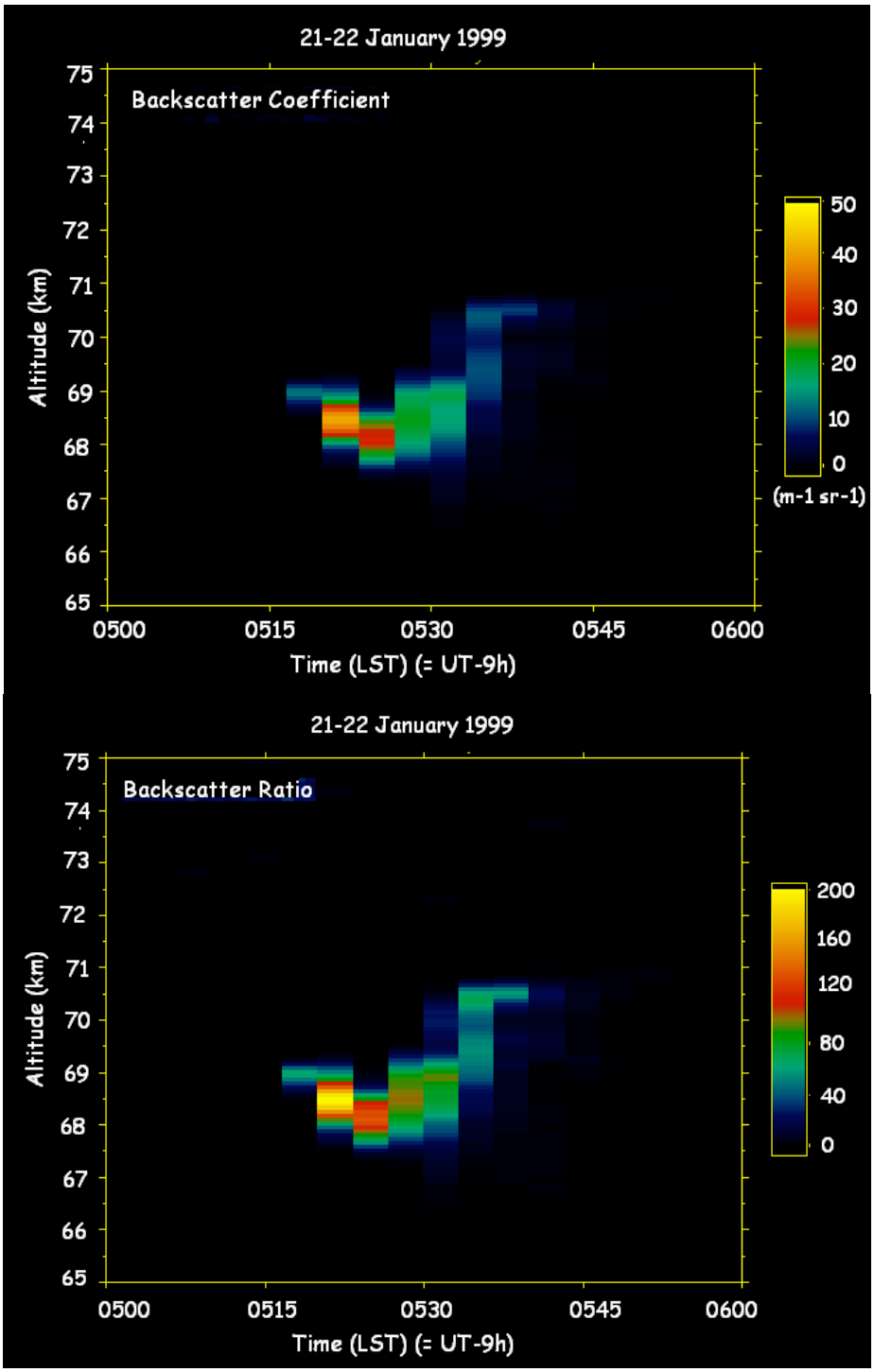

Figure D.1. False color plot of (top) volume backscatter coefficient and (bottom) backscatter ratio of aerosol layer as a function of time and altitude on the night of 21-22 January 1999. The backscatter coefficient is plotted in units of 10^{-10} m^{-1} sr^{-1}.

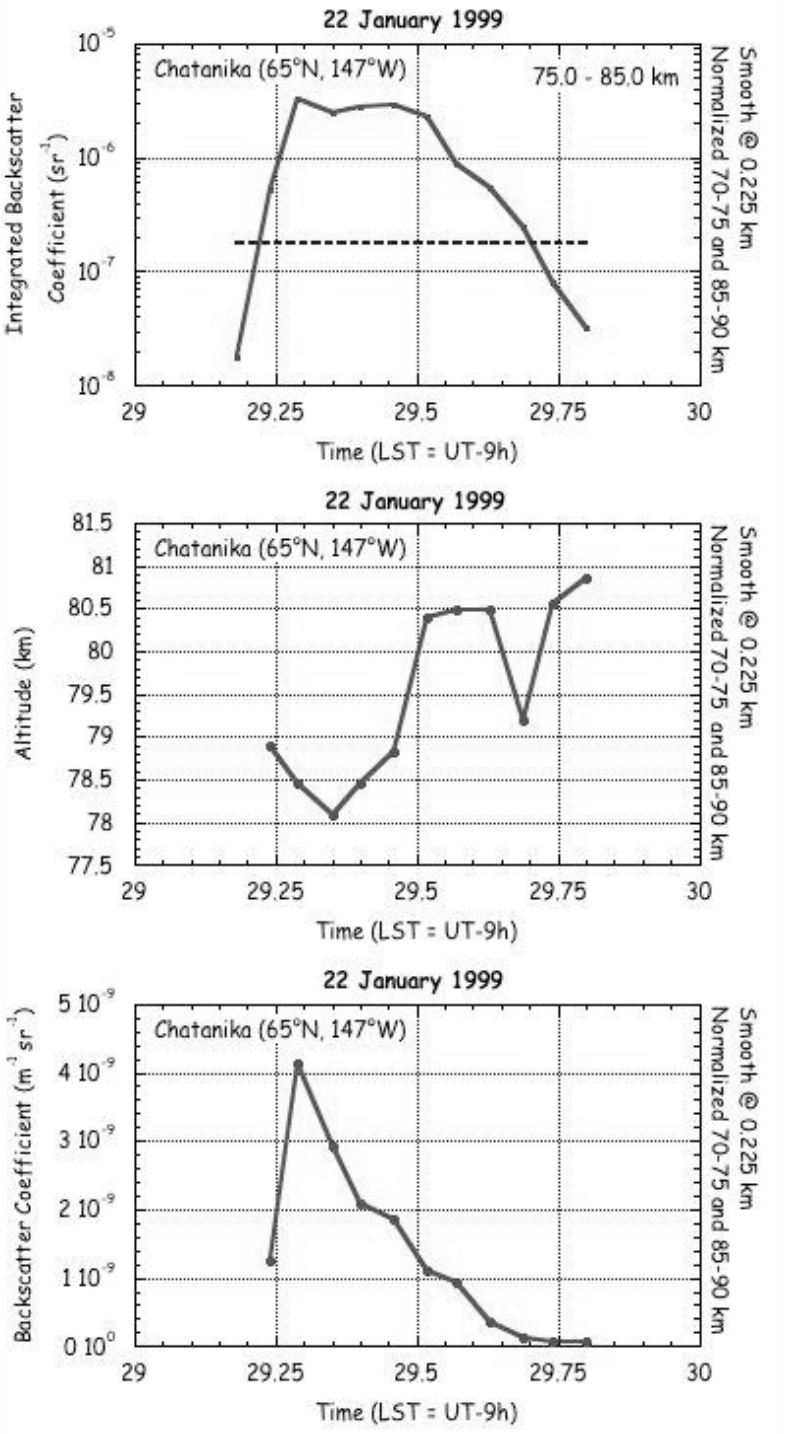

Figure D.2. (top) Integrated backscatter coefficient, variation of (mid) altitude and (bottom) backscatter coefficient of aerosol layer as a function of time on the night of 21-22 January 1999. The corresponding integrated Rayleigh backscatter coefficient is plotted as a dashed line for comparison.

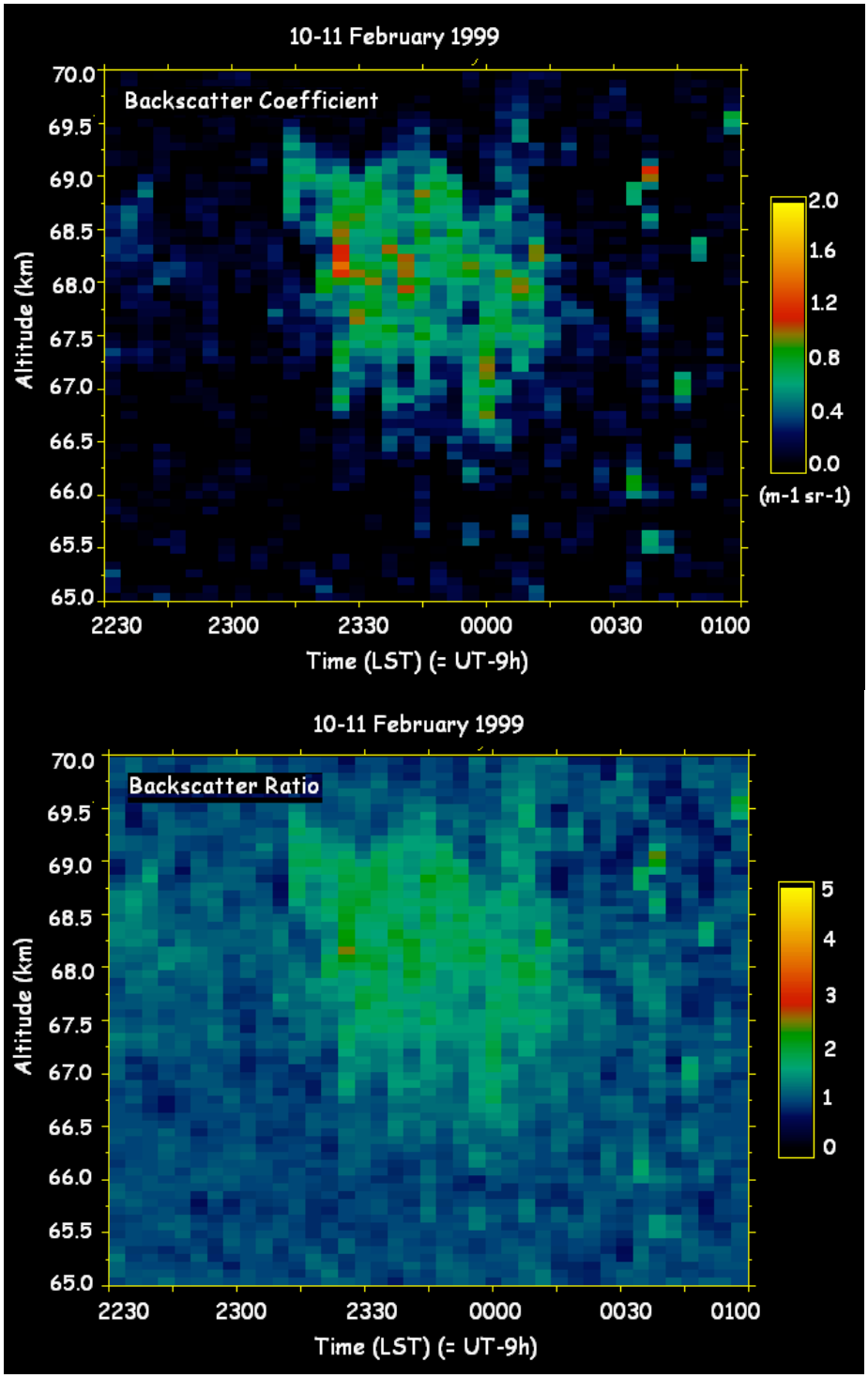

Figure D.3. False color plot of (top) volume backscatter coefficient and (bottom) backscatter ratio of aerosol layer as a function of time and altitude on the night of 10-11 February 1999. The backscatter coefficient is plotted in units of 10^{-10} m^{-1} sr^{-1}.

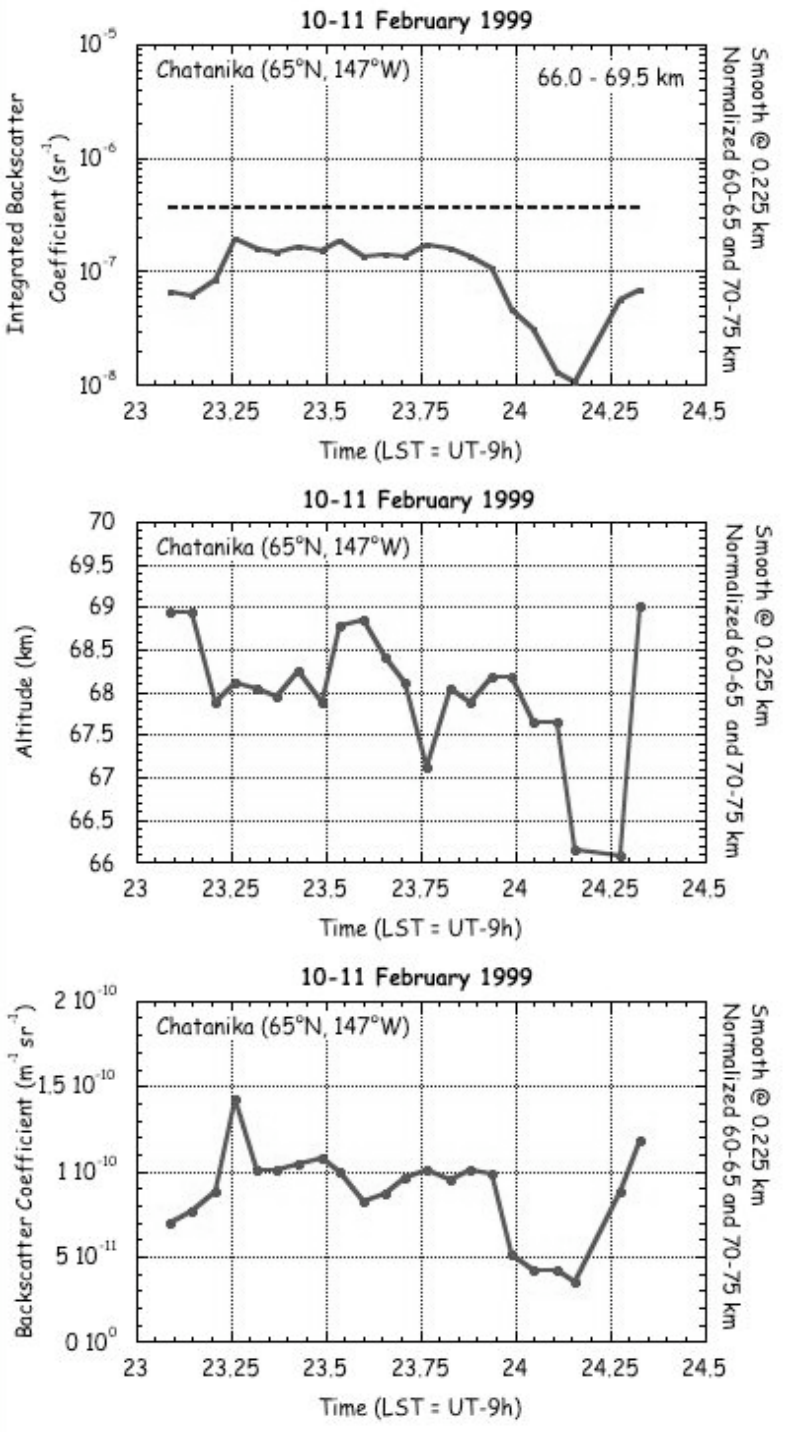

Figure D.4. (top) Integrated backscatter coefficient, variation of (mid) altitude and (bottom) backscatter coefficient of aerosol layer as a function of time on the night of 10-11 February 1999. The corresponding integrated Rayleigh backscatter coefficient is plotted as a dashed line for comparison.

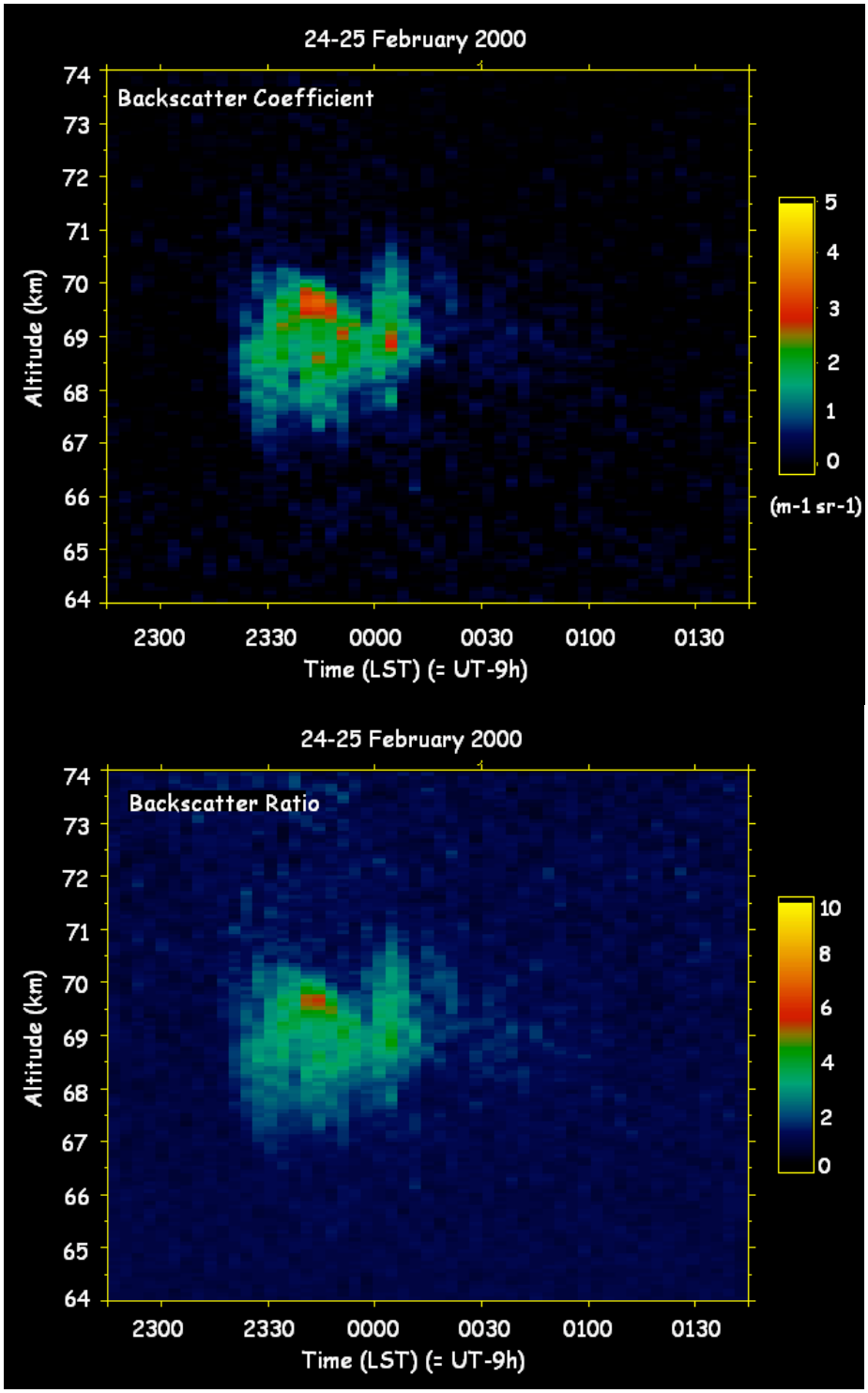

Figure D.5. False color plot of (top) volume backscatter coefficient and (bottom) backscatter ratio of aerosol layer as a function of time and altitude on the night of 24-25 February 2000. The backscatter coefficient is plotted in units of 10^{-10} m^{-1} sr^{-1}.

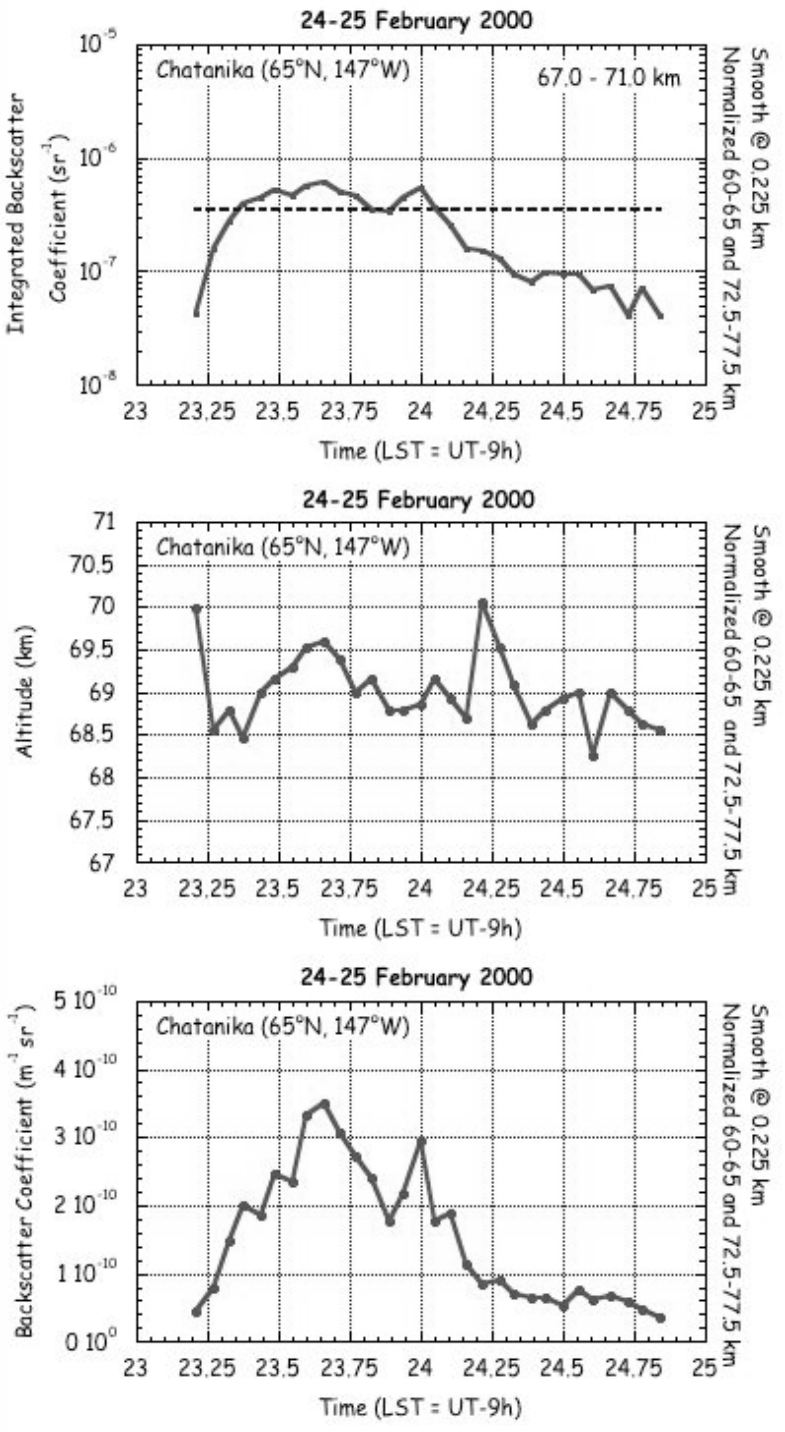

Figure D.6. Same Integrated backscatter coefficient, variation of (mid) altitude and (bottom) backscatter coefficient of aerosol layer as a function of time on the night of 24-25 February 2000. The corresponding integrated Rayleigh backscatter coefficient is plotted as a dashed line for comparison.

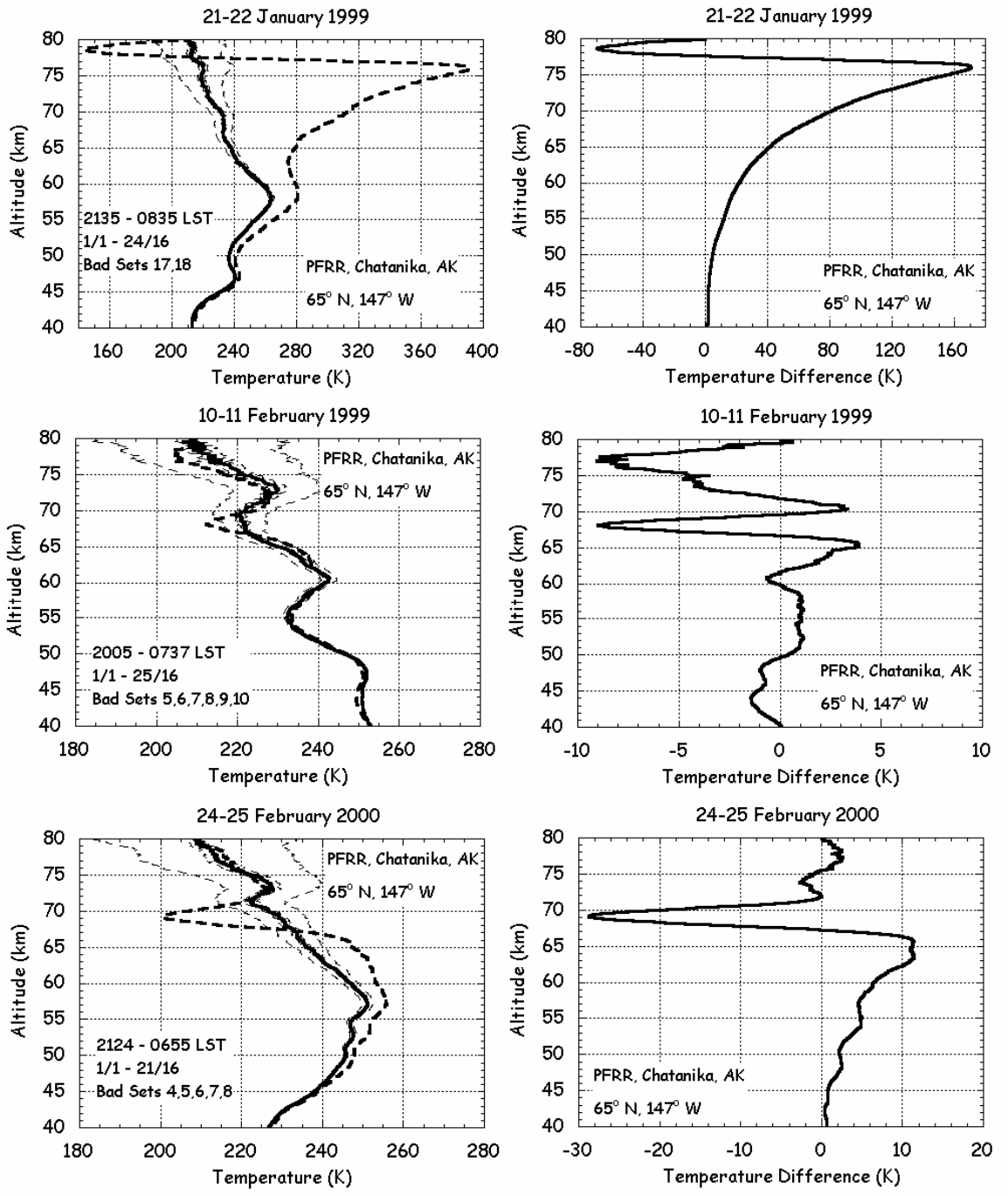

Figure D.7. (Left panel) Rayleigh lidar nightly mean temperature profiles on (top) 21-22 January 1999, (middle) 10-11 February 1999 and (bottom) 24-25 February 2000 with aerosol contamination (dashed line), and corrected for aerosols (solid line). The dashed lines are the temperature error and photon count error. (Right panel) The difference in temperature between Rayleigh lidar nightly mean temperature profile with and without aerosols.

Appendix E. Gradient Wind and Eliassen-Palm Flux Analysis using SABER\TIMED data

The Thermosphere Ionosphere Mesosphere Energetics and Dynamics (TIMED) mission is a sun-synchronous (polar orbiting) satellite launched on 7th December 2001 to obtain a global picture of the Mesosphere, Lower Thermosphere, and Ionospheric (MLTI) regions. The Sounding of the Atmosphere using Broadband Emission Radiometry (SABER) is one of the four instruments on board the spacecraft [*Russell et al*., 1999]. The other three instruments are TIMED Doppler Interferometer (TIDI), Solar Extreme Ultraviolet Experiment (SEE) and Global Ultraviolet Imager (GUVI). SABER uses a multi-channel radiometer to measure the limb infrared emission from the atmosphere [*Mertens et al*., 2004] in 10 broadband spectral channels ranging from 1.27 um to 17 um. SABER data provides information about the global vertical distribution of temperature, pressure, and trace gases such as CO_2, O_3, OH, and NO.

The SABER instrument does not provide direct measurements of wind. In this Appendix the calculation of gradient wind and Eliassen-Palm flux (EP flux) is documented using the temperature and geopotential data. Throughout this dissertation Level 2A version 1.07 data [*Beaumont*, 2008] has been used. The TIMED satellite has a yaw cycle (due to its solar angle requirement) alternating between the northern viewing phase, (~80^{o}N – 50^{o}S) and the southern viewing phase (~80^{o}N – 50^{o}S) approximately every 60 days. Examples of zonal mean gradient wind and divergence of EP flux are plotted for 16th January 2003, when the SABER measured started its 2003 yaw cycle in the northern hemisphere. This day also coincides with the peak of the January 2003 stratospheric warming event. The winds and EP flux are calculated using the SABER measured temperature, pressure, and geopotential. The SABER data is grid into 5^o latitude and 30^o longitude bins.

E.1. Gradient Wind Calculation

The zonal mean gradient wind is calculated by scaling (including only the leading order terms) the zonal averaged meridional momentum equation. To obtain winds only from geopotential height data various levels of approximations are made [*Randel*, 1987] to the equations of motion, and the horizontal winds are derived to be in geostrophic balance. A Geostrophic balance holds when the Coriolis term (f_o) is balanced by the horizontal gradient ($d\phi^{-1}$) of geopotential (Φ) and is applied to large scale extratropical systems. The zonal mean meridional momentum equation for hydrostatic and nearly geostrophic motions can thus be approximated to give the geostrophic zonal wind (u_g).

$$u_g = -f_o^{-1}\frac{d\overline{\Phi}}{d\phi} \tag{E.1}$$

From *Lieberman* [1999] the leading terms in the zonal mean meridional equation assuming steady state conditions, and neglecting eddy fluxes and advection by the mean meridional circulation, are,

$$\overline{u}(f_o + \overline{u}\tan\phi/a) = -\partial\overline{\Phi}/\partial\phi \tag{E.2}$$

The overbar denotes zonal mean, ϕ is the latitude, and *a,* the Earth's radius. From *Hitchman and Leovy* [1986] the zonal mean wind inside the parentheses can be approximated by the geostrophic value in E.1 to give the gradient wind u_r

$$\overline{u} = u_r = \frac{-\partial\Phi/\partial\phi}{f + u_g\tan\phi/a} = \frac{f_o u_g}{f_o + u_g\tan\phi/a}. \tag{E.3}$$

Figure E.1 shows a latitude-height plot the zonal mean gradient wind calculated using equation E.3 for 16th January 2003. The reversal of the winds (from westerly to easterly) associated with the major warming in mid-January 2003 is clearly seen poleward of 60^{o}N. The high westerly winds in the mesosphere are seen at the tropics.

E.2. Eliassen-Palm Flux Calculation

The Eliassen-Palm flux (EP flux, F) is a representation of the eddy-mean flow interaction in the atmosphere. It consists of two components, the eddy momentum flux (F_y) and eddy heat flux (F_z). These two components act in combination to drive changes

in the zonal-mean circulation and is given by the divergence of the EP flux ($\nabla \bullet F$) [*Holton*, 2004]. For a quasi-geostrophic approximation the divergence of the EP flux is given by [*Andrews et al*., 1987],

$$\nabla \bullet F \equiv -\left(\rho_o \overline{u'v'}\right)_\phi + \left(\rho_o f_o \overline{v'\theta'}/\theta_{oz}\right)_z \tag{E.4}$$

where the subscripts 'ϕ' and 'z' represent the meridional and vertical derivatives, and the subscript 'o' represents the vertical component i.e. the basic density $\rho_o = \rho_o(z)$ and the potential temperature $\theta_{oz} = d(\theta_o(z)/dz$. The Coriolis parameter $f_o = 2.\Omega.\sin\phi$ (Ω = 7.292 x 10^{-5} rad/s), u' and v' are the perturbation zonal and meridional winds, respectively. The overbar denotes the zonal average.

Following *Randel* [1987] the perturbation zonal and meridional winds can be calculated by rearranging the perturbation horizontal momentum equations. The leading terms in these rearranged equations are [*Andrews et al*., 1987 (equation 3.4.2a, 3.4.2b)],

$$\left[(a\cos\phi)^{-1}(\bar{u}\cos\phi)_\phi - f\right]v' + (a\cos\phi)^{-1}\Phi'_\lambda = 0 \tag{E.5}$$

$$\left(f + 2\bar{u}a^{-1}\tan\phi\right)u' + a^{-1}\Phi'_\phi = 0 \tag{E.6}$$

The subscripts denote derivatives, for example $X_y = dX/dy$. Reordering the above equations,

$$u' = \frac{-a^{-1}\Phi'_\phi}{\left(f + 2\bar{u}a^{-1}\tan\phi\right)} = \frac{-u'_g}{\left(f + 2\bar{u}a^{-1}\tan\phi\right)} \tag{E.7}$$

$$v' = \frac{-(a\cos\phi)^{-1}\Phi'_\lambda}{\left[(a\cos\phi)^{-1}(\bar{u}\cos\phi)_\phi - f\right]} \tag{E.8}$$

Figure E.2 shows the divergence of the EP flux on 16 January 2003 calculated using equation E.4. The contours have been scaled by the basic state density. The zonal force per unit mass exerted by the quasi-geostrophic eddies is stronger poleward of 60^{o}N due to the stronger planetary wave activity in this region.

References

Andrews, D. G., J. R. Holton, and C. B. Leovy (1987), *Middle atmosphere dynamics*, 489 pp., Academic Press Inc., New York.

Beaumont, K. (2008), SABER: Sounding of the atmosphere using broadband emission radiometry, http://saber.gats-inc.com/, data accessed June 2008.

Hitchman, M. H. and C. B. Leovy (1986), Evolution of the zonal mean state in the equatorial middle atmosphere during October 1978–May 1979, *J. Atmos. Sci.*, *43*, 3159–3176.

Holton, J. R. (2004), *An introduction to dynamic meteorology*, 535 pp. Elsevier Academic Press, Massachusetts.

Lieberman, R. S. (1999), The gradient wind in the mesosphere and lower thermosphere, *Earth Planets Space*, *51*, 751–761.

Mertens, C. J., F. J. Schmidlin, R. A. Goldberg, E. E. Remsberg, W. D. Pesnell, J. M. Russell III, M. G. Mlynczak, M. Lopez-Puertas, P. P. Wintersteiner, R. H. Picard, J. R. Winick, and L. L. Gordley (2004), SABER observations of mesospheric temperatures and comparisons with falling sphere measurements taken during the 2002 summer MaCWAVE campaign, *Geophys. Res. Lett.*, **31**(3), L03105, doi:10.1029/2003GL018605.

Randel, W. J. (1987), The evaluation of winds from geopotential height data in the stratosphere, *J. Atmos. Sci.*, *44*, 3097–3120.

Russell, J. M. III, M. G. Mlynczak, L. L. Gordley, J. Tansock, and R. Esplin (1999), An overview of the SABER experiment and preliminary calibration results, *Proceedings of the SPIE*, 44th Annual Meeting, Denver, Colorado, July 18-23, 3756, 277-288.

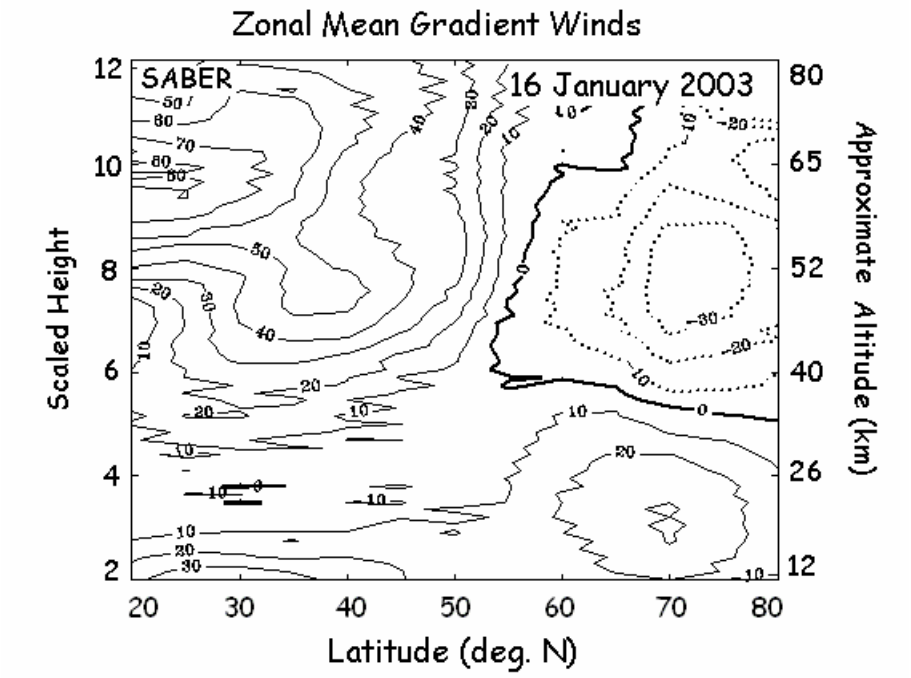

Figure E.1. Latitude height plot of zonal mean gradient wind on 16 January 2003 calculated from SABER data.

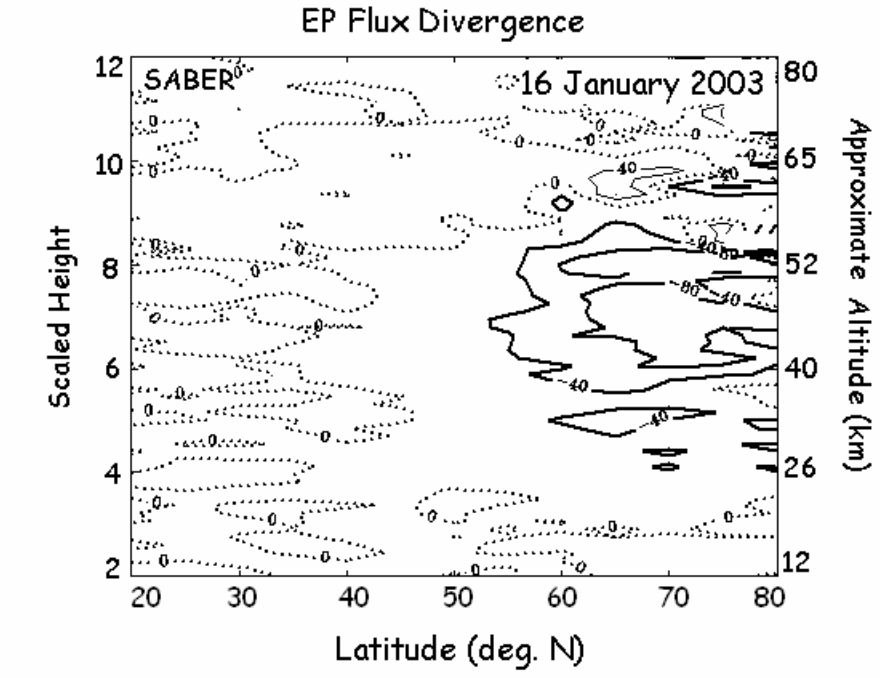

Figure E.2. Latitude height plot of divergence of Eliassen-Palm flux on 16 January 2003 calculated from SABER data.